

Ion acceleration by superintense laser-plasma interaction

Macchi, A., Borghesi, M., & Passoni, M. (2013). Ion acceleration by superintense laser-plasma interaction. *Reviews of Modern Physics*, 85(2), 751-793. <https://doi.org/10.1103/RevModPhys.85.751>

Published in:
Reviews of Modern Physics

Document Version:
Publisher's PDF, also known as Version of record

Queen's University Belfast - Research Portal:
[Link to publication record in Queen's University Belfast Research Portal](#)

Publisher rights
© 2013 American Physical Society (APS)

General rights
Copyright for the publications made accessible via the Queen's University Belfast Research Portal is retained by the author(s) and / or other copyright owners and it is a condition of accessing these publications that users recognise and abide by the legal requirements associated with these rights.

Take down policy
The Research Portal is Queen's institutional repository that provides access to Queen's research output. Every effort has been made to ensure that content in the Research Portal does not infringe any person's rights, or applicable UK laws. If you discover content in the Research Portal that you believe breaches copyright or violates any law, please contact openaccess@qub.ac.uk.

Ion acceleration by superintense laser-plasma interaction

Andrea Macchi^{*}

*Istituto Nazionale di Ottica, Consiglio Nazionale delle Ricerche (CNR/INO),
U.O.S. “Adriano Gozzini,” Pisa, Italy,
and Department of Physics “Enrico Fermi,” University of Pisa,
Largo Bruno Pontecorvo 3, I-56127 Pisa, Italy*

Marco Borghesi[†]

*Centre for Plasma Physics, The Queen’s University of Belfast,
BT7 1NN Belfast, United Kingdom
and Institute of Physics of the ASCR, ELI-Beamlines Project,
Na Slovance 2, 18221 Prague, Czech Republic*

Matteo Passoni[‡]

Dipartimento di Energia, Politecnico di Milano, Via Ponzio 34/3, I-20133 Milan, Italy

(published 10 May 2013)

Ion acceleration driven by superintense laser pulses is attracting an impressive and steadily increasing effort. Motivations can be found in the applicative potential and in the perspective to investigate novel regimes as available laser intensities will be increasing. Experiments have demonstrated, over a wide range of laser and target parameters, the generation of multi-MeV proton and ion beams with unique properties such as ultrashort duration, high brilliance, and low emittance. An overview is given of the state of the art of ion acceleration by laser pulses as well as an outlook on its future development and perspectives. The main features observed in the experiments, the observed scaling with laser and plasma parameters, and the main models used both to interpret experimental data and to suggest new research directions are described.

DOI: [10.1103/RevModPhys.85.751](https://doi.org/10.1103/RevModPhys.85.751)

PACS numbers: 52.38.Kd, 41.75.Jv, 52.27.Ny

CONTENTS

I. Introduction	751	E. Experimental optimization	770
II. Laser Ion Acceleration in a Nutshell	754	1. Energy cutoff enhancement	770
A. Laser interaction with overdense matter	754	2. Source spectrum manipulation	771
B. Hot electrons	755	3. Staged acceleration and beam control	772
1. Heating models	755	IV. Other Acceleration Mechanisms	773
2. Simulations, multidimensional effects, and simple estimates	757	A. Radiation pressure acceleration	773
3. Hot electron transport in solid matter	757	1. Thick targets: Hole boring regime	773
C. Ion acceleration mechanisms	758	2. Thin targets: Light sail regime	775
1. Rear surface acceleration	758	B. Collisionless shock acceleration	777
2. Front surface acceleration	758	C. Transparency regime: Breakout afterburner	778
3. Acceleration schemes using innovative targetry	759	D. Acceleration in near-critical and underdense plasmas	779
D. Particle-in-cell simulations	759	E. Resistively enhanced acceleration	780
E. Ion diagnostics	760	V. Current and Future Applications	780
III. Target Normal Sheath Acceleration	761	A. Proton radiography	780
A. TNSA scenario: Main experimental observations	761	B. Production of warm dense matter	782
B. Characterization of beam properties	762	C. Fast ignition of fusion targets	783
C. TNSA modeling	764	D. Biomedical applications	784
1. Quasistatic models	765	E. Nuclear and particle physics	785
2. Plasma expansion into vacuum	766	VI. Conclusions and Outlook	786
3. Multispecies expansion	767	Acknowledgments	787
4. Numerical simulations	768	References	787
D. Comparison between models and experiments	768		

I. INTRODUCTION

More than half a century ago, [Veksler \(1957\)](#) introduced the concept of “coherent acceleration” of particles as a mechanism in which the accelerating field on each particle is proportional to the number of particles being accelerated,

^{*}<http://www.df.unipi.it/~macchi>
andrea.macchi@ino.it

[†]m.borghesi@qub.ac.uk

[‡]matteo.passoni@polimi.it

in contrast to traditional techniques. Additional elements in Veksler's vision of future accelerators included the automatic synchrony between the particles and the accelerating field, the localization of the latter inside the region where the particles are, and the production of quasineutral groups with large numbers of energetic particles.

These features are realized in the acceleration of ions from plasmas produced by intense laser pulses. In this case, as a very general description, strong electric fields are generated by a collective displacement of a large number of electrons, and such electric fields accelerate ions until charge neutrality is restored and ions move together with electrons in a ballistic way.

Before the year 2000, ions having energies up to several MeVs had been observed in several high-intensity laser-matter interaction experiments and for different targets, including thick solid foils (Gitomer *et al.*, 1986; Fews *et al.*, 1994; Beg *et al.*, 1997, and references therein), gas jets (Krushelnick *et al.*, 1999; Sarkisov *et al.*, 1999, and references therein) and submicrometric clusters (Ditmire *et al.*, 1997, 1999, and references therein). Common to these experiments was the rather isotropic ion emission and the resulting low brilliance, making these configurations unattractive as ion accelerators for applications.

In 2000 three experiments (Clark *et al.*, 2000a; Maksimchuk *et al.*, 2000; Snavely *et al.*, 2000) independently reported the observation of an intense emission of multi-MeV protons from solid targets, either metallic or plastic (CH), of several microns thickness irradiated by high-intensity laser pulses. The basic setup of these experiments is shown in Fig. 1. The laser intensity, number of protons, and maximum ion energy observed for the three experiments were $3 \times 10^{18} \text{ W cm}^{-2}$, $\geq 10^9$ and 1.5 MeV (Maksimchuk *et al.*, 2000), $5 \times 10^{19} \text{ W cm}^{-2}$, $\sim 10^{12}$ and 18 MeV (Clark *et al.*, 2000a), and $3 \times 10^{20} \text{ W cm}^{-2}$, $\sim 2 \times 10^{13}$, and 58 MeV (Snavely *et al.*, 2000), respectively. Figure 2 shows the spectrum of protons observed by Snavely *et al.* (2000). The protons were detected at the rear side of the target, opposite to the laser-irradiated surface and were emitted, as a rather collimated beam, along the target normal direction.

The emission of protons from metallic targets whose chemical composition does not include hydrogen may sound surprising, but it was already clear from previous experiments that protons originated from impurities, i.e., thin layers of

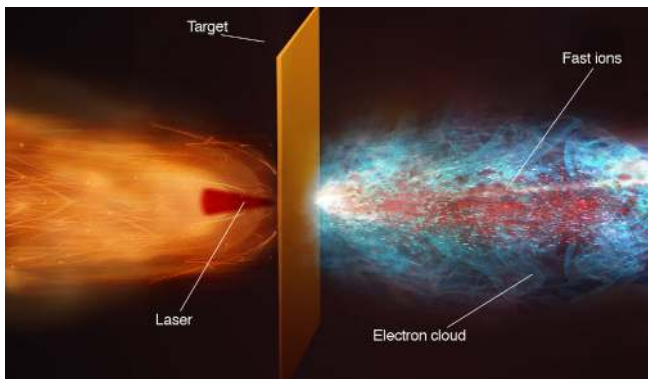


FIG. 1 (color online). Artist's view of a typical experiment on proton emission from laser-irradiated solid targets.

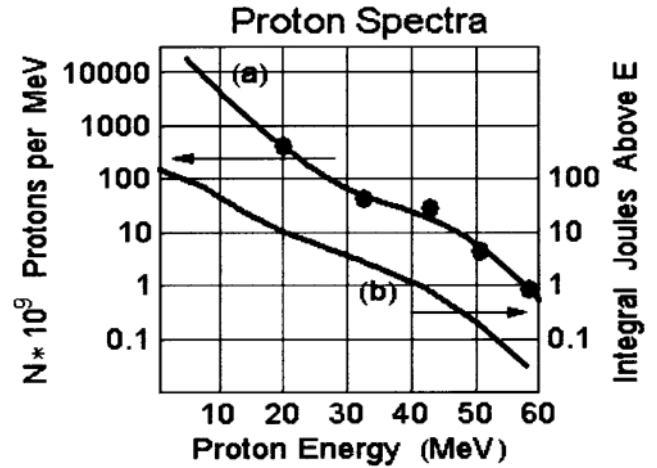


FIG. 2. Proton energy spectrum from the rear side of a $100 \mu\text{m}$ solid target irradiated by a 423 J, 0.5 ps pulse at normal incidence, corresponding to an intensity of $3 \times 10^{20} \text{ W cm}^{-2}$. The integrated energy of protons indicates a conversion efficiency of $\approx 10\%$ for protons above 10 MeV. From Snavely *et al.*, 2000.

water or hydrocarbons which are ordinarily present on solid surfaces under standard experimental conditions. In experiments performed with both “long” nanosecond pulses (Gitomer *et al.*, 1986, and references therein) and “short” (sub)picosecond, high-intensity pulses (Fews *et al.*, 1994; Beg *et al.*, 1997; Clark *et al.*, 2000b), protons and heavier ions were commonly detected in the backward direction (i.e., toward the laser) with a broad angular distribution, and their origin was interpreted in terms of acceleration during the expansion of the hot laser-produced plasma at the front (laser-irradiated) side of the target. The characteristics of the forward proton emission in the new experiments, such as the high degree of collimation and laminarity of the beam, were much more impressive.

These findings generated an enormous interest both in fundamental research and in the possible applications. In an applicative perspective, the most relevant and peculiar feature of multi-MeV ions is the profile of energy deposition in dense matter. Different from electrons and x rays, protons and light ions deliver most of their energy at the end of their path (see Fig. 3), at the so-called Bragg peak (Ziegler, Biersack, and Ziegler, 2008; Knoll, 2010). The physical reason is that the energy loss is dominated by Coulomb collisions for which the cross section strongly grows with decreasing energy, so that the stopping process becomes progressively more and more efficient. This property makes protons and ions very suitable for highly localized energy deposition. The applications that were proposed immediately after the discovery of multi-MeV proton acceleration included ion beam cancer therapy, laser triggering and control of nuclear reactions, production of warm dense matter, “fast ignition” of inertial confinement fusion targets, and injectors for ion accelerators. These foreseen applications are reviewed in Sec. V. As a particularly innovative and successful application, ultrafast probing of plasmas by laser-driven proton beams is described in Sec. V.A.

While the potential for applications was apparent, the details of the physics behind proton acceleration were not clear. A debate arose on the actual location of the region where the

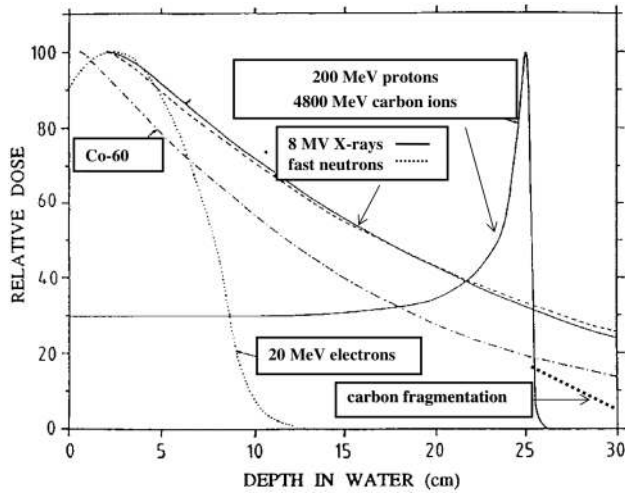


FIG. 3. Example of the profile of energy deposition of protons and C ions in water, compared to those of electrons, x and γ rays, and neutrons. Protons and C ion profiles are characterized by the Bragg peak at the end of the path. The quantity plotted is the relative dose, i.e., the energy absorbed per unit mass. From [Amaldi and Kraft, 2005](#).

protons were accelerated and, consistently, on the mechanism driving the acceleration. [Clark *et al.* \(2000a\)](#) and [Maksimchuk *et al.* \(2000\)](#) suggested that protons were accelerated at the front side of the target, crossing the latter and being detected on the opposite side. In contrast, [Snively *et al.* \(2000\)](#) provided evidence that protons were accelerated at the rear side [see also [Hatchett *et al.* \(2000\)](#)]. To support the interpretation of these latter experiments (performed at the petawatt facility of Lawrence Livermore National Laboratory, USA) the so-called target normal sheath acceleration (TNSA) model was introduced by [Wilks *et al.* \(2001\)](#). Briefly, TNSA is driven by the space-charge field generated at the rear surface of the target by highly energetic electrons accelerated at the front surface, crossing the target bulk, and attempting to escape in vacuum from the rear side. The basic theory of TNSA and related models is described in detail in Sec. III. Most of the experiments investigating proton acceleration by laser interaction with solid targets have been interpreted in terms of the TNSA framework (see Secs. III.A and III.B) that has also guided developments toward source optimization by target engineering (see Sec. III.E).

A major requirement for several of the foreseen applications is an increase of the energy per nucleon up to hundreds of MeV and beyond. The next generation of laser facilities should allow intensities higher than the current record of $\sim 10^{22} \text{ W cm}^{-2}$ ([Yanovsky *et al.*, 2008](#)), but at present it is not guaranteed that the ion energy scaling observed so far will be maintained at such extreme intensities nor that TNSA will still be effective. An analysis of proton acceleration experiments performed up to 2006 suggests a $\sim (I\lambda^2)^{1/2}$ scaling of proton energy up to values of $I\lambda^2 = 3 \times 10^{20} \text{ W cm}^{-2} \mu\text{m}^2$ ([Borghesi *et al.*, 2006](#); [Fuchs *et al.*, 2006b](#)), where I and λ are the laser intensity and wavelength, respectively. Figure 4 summarizes such data, together with more recent results obtained with Ti:Sa-based, ultrashort (tens of fs) pulses, exhibiting a $\sim I\lambda^2$ scaling. Measurements by [Robson *et al.*](#)

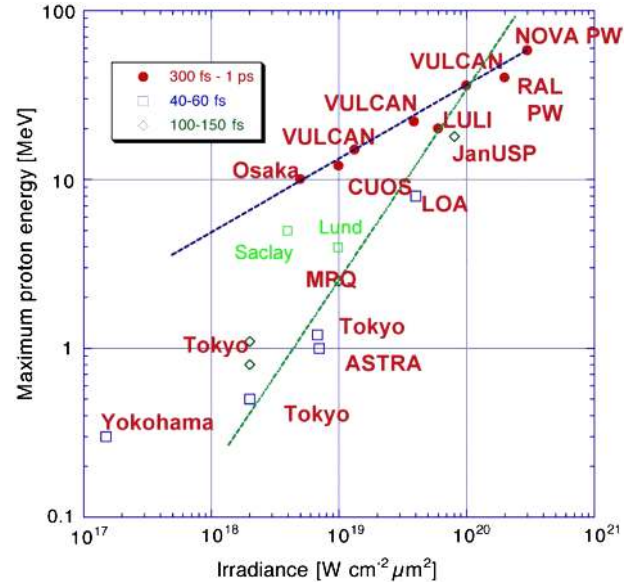


FIG. 4 (color online). Maximum proton energy from laser-irradiated solid targets as a function of the laser irradiance and for three ranges of pulse durations, reporting experiments up to 2008. Two trend lines are overlaid, the shallower one corresponding to a $\sim I^{1/2}$ dependence, and the steeper one to a scaling proportional to I . From [Borghesi *et al.*, 2008](#).

(2007) at energies up to 400 J, pulse durations between 1 and 8 ps, and intensities up to $6 \times 10^{20} \text{ W cm}^{-2}$ suggested a slower scaling. It is also of crucial importance to establish the most relevant scaling parameters as well as to improve or optimize beam emittance, brilliance, and monoenergeticity for specific applications. For instance, TNSA-generated proton beams are highly laminar and have very low emittance (see Sec. III.B) but the energy spectrum is ordinarily broad and thus not optimal for most applications.

These issues motivate the search for other ion acceleration mechanisms. These include concepts which have been explored previously in different contexts (e.g., astrophysics), such as radiation pressure acceleration (RPA) and collisionless shock acceleration (CSA). Other proposed schemes exploit the potential of both advanced target engineering and nonlinear “relativistic” optical effects in plasmas, such as ion acceleration in ultrathin solid targets which become transparent to intense laser pulses [break-out afterburner (BOA)], or involving low-density targets. The basic physics of these mechanisms and the related experimental work, still in a preliminary stage with respect to TNSA, will be described in Sec. IV. The development of advanced acceleration schemes is sustained by the continuous trend toward laser pulses of higher intensity and energy. A detailed account of the many active projects and facilities under development based on optical and infrared lasers ($\lambda \sim 1 \mu\text{m}$) is given in Sec. II of [Di Piazza *et al.* \(2012\)](#). Progress toward CO₂ lasers ($\lambda \sim 10 \mu\text{m}$) having multiterawatt power ([Haberberger, Tochitsky, and Joshi, 2010](#)) is also of growing interest for ion acceleration, as discussed in Secs. IV.A.1 and IV.B.

On the theoretical side, the interpretation of experiments has revitalized classic and often controversial problems of plasma physics such as plasma expansion into vacuum and

the formation of collisionless sheaths, at the basis of most of the TNSA models, as well as other general physics models such as the motion of relativistic moving mirrors, a concept already discussed in the original work on special relativity by [Einstein \(1905\)](#), which serves as a model for RPA. Simple, analytically affordable models are extremely useful to understand the basic acceleration mechanisms and, in particular, to provide scaling laws which may give directions for further developments. Reference models also highlight the several connections with other fields, such as the physics of discharges, of ultracold plasmas, and of particle acceleration in astrophysics. The theoretical discussions in Secs. III and IV are, to a significant extent, based on this approach.

Beyond simple modeling a rich and complex dynamics of laser-plasma interaction and ion acceleration, involving collective and self-organization effects, is apparent. Unfolding such dynamics requires the use of self-consistent electromagnetic (EM), kinetic simulations. To this aim, the particle-in-cell (PIC) method (see Sec. II.D) is by far the most commonly used approach. Large-scale, multidimensional PIC simulations running on parallel supercomputers are an effective support for the design and interpretation of laser-plasma acceleration experiments, although fully “realistic” simulations in three spatial dimensions and for actual laser and target parameters are most of the time still beyond computational capabilities. These limitations further motivate the development of complementary, reduced simulation models. These issues are further discussed in Secs. II.D and III.C.4.

A comprehensive description of laser-plasma dynamics is far beyond the scope of this work and can be found in recent books and reviews ([Gibbon, 2005b](#); [Mourou, Tajima, and Bulanov, 2006](#); [Mulser and Bauer, 2010](#)). In Secs. II.A and II.B we describe only a few basic issues of relevance to the understanding of ion acceleration mechanisms. The main mechanisms are first introduced in a compact form in Sec. II.C, leaving a detailed discussion to the following Secs. III and IV.

II. LASER ION ACCELERATION IN A NUTSHELL

A. Laser interaction with overdense matter

In this work we mostly refer to ion acceleration occurring in the interaction with solid targets, where the electron density n_e greatly exceeds the so-called critical or cutoff density,

$$n_c = \frac{m_e \omega^2}{4\pi e^2} = 1.1 \times 10^{21} \text{ cm}^{-3} \left(\frac{\lambda}{1 \text{ } \mu\text{m}} \right)^{-2}. \quad (1)$$

The condition $n_e = n_c$ is equivalent to $\omega_p = \omega$, where $\omega_p = (4\pi n_e e^2 / m_e)^{1/2}$ and $\omega = 2\pi c / \lambda$ are the plasma and laser frequencies, respectively. Since the linear refractive index of the plasma is $n = (1 - \omega_p^2 / \omega^2)^{1/2} = (1 - n_e / n_c)^{1/2}$, in the $n_e > n_c$ “overdense” region n has imaginary values and the laser pulse cannot propagate. All the laser-plasma interaction occurs either in the “underdense” region where $n_e < n_c$ or near the “critical” surface at which $n_e \simeq n_c$.

Relativistic effects make the refractive index nonlinear. Qualitatively speaking, the relativistic refractive index

describing the propagation of a plane wave with vector potential $\mathbf{A} = \mathbf{A}(x, t)$ is obtained from the linear expression by replacing the electron mass with the quantity $m_e \gamma$, where the relativistic factor γ is given by

$$\gamma = \sqrt{1 + \langle \mathbf{a}^2 \rangle} = \sqrt{1 + a_0^2 / 2}, \quad (2)$$

where $\mathbf{a} = e\mathbf{A} / m_e c^2$, and the angular brackets denote an average over the oscillation period. The parameter a_0 is the commonly used “dimensionless” amplitude related to the laser intensity I by¹

$$a_0 = 0.85 \left(\frac{I \lambda_{\mu\text{m}}^2}{10^{18} \text{ W cm}^{-2}} \right)^{1/2}, \quad (3)$$

where we used $I = c \langle E^2 \rangle / 4\pi$ to relate the electric field $\mathbf{E} = -(1/c) \partial \mathbf{A} / \partial t$ to the laser intensity I .

The nonlinear, relativistic index $n_{\text{NL}} = (1 - n_e / \gamma n_c)^{1/2}$ becomes imaginary when $n_e > \gamma n_c$, showing an increase of the cutoff density for a plane monochromatic wave: this effect is known as relativistic self-induced transparency or, briefly, relativistic transparency. However, the problem of laser penetration inside a plasma is not trivial ([Cattani et al., 2000](#); [Goloviznin and Schep, 2000](#); [Shen and Xu, 2001](#)) because of both the nonlinearity in the wave equation and the self-consistent modification of the plasma density profile due to radiation pressure effects. These latter may be described via the ponderomotive force (PF).² In an oscillating, quasimonochromatic electromagnetic field described by a dimensionless vector potential $\mathbf{a}(\mathbf{r}, t)$ whose envelope is sufficiently smooth in space and time, the relativistic PF is [see, e.g., [Bauer, Mulser, and Steeb \(1995\)](#) and [Mulser and Bauer \(2010\)](#)]

$$\mathbf{f}_p = -m_e c^2 \nabla (1 + \langle \mathbf{a}^2 \rangle)^{1/2}. \quad (4)$$

For a plane wave impinging on an overdense plasma, the resulting PF, more effective on the lightest particles, is in the inward direction and tends to push and pile up electrons inside the plasma. Ponderomotive effects will be further discussed below (see Secs. II.B and II.C).

In a multidimensional geometry, a laser pulse of finite width may produce a density depression around the propagation axis also because of the ponderomotive force pushing the electrons in the radial direction. Jointly with the relativistic effect and target expansion driven by electron heating, this mechanism may lead to a transition to transparency as soon as the electron density drops below the cutoff value ([Fuchs et al., 1999](#)). Investigations of ion acceleration in the transparency regime are described in Sec. IV.C.

¹Consistently with our definitions, given the value for I , the peak value of the dimensionless vector potential of the plane wave will be given by a_0 for linear polarization and by $a_0 / \sqrt{2}$ for circular polarization.

²Throughout this review we refer to the ponderomotive force as the slowly varying, effective force describing the cycle-averaged motion of the “oscillation center” of a charged particle in an oscillating nonuniform field, over a time scale longer than the oscillation period. “Fast” oscillating components are not included in the definition of ponderomotive force here adopted.

The penetration of the laser pulse depends not only on the electron density but also on the target size when the latter becomes close to or smaller than one wavelength. As a simple but useful example, the nonlinear transmission and reflection coefficients can be calculated analytically for a sub-wavelength foil modeled as a Dirac deltalike density profile (Vshivkov *et al.*, 1998; Macchi, Veghini, and Pegoraro, 2009), obtaining a transparency threshold

$$a_0 > \pi \frac{n_e}{n_c} \frac{\ell}{\lambda} \equiv \zeta, \quad (5)$$

where ℓ is the thickness of the foil. Equation (5) has some interest for the interaction with ultrathin foil targets (see Secs. IV.A.2–IV.C).

B. Hot electrons

Since the laser pulse cannot penetrate into solid-density regions, the absorbed energy is transported to these regions mostly by energetic (commonly named either hot or fast) electrons which may be generated during the interaction through several mechanisms. By hot electrons in the present context one typically refers to relativistic electrons whose energy is of the order of the cycle-averaged oscillation energy in the electric field of the laser in vacuum,

$$\mathcal{E}_p = m_e c^2 (\gamma - 1) = m_e c^2 (\sqrt{1 + a_0^2/2} - 1), \quad (6)$$

where Eq. (2) has been used. Equation (6) is also called the “ponderomotive” energy (Wilks *et al.*, 1992). Hot electrons penetrating into solid targets have been observed and characterized in several experiments at very high intensities and for different interaction conditions³ and play a fundamental role in applications such as laser-driven photonuclear physics and fast ignition of fusion targets. Moreover, as discussed in Sec. III, in most of the experiments reported so far, acceleration of protons and heavier ions is driven by hot electrons.

The process of hot electron generation turns out to be complex and, possibly, not yet completely understood. A review of past and ongoing research on the topic can be found in recent books (Gibbon, 2005b; Mulser and Bauer, 2010). Here we give a basic discussion at a qualitative level, focusing on those aspects which are most essential and relevant to ion acceleration.

At the surface of an overdense plasma, electrons are driven by the Lorentz force $\mathbf{f}_L = -e(\mathbf{E} + \mathbf{v} \times \mathbf{B}/c)$ which includes both the fields of the incident and reflected laser pulses and self-generated fields. As a necessary condition for the efficient generation of hot electrons near the critical surface \mathbf{f}_L must have an *oscillating* component directed along the density gradient ∇n_e . This is the case for the well-known resonance absorption where the condition $\mathbf{E} \cdot \nabla n_e \neq 0$ is necessary to drive resonant plasma oscillations which in turn accelerate electrons. In a plane geometry such condition requires oblique incidence and *P* polarization of the laser pulse. This absorption mechanism is sensitive to the density

scale length $L_n = n_e/|\nabla n_e|$ because the driving force is evanescent in the resonance region.

In a sharp-boundary plasma where $L_n \ll \lambda$, absorption and heating may arise because electron motion is not adiabatic, as electrons are driven from the region of strong fields to the evanescence region in a time shorter than $2\pi/\omega$, so that the cycle average $-e\langle \mathbf{E} \cdot \mathbf{v} \rangle$ may not cancel out. Thus, short duration and high-intensity laser pulses favor electron heating because the hydrodynamic expansion does not have sufficient time to wash out sharp density gradients nor is it dominated by the strong ponderomotive force that steepens the density profile.

At this point it is worth mentioning that in most high-intensity experiments the main interaction pulse is preceded by prepulses⁴ which cause early plasma formation and expansion, so that the short-pulse interaction does not occur with a sharp-boundary, solid-density plasma. However, profile steepening at the critical surface is still effective; thus one may expect the interactions to still occur with a sharp density profile, having a lower density jump with respect to a solid interface. Occasionally, “preplasma” formation may also allow additional electron acceleration mechanisms to take place in the underdense plasma region (Esarey, Schroeder, and Leemans, 2009), possibly leading to electron energies much higher than given by Eq. (6). In more recent experiments, advanced pulse cleaning techniques allow minimizing prepulse effects (see Sec. III.E).

1. Heating models

A popular electrostatic model of electron heating at a step-boundary plasma was proposed by Brunel (1987). In this model, electrons are dragged out of the surface of a perfect conductor by an oscillating “capacitor field,” extending on the vacuum side, and representing the *P* component of the incident plus reflected laser electric field. Electrons are considered to be “absorbed” when, after having performed about half of an oscillation on the vacuum side, they reenter the target, there delivering their energy, which is of the order of the oscillation energy in the external field.⁵ The model thus accounts in a simplified way for the pulsed generation (once per cycle) of hot electrons directed into the target and having an energy, roughly speaking, close to the “vacuum” value (6). This simple model is not self-consistent because, for instance, the capacitor field is assumed to vanish inside the target, implying the presence of a surface charge density. Nevertheless, following Mulser, Ruhl, and Steinmetz (2001) it is possible to provide a “minimal” 1D model, still in the capacitor approximation, where the electrostatic field is calculated self-consistently and an acceleration of electron bunches similar to that inferred by Brunel is apparent. We consider the electric field as the sum of the electrostatic and driver fields, e.g., $E_x = E_e + E_d$, where $E_d = \tilde{E}_d(t) \sin \omega_0 t$ with $\tilde{E}_d(t)$ a suitable temporal envelope, a step-boundary density profile $n_i = n_0 \Theta(x)$ ($Z = 1$ for

³See, e.g., Key *et al.* (1998), Wharton *et al.* (1998), H. Chen *et al.* (2009), Tanimoto *et al.* (2009), and Nilson *et al.* (2010), and references therein.

⁴In general the main pulse is preceded both by short pulses of duration similar to the main pulse and by a much longer pedestal due to amplified spontaneous emission.

⁵This effect is also commonly referred to as “vacuum heating.” See Gibbon (2005b) for a discussion on the origin of the name.

simplicity), and a “cold” plasma, i.e., we neglect thermal pressure. Following these assumptions we write Maxwell’s equations for the electrostatic field and Euler’s equation for the electron fluid having velocity v_x :

$$\partial_x E_e = 4\pi\rho = 4\pi e[n_0\Theta(x) - n_e], \quad (7)$$

$$\partial_t E_e = -4\pi J_x = 4\pi e n_e v_x, \quad (8)$$

$$\frac{dv_x}{dt} = (\partial_t + v_x \partial_x) v_x = -\frac{e}{m_e} (E_e + E_d). \quad (9)$$

Switching to Lagrangian variables x_0 and $\xi = \xi(x_0, t)$ defined by $x = x_0 + \xi$, $d\xi/dt = v_x$, a straightforward calculation along with the constraint of E_e being continuous at $x = x_0 + \xi = 0$ yields the following equations of motion describing electrostatic, forced oscillations of electrons across a steplike interface:

$$\frac{d^2 \xi}{dt^2} = \begin{cases} -\omega_p^2 \xi - eE_d/m_e & (x_0 + \xi > 0), \\ +\omega_p^2 x_0 - eE_d/m_e & (x_0 + \xi < 0). \end{cases} \quad (10)$$

From Eq. (10) we see that electrons crossing the boundary ($x = x_0 + \xi < 0$) feel a secular force $\omega_p^2 x_0$ leading to dephasing from E_d and acceleration (Mulser, Ruhl, and Steinmetz, 2001). Equation (10) can be solved numerically for a discrete but large ensemble of electron “sheets” (corresponding to a set of values of $x_0 > 0$), with the prescription to exchange the values of x_0 for two crossing sheets to avoid the onset of singularity in the equations.⁶ Representative trajectories of electrons moving across the interface are found as in Fig. 5. Electrons whose trajectory extends in vacuum for half or one period of the driving field are observed. Similar trajectories are found in electromagnetic and self-consistent simulations (see Sec. II.B.2).

Note that the cold plasma assumption is consistent with the requirement that the external field should be strong enough to overcome the potential barrier which, in an equilibrium state, confines warm electrons inside a bounded plasma (such a barrier corresponds to a Debye sheath; see also Secs. II.C.1 and III.C.1). For $\omega_p \gg \omega$ and nearly total reflection, the laser field component normal to the surface has an amplitude $E_\perp \simeq 2E_0 \sin\theta$, with $E_0 = (4\pi I/c)^{1/2}$ the amplitude in vacuum. The sheath field is $E_s \simeq T_e/e\lambda_D = (4\pi n_0 T_e)^{1/2}$, so that the condition $E_\perp > E_s$ may be rearranged as $4(I/c)\sin^2\theta > n_0 T_e$. This implies (at nongrazing incidence) that the radiation pressure should exceed the thermal pressure and thus counteract the thermal expansion and steepen the density profile, making the assumption of a steplike plasma more self-consistent.

For S polarization or normal incidence there is no component of the electric field perpendicular to the surface. However, for high intensities the magnetic force term becomes important and may drive electron oscillations along the density gradient also for normal incidence. This effect is commonly named “ $\mathbf{J} \times \mathbf{B}$ ” heating (Kruer and Estabrook,

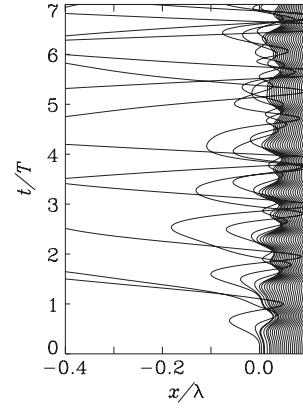


FIG. 5. Numerical solution of the electrostatic “plasma sheet” model based on Eq. (10) plus the exchange of initial position for crossing plasma sheets (see text for details). The trajectories of a limited number of sheets (1 over 20) in the (x, t) plane are shown. The driver field has the profile of an evanescent wave with peak amplitude $0.5m_e\omega c/e$ in vacuum and a $\sin^2(\pi t/2\tau)$ rising front with $\tau = 5T$ where $T = 2\pi/\omega$. A density $n_e/n_c = (\omega_p/\omega)^2 = 5$ is assumed.

1985). By considering the driver capacitor field as a model for the magnetic force component, the related electron dynamics may still be described using the above outlined models, but with two significant differences. First, to lowest order the magnetic force oscillates at 2ω , thus leading to the generation of hot electron bunches twice per laser period. Second, the oscillating component perpendicular to the surface vanishes for circular polarization (and normal incidence), so that hot electron generation might be strongly *suppressed* under such conditions. In fact, the vector potential representing a plane, elliptically polarized field may be written as

$$\mathbf{A}(x, t) = \frac{A(x)}{\sqrt{1+\epsilon^2}} (\hat{\mathbf{y}} \cos\omega t + \epsilon \hat{\mathbf{z}} \sin\omega t) \quad (11)$$

with $0 \leq \epsilon \leq 1$. Using $\mathbf{B} = \nabla \times \mathbf{A}$ and $\mathbf{p}_\perp = e\mathbf{A}/c$ for the transverse momentum of electrons, the $-e(\mathbf{v} \times \mathbf{B}/c)$ force can be written as

$$-e \frac{\mathbf{v}}{c} \times \mathbf{B} = -\hat{\mathbf{x}} \frac{e^2 \partial_x A^2(x)}{4m_e \gamma c^2} \left(1 + \frac{1-\epsilon^2}{1+\epsilon^2} \cos 2\omega t \right), \quad (12)$$

showing that the oscillating component vanishes for circular polarization ($\epsilon = 1$).⁷

The integral over x of $n_e f_{px}$, where $f_{px} = \langle f_x \rangle = \langle -e(\mathbf{v} \times \mathbf{B}/c)_x \rangle$ is the steady ponderomotive force density on electrons, equals the total radiation pressure on the target surface. For circular polarization and normal incidence we thus expect radiation pressure to push the target while electron heating is quenched. These conditions have been investigated in order to optimize radiation pressure acceleration of ions versus other mechanisms driven by hot electrons; see Sec. IV.A.

⁶This numerical implementation basically corresponds to the pioneering, elementary model of plasma simulation formulated by Dawson (1962).

⁷A more detailed analysis shows that electron heating is quenched when the parameter ϵ exceeds some threshold value; see Rykovanov *et al.* (2008) and Macchi, Liseikina *et al.* (2009).

2. Simulations, multidimensional effects, and simple estimates

A more quantitative description of laser absorption and hot electron generation requires numerical simulations. To address electromagnetic effects in his model Brunel (1988) performed two-dimensional (2D) PIC simulations in a plane wave, oblique incidence geometry. Several later studies using 1D simulations with the “boosted frame” technique (Bourdier, 1983) are summarized and reviewed by Gibbon *et al.* (1999). The absorption degree of a P -polarized laser pulse is quite sensitive to the incidence angle and the density scale length, with the latter varying on the time scale of ion motion (Gibbon, 1994) yielding a time-dependent absorption. Experimental attempts (Flacco *et al.*, 2008; McKenna *et al.*, 2008; Batani *et al.*, 2010) have been made to vary the density scale length in order to increase absorption in hot electrons and consequently to enhance ion acceleration (see Sec. III.E). Hot electron generation tends to become more efficient for lower plasma densities and, particularly, close to the critical density n_c , as it is observed that stronger coupling and volumetric heating occurs near the transmission threshold. A “near-critical” plasma may be produced either by the laser prepulse or by using a special target material, e.g., a low-density foam (see Sec. IV.D).

2D simulations reveal additional effects, as for instance the deformation of the plasma surface due to “hole boring” (HB) driven by radiation pressure (see also Sec. IV.A.1), which changes the local incidence angle (Wilks *et al.*, 1992), leading to increased absorption and providing a dynamic “funnel” effect collimating the electron flow inside the target (Ruhl *et al.*, 1999). A similar dynamics occurs in microcone targets which have proved to be effective in enhancing hot electron generation (Sentoku *et al.*, 2004; Nakamura *et al.*, 2009; Gaillard *et al.*, 2011, and references therein).

Absorption is also sensitive to small-scale surface deformations, either self-generated or preimposed, so that the use of microstructures on the front target surface has also been suggested as a way to enhance hot electron generation; see, e.g., Klimo *et al.* (2011), and references therein. Another possible approach is the use of grating surfaces where the resonant excitation of surface plasma waves can also lead to very high absorption (Raynaud *et al.*, 2007; Bigongiari *et al.*, 2011).

The high sensitivity of hot electron generation to laser and plasma parameters partly accounts for data scatter and differences observed in the many experimental investigations reported in the literature, with the above mentioned prepulse effects bringing additional complexity. For these reasons, absorption values and characteristics of the hot electron distribution are often taken into account in a phenomenological way. It has often been considered acceptable to assume the hot electron distribution to be Maxwellian with a temperature T_h given by Eq. (6) as a function of the laser irradiance. Figure 6 presents a collection of temperature measurements obtained for subpicosecond pulses up to the year 2000 (Gibbon, 2005b); these data broadly support a scaling of T_h as $(I\lambda^2)^{1/2}$. The total fractional absorption in hot electrons η_h is usually estimated to be in the 10%–30% range, with experimental indications of possibly quite higher values at ultrarelativistic intensities (Ping *et al.*, 2008).

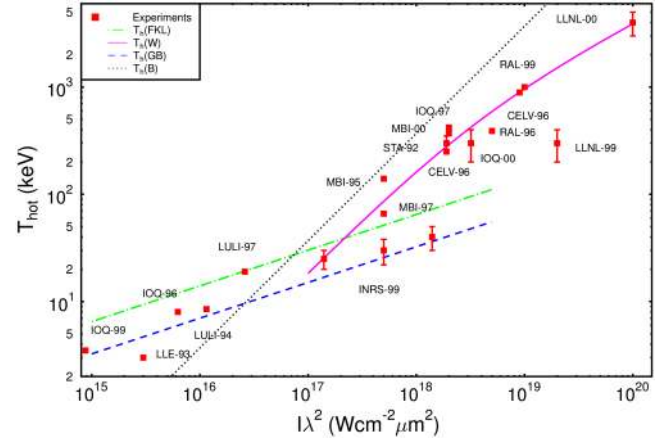


FIG. 6 (color online). Hot electron temperature as a function of irradiance from experiments of sub-ps laser-solid interaction. See Table 5.2 in Gibbon (2005b) for details on experimental parameters, diagnostic methods, and references. The lines give scaling laws derived from different models [FKL: Forslund, Kindel, and Lee (1977); W: Wilks *et al.* (1992); GB: Gibbon and Bell (1992); B: Brunel (1987)]. From Gibbon, 2005b.

An energy flux balance condition such as $\eta_h I \approx n_h v_h T_h$ (with $v_h \approx c$ at ultrahigh intensities) may then be used to estimate the “initial” density of hot electrons n_h , which usually is not larger than n_c , consistently with the argument that n_h cannot exceed the density of the region where hot electrons are generated.

Inside the target, the effective density may become different from the above estimate for n_h under particular conditions due to, e.g., the angular divergence of the electron flow or to electron refluxing effects depending on the electron time of flight and recirculation and thus on the target thickness (Mackinnon *et al.*, 2002). Still one can roughly estimate the total number of hot electrons N_h by an energy balance relation $N_h \sim \eta_h U_L / T_h$, where U_L is the energy of the laser pulse. The angular divergence θ_{div} is also estimated from experiments to range between 20° and 60° and to increase with irradiance (Green *et al.*, 2008, and references therein), although such estimates might depend on the accuracy of the sheath field modeling (Ridgers *et al.*, 2011).

3. Hot electron transport in solid matter

Transport of hot electrons in solid matter has been extensively investigated also because of its relevance to the electron-driven fast ignition (FI) scheme in inertial confinement fusion (ICF) [see Freeman *et al.* (2006) for a survey]. Key issues characterizing this regime are the very high values of the currents and the effect of self-generated fields. From the above estimates it can be inferred that near the front surface of the target the current density $\mathbf{j}_h = -en_h v_h$ associated to hot electrons may reach values up to $j_h \sim en_c c \approx 4.8 \times 10^{12} \text{ A cm}^{-2}$, corresponding to a total current of $\sim 15 \text{ MA}$ over a circular spot of $10 \text{ }\mu\text{m}$ radius. This large current must be locally neutralized by a return current \mathbf{j}_r such that $\mathbf{j}_h + \mathbf{j}_r \approx 0$; otherwise, either the electric field generated by the charge unbalance or the magnetic field generated by the free flowing current \mathbf{j}_h would be strong enough to stop the

hot electrons (Davies *et al.*, 1997; Passoni *et al.*, 2004). The free, cold electrons contributing to the return current are either present as conduction electrons in metals or produced by field and collisional ionization in insulators (Tikhonchuk, 2002). Additional complexity is introduced by effects such as target heating and hot electron refluxing, which have been inferred in several experiments (Bellei *et al.*, 2010; Nilson *et al.*, 2011; Quinn *et al.*, 2011, and references therein). Filamentation instabilities and dependence on the target material have also been extensively studied (Fuchs *et al.*, 2003; Manclossi *et al.*, 2006; McKenna *et al.*, 2011, and references therein). Simulation models accounting for both collisional effects and self-consistent generation of quasistatic fields are needed for quantitative investigations.⁸ Finally, it is noticeable that at least a fraction of hot electrons propagates coherently through the target conserving the temporal periodicity of the driving force, i.e., as bunches with ω or 2ω rate depending on incidence angle and polarization, as inferred by optical transition radiation measurements (Popescu *et al.*, 2005).

C. Ion acceleration mechanisms

In this section we give an overview of ion acceleration mechanisms including both those proposed to explain early experimental results in solid targets and those investigated later, either following inspiration from theoretical work or testing novel target designs. Some of the mechanisms described and the target regions where they are active are indicated in Fig. 7. Ion acceleration models will be described more in detail in Secs. III and IV along with the most relevant experiments.

1. Rear surface acceleration

As outlined in Sec. II.B, a very intense current of high-energy hot electrons may be generated at the front side of the target and eventually reach the rear side. There, as the hot electrons cross the rear side boundary and attempt to escape in vacuum, the charge unbalance generates a sheath field E_s , normal to the rear surface. Since E_s must backhold electrons with a typical “temperature” T_h , the typical spatial extension of the sheath L_s will be related to E_s by

$$eE_s \sim \frac{T_h}{L_s}. \quad (13)$$

From dimensional arguments, assuming a steep interface and n_h and T_h as the only parameters, L_s may be roughly estimated as the Debye length of hot electrons, $L_s \sim \lambda_{Dh} = (T_h/4\pi e^2 n_h)^{1/2}$. Assuming the simple scalings of Sec. II.B for T_h , taking a laser irradiance $I\lambda^2 = 10^{20} \text{ W cm}^{-2} \mu\text{m}^2$ and a fractional absorption $\eta_h = 0.1$, we find $T_h \approx 5.1 m_e c^2 = 2.6 \text{ MeV}$, $n_h \sim 8 \times 10^{20} \text{ cm}^{-3}$, $\lambda_{Dh} = 4.2 \times 10^{-5} \text{ cm}$, and $E_s \sim 6 \times 10^{10} \text{ V cm}^{-1}$. This large field will backhold most of the escaping electrons, ionize atoms at the rear surface, and

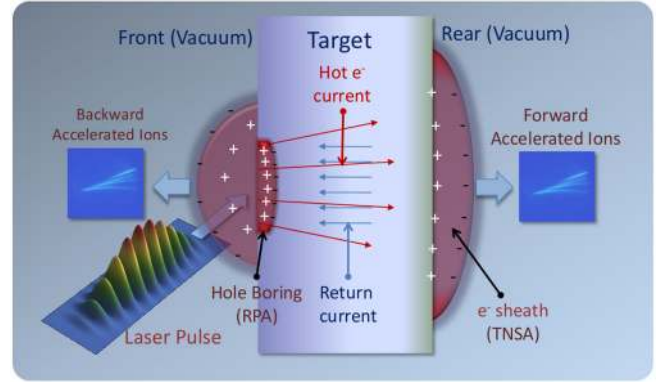


FIG. 7 (color online). Cartoon showing some of the possible acceleration mechanisms in the interaction with a thick solid target, including TNSA at the rear side (see Sec. II.C.1), hole boring RPA at the front side (see Sec. II.C.2), and backward acceleration in the plasma blowoff [see, e.g., Clark *et al.* (2000b)]. Also shown are the hot electron flow leading to sheath formation and expansion at the rear side and the associated return current.

start to accelerate ions. As a rough estimate, a test ion crossing the sheath would acquire the energy $\mathcal{E}_i \sim ZeE_s L_s = ZT_h$, resulting in MeV energies and a scaling as $I^{1/2}$ if $T_h \approx \mathcal{E}_p$ given by Eq. (6) holds. Protons from a thin layer of hydrogen-containing impurities on the surface will be in a very favorable condition for acceleration because of both their initial position, located at the maximum of the field, and their highest charge-to-mass ratio so that they will be more rapid than heavier ions in following electrons and screening the sheath field. This is the qualitative scenario for TNSA of protons as introduced by Wilks *et al.* (2001) to explain their experimental results on proton acceleration (Hatchett *et al.*, 2000; Snavely *et al.*, 2000).

The essential features of the TNSA mechanism have been supported by several experiments and TNSA has become the reference framework to interpret observations of multi-MeV protons from the target rear side. Various schemes for beam optimization and control have been designed on the basis of TNSA. Detailed discussions of main experimental findings are reported in Secs. III.A, III.B, and III.E.

From a theoretical viewpoint, there are two main categories of models which describe TNSA, namely, “static” and “dynamic” models which, depending on the starting assumptions, allow one to provide simplified analytical descriptions useful for interpreting experimental data. These models and related numerical investigations are presented in Sec. III.C.

2. Front surface acceleration

Already in the first measurements of proton acceleration in the forward direction, the possibility of a contribution originating at the front surface of the target was conceived (Clark *et al.*, 2000a; Maksimchuk *et al.*, 2000). As a consequence, mechanisms leading to ion acceleration in such a region have also been extensively investigated.

At the front surface, the intense radiation pressure of the laser pulse pushes an overdense target inward, steepening the density profile and bending the surface; this process is commonly named hole boring. The recession velocity v_{HB} of the plasma surface

⁸See, e.g., Gremillet, Bonnaud, and Amiranoff (2002), Bell *et al.* (2006), Evans (2007), Klimo, Tikhonchuk, and Debayle (2007), Solodov *et al.* (2009), and Kemp, Cohen, and Divol (2010), and references therein.

may be estimated by balancing the electromagnetic and mass momentum flows $I/c \sim n_i(m_i v_{\text{HB}})v_{\text{HB}}$. This corresponds to an energy per nucleon $\mathcal{E}_i = m_p v_{\text{HB}}^2/2 \sim I/An_i c$. The scaling with the laser intensity I is more favorable than the $I^{1/2}$ scaling for TNSA and suggests that RPA effects should become more important for higher intensities. More accurate, relativistic, and dynamic modeling is presented in Sec. IV.A.1 along with related experimental indications.

Radiation pressure action and hot electron temperature may also lead to the generation of collisionless shock waves (Tidman and Krall, 1971) with high Mach number M . Such waves are associated with the reflection of ions from the shock front, resulting in a velocity $v_i = 2Mc_s$ and an energy per nucleon $\mathcal{E}_i = 2m_p M^2 c_s^2 = 2(Z/A)M^2 T_h$, being $c_s = \sqrt{ZT_h/Am_p}$ the ion sound velocity. Such a CSA scenario and related experiments are discussed in Sec. IV.B.

Finally, the possibility of front side (or bulk) acceleration being favored by resistivity effects is discussed in Sec. IV.E.

3. Acceleration schemes using innovative targetry

Both TNSA and RPA can have different features in targets having peculiar geometrical and physical properties, if compared to the solid targets used in the 2000 experiments (Clark *et al.*, 2000a; Maksimchuk *et al.*, 2000; Snavely *et al.*, 2000) which had thickness in the 1–100 μm range and were much wider than the laser spot diameter. Experimental investigations of “ultrathin,” submicrometric targets require extremely “clean,” prepulse-free pulses to avoid early target evaporation and thus became possible only recently thanks to the development of advanced pulse cleaning techniques (see Sec. III.E). The use of “mass-limited” targets which also have limited lateral dimensions (in the sub-mm range) allows the refluxing and concentration of hot electrons in a small volume and may lead to higher ion energies via TNSA. These studies are presented in Sec. III.E.

For RPA, a sufficiently thin foil target is expected to be accelerated as a whole. Assuming the foil to be a perfect mirror of thickness ℓ , its nonrelativistic motion may be simply described by $m_i n_i \ell dV/dt = 2I/c$ from which we obtain an energy $\mathcal{E}_i = m_i V^2/2 = (2/m_i)(F/n_i \ell c)^2$, where $F = \int I dt$ is the laser pulse fluence. This is the basis of the “light sail” (LS) regime of RPA (see Sec. IV.A.2) which seems very promising in view of the foreseen fast scaling and the intrinsic monoenergeticity.

For extremely thin (a few nm) targets, the breakthrough of the laser pulse through the foil due to relativistic transparency may stop LS-RPA, but at the same time lead to additional strong heating of electrons. This effect opens up a regime of possible enhanced acceleration (BOA), which will be discussed in Sec. IV.C.

In general, reducing the effective size of the target allows for laser pulse penetration, volumetric heating, and energy confinement, which can lead to efficient ion acceleration even at low laser pulse intensities. As a well-known example, the interaction of ultrashort, moderate intensity ($\approx 10^{16} \text{ W cm}^{-2}$) pulses with subwavelength clusters allowed acceleration of ions up to energies sufficient to produce nuclear fusion reactions (Ditmire *et al.*, 1997, 1999). A limitation on the use of such clusters as ion

sources is the isotropic ion emission and the resulting low brilliance. “Droplet” targets with size of the order of one wavelength have been investigated as a trade-off approach, as discussed in Sec. III.E.2.

As mentioned previously, special target materials may be used to produce plasmas with density close to n_c (for laser wavelengths $\lambda \sim 1 \mu\text{m}$) in order to enhance the generation of hot electrons which drive TNSA (see Sec. IV.D). Gas jet targets have also been used both with $\lambda \sim 1 \mu\text{m}$ lasers to investigate ion acceleration in underdense plasmas (see Sec. IV.D) and with CO_2 lasers ($\lambda \sim 10 \mu\text{m}$) for studies of RPA and CSA in moderately overdense plasmas (see Secs. IV.A and IV.B). Apart from the possibility to vary the background density, using flowing gas jets as targets is of interest because they enable the interaction with a pure proton plasma and are suitable for high-repetition rate operation as needed for most foreseen applications (see Sec. V).

D. Particle-in-cell simulations

The PIC method (Dawson, 1983; Birdsall and Langdon, 1991), mentioned in the Introduction, is the most widely used approach to the kinetic simulation of plasmas. The PIC method provides a solution to the Maxwell-Vlasov system using a Lagrangian approach, with fields and currents allocated on a fixed grid and the phase space represented by an ensemble of computational particles. Thus, the PIC method is mostly appropriate to describe collisionless laser-plasma interaction dynamics, although models are available to implement either collisions [see, e.g., Fiuza *et al.* (2011), and references therein] or ionization [see, e.g., Petrov, Davis, and Petrova (2009), and references therein].

PIC simulations of laser interaction with solid-density plasmas at peak densities typically exceeding $10^2 n_c$ are a very demanding task even when the most powerful supercomputers are used. As a minimum requirement, one has to resolve temporal scales $\sim \omega_p^{-1}$ and spatial scales $\sim c/\omega_p$ where $\omega_p \sim n_e^{1/2}$. Thus, when approaching parameters of a real experiment, relevant lengths such as the laser beam waist may correspond to thousands of grid points in each spatial direction and typical dynamic times to thousands of time steps. In addition, kinetic effects such as the generation of hot electron tails in the distribution function and large density variations need very large numbers of particles to be properly resolved. For these reasons, realistic 3D simulations with proper resolution are typically beyond computational possibilities. These constraints result, in most of the cases, in either using a reduced dimensionality or in relaxing the actual parameters to some extent, e.g., by assuming relatively low densities or short scales. For some peculiar problems, development of hybrid modeling may be appropriate, as discussed in Sec. III.C.4.

Despite the above mentioned limitations, several groups have been able to perform large-scale 3D simulations relevant to ion acceleration regimes such as, e.g., TNSA (Pukhov, 2001), RPA (Esirkepov *et al.*, 2004; Tamburini *et al.*, 2012), and BOA (Yin *et al.*, 2011a). The use of parallel supercomputers has also allowed extended multiparametric studies (see Fig. 8) aimed to infer scaling laws and to provide

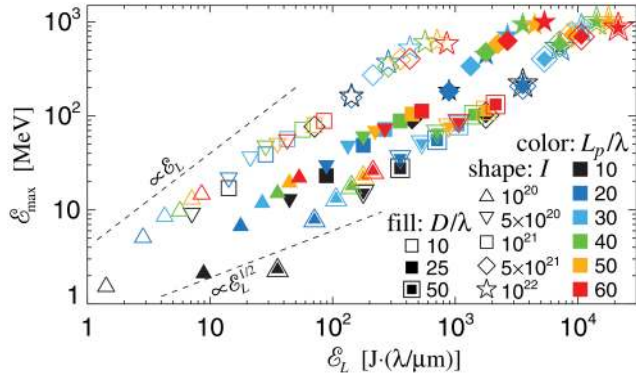


FIG. 8 (color online). Results from multiparametric 2D simulations for a double layer target (Esirkepov *et al.*, 2002; Esirkepov, Yamagiwa, and Tajima, 2006). The maximum energy of protons accelerated from the rear layer is shown as a function of laser pulse energy \mathcal{E}_L and for different values of the intensity I , pulse length L_p , and focal spot diameter D . The target density and thickness are $n_e = 100n_c$ and $\ell = \lambda$, respectively. From Esirkepov, Yamagiwa, and Tajima, 2006.

evidence for a transition from TNSA to RPA dominance at high intensities (Esirkepov, Yamagiwa, and Tajima, 2006). These and other numerical results will be discussed in Secs. III and IV.

E. Ion diagnostics

The specific properties of laser-driven ion beams (e.g., broad spectrum, high flux, significant divergence) have required either modifications of established diagnostics techniques or the development of new ones.

Radiochromic film (RCF) (McLaughlin *et al.*, 1996) is a detector which is favored by many experimenters, since the early work by Snavely *et al.* (2000), mainly due to simplicity of use. This is a high-dose, high-dynamic range film, widely used in medical context for x-ray dosimetry (Niroomand-Rad *et al.*, 1998). The films consist of one or more active layers containing a microcrystalline monomeric dispersion buried in a clear plastic substrate. Typical examples are the MDV3 and EBT2 Gafchromic varieties. After interaction with ionizing radiation, the active material undergoes polymerization and the film changes its color from nearly transparent to blue. The consequent change in optical density can be calibrated against the dose released in the film, and therefore provide information on the flux of particles directed at the layer. Typically, RCFs are used in a stack arrangement, so that each layer acts as a filter for the following ones in the stack. The signal in a given layer will be due only to ions having energy $E \geq E_B$, where E_B is the energy of the ions which reach their Bragg peak within the layer (see Fig. 9). In the first approximation, for an exponential-like spectrum such as those typically produced by TNSA, the dose deposited in a layer can be taken as proportional to the number of protons with $E \sim E_B$, allowing a rough spectral characterization of the beam. Various, more refined procedures have been developed for deconvolving the spectral information (either integrated across the beam or angularly resolved) in multilayer RCF data (Breschi *et al.*, 2004; Hey *et al.*, 2008; Nuernberg *et al.*, 2009; Kirby *et al.*, 2011).

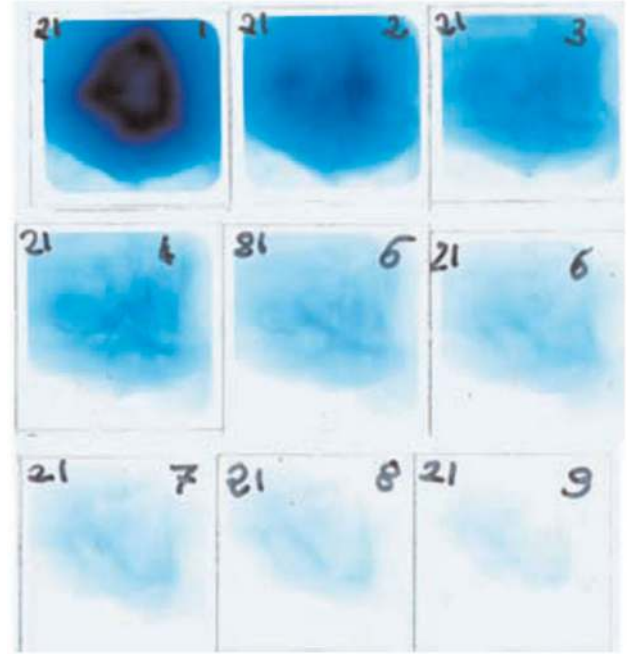


FIG. 9 (color online). A typical RCF stack obtained in an experiment with the TARANIS laser at Queen's University, Belfast. Higher numbers correspond to higher energy protons with layer 1 corresponding to ~ 1 MeV and layer 9 to ~ 12 MeV. From Dzelzainis *et al.*, 2010.

Plastic track detectors such as CR39 (Enge, 1995), which have the advantage of being insensitive to x rays and electrons, have been widely used also in multistack arrangements, e.g., by Clark *et al.* (2000a). CR39 layers (typically 0.25–1 mm in thickness) require etching in a NaOH solution after exposure to ions, so that the damage tracks created by the particles can be revealed thanks to the different etching rate in the track compared to the undamaged bulk (Sèguin *et al.*, 2003). After etching, the single tracks can be counted, which provides a direct measurement of the number of protons hitting the detector. CR39 works better for low particle fluxes, as at high flux (typically above $\sim 10^8$ particles cm^{-2}) or for long etching times the tracks start to overlap, leading to saturation (Gaillard *et al.*, 2007).

The interaction of laser-driven high-energy ions with secondary targets can initiate a number of nuclear reactions (see Sec. V.E), which can be used to diagnose the beam properties with the ability to provide absolute particle numbers with a linear response and virtually no saturation at high flux. The $^{63}\text{Cu}(p, n)^{63}\text{Zn}$ reaction in copper stacks has been used to quantify the proton numbers through measurement of β^+ decay of ^{63}Zn nuclei, using a NaI detector-based coincidence counting system (Santala *et al.*, 2001; Spencer *et al.*, 2001). Techniques employing a single Cu layer, in which a range of isotopes resulting from proton-induced nuclear reactions is analyzed in order to reconstruct the proton spectrum, have also been used (Yang *et al.*, 2004b). Spectral resolution is provided by a combination of filtering and known thresholds for the considered reaction. The above described approaches provide particle flux integrated over the whole beam cross section. Contact radiography of (p, n) -generated isotopes in activation samples (where the activated foil is placed in contact with RCF) has been

developed (Clarke *et al.*, 2008; Offermann *et al.*, 2010) as a way to achieve 2D images of the beam profile with high spatial resolution and extremely high-dynamic range. Neutron spectra produced through fusion reactions of the type $D(d,n)^3\text{He}$ have been used as a diagnostic of laser-driven deuterium ions inside a laser-irradiated target (Habara *et al.*, 2003, 2004a, 2004b).

Obtaining spectra with high-energy resolution requires the use of magnetic dispersion techniques. In simple magnetic spectrometers [see, e.g., H. Chen *et al.* (2008)] the ions, spatially selected by an entrance slit or pinhole, are dispersed along one spatial direction according to their energy by a ~ 1 T magnetic field \mathbf{B} . This arrangement, which discriminates particles according to their energy but not to their charge-to-mass ratio, is adequate for diagnosing the high-energy proton spectrum in “standard” TNSA experiments in which protons are the dominant accelerated species (Hegelich *et al.*, 2002).

A more complete spectral characterization of multicomponent ion beams can be obtained with Thomson parabola spectrometers, based on the principle for mass spectrometry introduced by Thomson (1911). A schematic of the device is shown in Fig. 10(a). Ions are deflected by parallel \mathbf{E} and \mathbf{B} fields [with $E \sim 10^4$ V/m (Sakabe *et al.*, 1980)] resulting in a characteristic deflection pattern in which species with different charge-to-mass ratio form separated parabolic traces in the detector plane, as shown in the typical image of Fig. 10(b). Modified magnetic and Thomson spectrometers, having imaging and angular resolution capability, have also been developed (Ter-Avetisyan *et al.*, 2009; Chen *et al.*, 2010; Jung *et al.*, 2011a).

The detectors used in conjunction with these spectrometers are typically either CR39, image plates (IP), scintillating plates, or microchannel plates (MCPs). Photostimulable IPs are filmlike radiation image sensors, developed for x-ray medical imaging, which are composed of specially designed phosphors that trap and store radiation energy in metastable excited states and can be absolutely calibrated in terms of particle flux (Mančić *et al.*, 2008; Freeman *et al.*, 2011). Scintillating plates (Green *et al.*, 2010) or MCPs (Ter-Avetisyan, Schnrer, and Nickles, 2005) are favored in situations where online detection is required (e.g., high-repetition laser systems), as the scintillator screen or the MCPs phosphor are imaged on a charge-coupled device (CCD) and the detector does not require replacing after exposure. Scintillators can also be used for beam profiling (Sakaki *et al.*, 2010), with potential for energy range selection (Green *et al.*, 2011).

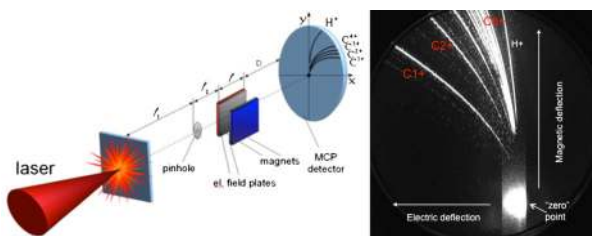


FIG. 10 (color online). Left: Schematic of a Thomson parabola (courtesy of S. ter-Avetisyan). Right: A typical example of ion traces obtained with the Thomson parabola.

A different approach also allowing online beam monitoring is the use of time-of-flight (TOF) techniques, where the broadband ions are left to propagate over a given distance and then detected employing scintillating plates coupled to a photomultiplier (Nakamura *et al.*, 2006), Faraday cups, or semiconductor detectors (Margarone *et al.*, 2011). The time-varying signal produced by the detectors maps the ion energy spectrum, although the finite response time of the detector and realistic propagation distances limits the energy range over which these measurements can be applied. State-of-the-art TOF-MCP detectors allow for measurements of protons with a kinetic energy up to ~ 20 MeV/nucleon (Fukuda *et al.*, 2009).

III. TARGET NORMAL SHEATH ACCELERATION

A. TNSA scenario: Main experimental observations

As anticipated in Sec. II.C the TNSA process (Wilks *et al.*, 2001) is a consequence of the large charge separation generated by hot electrons reaching the rear side of the target. There, a cloud of relativistic electrons is formed, extending out of the target for several Debye lengths, and giving rise to an extremely intense electric field, mostly directed along the normal to the surface. A consequent distinctive feature is that ions are accelerated perpendicularly to the surface, with high beam collimation. The electric field generated at the rear surface depends on parameters of the electron distribution (temperature, number, divergence) as well as of the surface (mostly its density profile as detailed below).

The acceleration is most effective on protons, which can be present either in the form of surface contaminants or among the constituents of the solid target as in plastic targets. The heaviest ion populations provide a positive charge with much more inertia, thus creating the charge separation which generates the accelerating field. Part of the heavy population can also be effectively accelerated, on a longer time scale, if the proton number is not high enough to balance the charge of the escaping hot electrons, and especially if impurity protons are removed before the interaction, for example, by preheating the target (Hegelich *et al.*, 2002). In this way, ions of several different species may be accelerated (Hegelich *et al.*, 2005).

Several observations strongly supported the TNSA scenario taking place at the rear side. Already Snively *et al.*

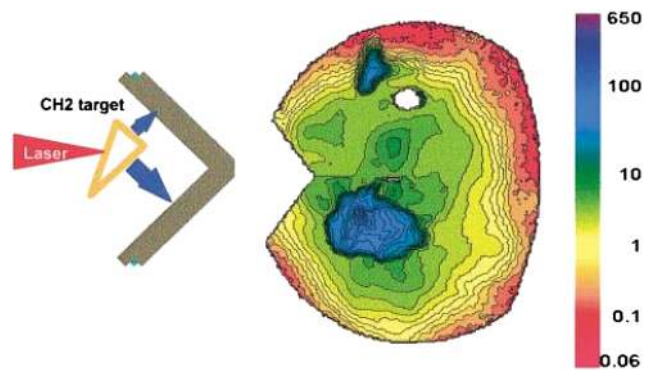


FIG. 11 (color online). Proton emission from a wedge target effectively having two rear surfaces. Two separate spots are produced on the detector, showing that most of the protons originate from the rear side of the target. From Snively *et al.*, 2000.

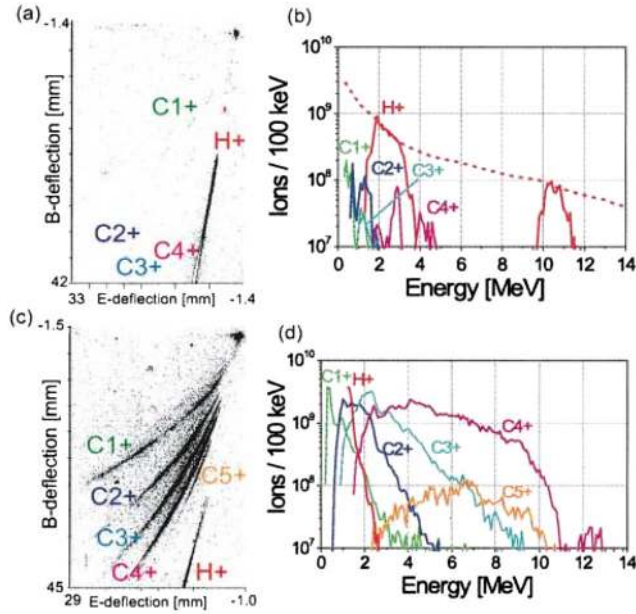


FIG. 12 (color online). Effect of impurity removal on carbon ion spectra. (a) and (b) show C ions traces (from CR-39 track detectors) and spectra from Al foils coated with a C layer on the rear side, in the presence of hydrocarbon contaminants on the surface. In (c) and (d), the contaminants had been previously removed by resistive heating. From Hegelich *et al.*, 2002.

(2000) gave clear evidence that the emission was normal to the rear surface using wedge targets which effectively have more than one rear surface. Two separate proton beams were observed in the directions normal to the two rear surfaces of the wedge (see Fig. 11).

Mackinnon *et al.* (2001) reported experimental observations of the interaction of ultraintense laser pulses using targets with and without preformed plasmas on the rear surface of the foil. The peak and mean energies of the proton beam were found to strongly depend on the plasma scale length at the rear of the target. While an energetic proton beam was obtained with an unperturbed rear surface, no evidence of high-energy protons was recorded when a large local scale length in the ion density at the rear surface was induced, consistently with the dependence of the accelerating field on the scale length in Eq. (13).

Hegelich *et al.* (2002) used Al and W foils as targets, resistively heated to remove hydrogen contaminants and coated on the rear side with thin C and CaF_2 layers,

respectively. The observation of high-energy C, Ca, and F ions from these prepared source layers proves the existence of an effective rear surface acceleration mechanism (see Fig. 12). Further evidence was provided by Allen *et al.* (2004) who showed that removing contamination from the back surface of Au foils strongly reduced the total yield of accelerated protons, while removing contamination from the front surface of the target had no observable effect on the proton beam.

Further proof that ions are accelerated at the rear side was given by the observation that a structuring (i.e., grooving) of the rear surface produced modulations in the proton beam (Cowan *et al.*, 2004). This effect also evidences the high laminarity of the beam and allows one to measure its emittance, as discussed in Sec. III.B.

Direct experimental evidence of the generation of an initial intense sheath field at the rear surface and a late time field peaking at the beam front was provided by Romagnani *et al.* (2005) using the proton imaging technique (see Sec. V.A). In this case, TNSA itself provided a unique diagnostic which allowed direct experimental confirmation of the nature of the acceleration process. Figure 13 shows a temporal series of “proton images” in which the propagation of the bell-shaped front of ion expansion can be observed.

More recent developments have shown the possibility to significantly control and optimize the TNSA process by acting on the detailed properties of both the laser pulse and the irradiated target. These developments have also highlighted the capability of achieving interesting and promising variations of the main scheme, also in light of possible specific applications. These topics will be presented in Sec. III.E.

B. Characterization of beam properties

Several experiments have investigated in detail the properties of the TNSA ion beams. The energy spectrum of the beams is typically broadband, up to a cutoff energy (see Fig. 2). The particle number per MeV can be roughly approximated by a quasithermal distribution with a sharp cutoff at a maximum energy (Kaluza *et al.*, 2004; Fuchs *et al.*, 2005) which scales with the laser parameters as discussed in Sec. III.D. Many experiments have reported spectral observations for a wide range of laser and target parameters, and partial surveys have been provided in a

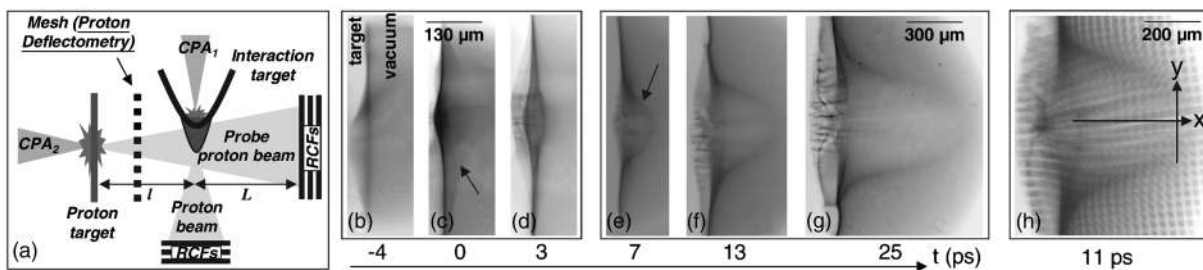


FIG. 13. Proton probing of the expanding sheath at the rear surface of a laser-irradiated target. (a) Setup for the experiment. A proton beam is used as a transverse probe of the sheath. (b)–(g) Temporal series of images produced by the deflection of probe protons in the fields, in a time-of-flight arrangement. The probing times are relative to the peak of the interaction. (h) A deflectometry image where a mesh is placed between the probe and the sheath plasma for a quantitative measure of proton deflections. From Romagnani *et al.*, 2005.

number of publications (Borghesi *et al.*, 2006; Fuchs *et al.*, 2006b; Zeil *et al.*, 2010).

A number of experimental studies have been devoted to the investigation of the spatial and angular characteristics of the emitted beams. These are closely dependent on the electron sheath spatial distribution, and consequently on the target properties (resistivity, surface roughness, etc.) affecting the electron propagation.

It was observed early on that the use of conducting targets leads to smooth proton beam profiles with a sharp boundary, as detectable, for example, in RCF data (Snively *et al.*, 2000; Fuchs *et al.*, 2003), while using dielectric targets creates nonhomogeneities in the proton density across the beam section. In the latter case, the transport of the electron current is prone to electromagnetic instabilities, which break the hot electron flow into filaments. This leads to an uneven electron sheath at the target rear (Manclossi *et al.*, 2006) and consequently to a modulated proton beam cross section (Roth *et al.*, 2002; Fuchs *et al.*, 2003). The close correlation between proton beam properties and electron beam transport characteristics has indeed been exploited in a number of experiments, which have used the proton beam as a diagnostic for the electron beam behavior inside the target, revealing, beside the aforementioned differences related to the target conductivity (Fuchs *et al.*, 2003), effects of magnetic collimation on the beam transport (Yuan *et al.*, 2010; Gizzi *et al.*, 2011) or the role of lattice structure in dielectric targets (McKenna *et al.*, 2011). Other factors that can lead to structured beam profiles even in conducting targets are surface roughness at the target rear, resulting in a randomized local orientation of the protons (Roth *et al.*, 2002), and intensity modulations in the focal spot which can be coupled to the protons via structured electron beams in medium- Z thin targets (Fuchs *et al.*, 2003).

The existence of a sharp angular boundary in the proton angular distribution (clearer in higher- Z and thicker targets) is consistent with a bell-shaped transverse distribution of hot electrons in the rear surface sheath due to the fact that the density will naturally be higher along the laser axis and decrease with transverse radius. Protons are accelerated normal to the local isodensity contour, and the presence of an inflection point in the sheath therefore results in a maximum angle of acceleration (Fuchs *et al.*, 2003). Comparison of experimental data with simple electrostatic models indicates that the shape of the accelerating sheath is generally Gaussian (Fuchs *et al.*, 2003; Carroll *et al.*, 2007) as also observed directly in sheath imaging data (Romagnani *et al.*, 2005); see Fig. 13.

A modulation of the proton beam angular distribution can be introduced purposefully by microstructuring the target surface. A technique based on micromachining shallow grooves on the rear surface of the target, introduced by Cowan *et al.* (2004), has successfully been used in several experiments for diagnosing the emission properties of the beam (Nuernberg *et al.*, 2009). From these patterned targets, a periodic modulation of the beam angular envelope arises during TNSA due to the local perturbation of the target normal direction, which causes an initial beam microfocusing at the groove locations. As the sheath expands, the local modulations are added over the global divergence of the

beam (Ruhl, Cowan, and Fuchs, 2004) and are observable as a modulation of the proton dose on the detector (see Fig. 14). The modulations can be used as a spatial fiducial from which one can infer the dimensions of the area from where ions are accelerated, i.e., the proton or ion source size (Brambrink *et al.*, 2006). Similar information has been obtained by considerations based on the projection by the ion beam of patterned objects, e.g., metal meshes (Borghesi *et al.*, 2004) or knife edges (Schreiber *et al.*, 2004).

A crucial property of laser-driven ion beams is their laminarity. In an ideal laminar source, there is a correlation between the location within the source from where a particle is emitted and the angle of emission. The degree of laminarity of charged-particle beams is typically expressed in terms of their transverse emittance, a quantity which is proportional to the area of the bounding ellipsoid of the distribution of particles in phase space (Humphries, 1990). The highest quality ion beams have the lowest values of transverse and longitudinal emittance, indicating a low effective transverse ion temperature and a high degree of angle space and time-energy correlation, respectively. Transverse emittance has been measured in a number of experiments. Methods based on mesh projection (which is broadly equivalent to the established “pepper-pot” method) indicate that the emittance is less than 0.1π mm mrad (Borghesi *et al.*, 2004; Ceccotti *et al.*, 2008; Nishiuchi *et al.*, 2008). The above discussed groove imaging technique allows a full reconstruction of the transverse phase space, and possibly a more precise estimation of the transverse emittance (Cowan *et al.*, 2004; Brambrink *et al.*, 2006; Nuernberg *et al.*, 2009) which, for protons of up to 10 MeV, has been estimated as 0.004 mm mrad, i.e., 100-fold better than typical rf accelerators and at a substantially higher ion current (kA range).

It has also been found that the removal of the comoving electrons after 1 cm of the quasineutral beam expansion did not significantly increase the measured proton transverse

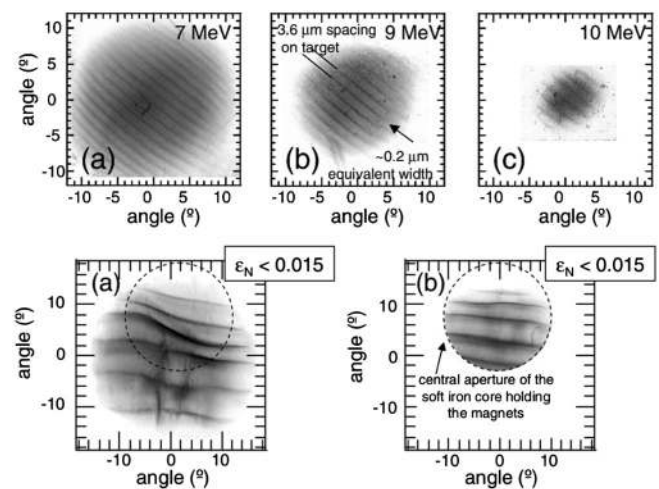


FIG. 14. Top: Modulations in the proton distribution, for different energies, on a RCF detector from a target with microgrooves imprinted on the rear side. The target is a $18\text{ }\mu\text{m}$ thick Al foil irradiated at 10^{19} W cm^{-2} . Bottom: The effect of electron removal by magnetic fields, showing that the proton beam emittance is not significantly affected. The images are for 6.5 MeV protons and the target thickness is $40\text{ }\mu\text{m}$. From Cowan *et al.*, 2004.

emittance, as shown in Fig. 14 (Cowan *et al.*, 2004). This last observation is important since, in order to take advantage of the exceptionally small proton beam emittance in future applications, e.g., to capture them into a postaccelerator, removal of the comoving electrons without significantly perturbing the protons is crucial.

The ultralow emittance stems from the extremely strong, transient acceleration that takes place from a cold, initially unperturbed surface and from the fact that during much of the acceleration the proton space charge is neutralized by the comoving hot electrons. Using the ion beam as a projection source, having a low-emittance beam is equivalent to projecting from a *virtual* pointlike source located in front of the target, with much smaller transverse extent than the ion-emitting region on the target surface (Borghesi *et al.*, 2004; Nuernberg *et al.*, 2009). As discussed in Sec. V.A, this property of laser-driven ion beams allows one to implement point-projection radiography with high spatial resolution.

C. TNSA modeling

The experimental observations and the considerations summarized in Sec. III.A suggest the following assumptions, leading to the formulation of a relatively simple system of equations which can be investigated analytically and numerically (Passoni *et al.*, 2004). First, we assume an electrostatic approximation, so that the electric field $\mathbf{E} = -\nabla\phi$ where the potential ϕ satisfies Poisson's equation

$$\nabla^2\phi = 4\pi e\left(n_e - \sum_j Z_j n_j\right), \quad (14)$$

with the sum running over each species of ions, having density n_j and charge Z_j . As a consequence of the laser-solid interaction, the electron density n_e may be described as composed of at least two qualitatively distinct populations, which will be labeled *cold* and *hot* in the following, having densities n_c and n_h such that $n_e = n_c + n_h$. In the simplest approach, thermal effects are neglected for the cold population, while n_h is given by a one-temperature Boltzmann distribution (notice that in this section “e” indicates the mathematical constant $e = \exp(1) = 2.71828 \dots$ while e indicates as usual the elementary charge),

$$n_h = n_{0h} e^{e\phi/T_h}. \quad (15)$$

This expression can be a reasonable first approximation to account for the presence of the self-consistent sheath field and has been used in many works on TNSA⁹ but, as discussed below, it can lead to serious problems when the main goal is the estimation of the maximum energy of the accelerated ions. Alternatively, the electron dynamics can be included via either fluid or kinetic equations. It is mostly appropriate to consider two different ion species, a light (L) and a heavy (H) population: in this way it is possible, e.g., to model the acceleration of light species present on the surfaces of a solid target made of heavy ions.

⁹See, e.g., Mora (2003), Passoni *et al.* (2004), Albright *et al.* (2006), Nishiuchi *et al.* (2006), and Robinson, Bell, and Kingham (2006).

Depending on the description of the ion populations, two main categories of TNSA models, to be discussed in detail in Secs. III.C.1 and III.C.2, respectively, may be identified as follows. The first includes *static* models in which it is assumed that the light ions, or at least the most energetic ones, are accelerated in the early stage of the formation of the sheath, so that the latter may be assumed as stationary. With these conditions, the effects of the light ions on the electrostatic potential are usually neglected, while the heavy ion population of the target is considered immobile. The aim is thus to provide the most accurate description of the sheath depending on assumptions on the hot electron distributions. The second category includes *dynamic* models where the system is described as a neutral plasma in which the ions acquire kinetic energy in the course of the sheath evolution. In several cases a unique ion component is considered. This approach is therefore strongly connected to the classic problem of plasma expansion in vacuum, first considered by Gurevich, Pariiskaya, and Pitaevskii (1966). In a cold fluid description, neglecting relativistic effects the ions are described by

$$\frac{\partial \mathbf{u}_j}{\partial t} + \mathbf{u}_j \cdot \nabla \mathbf{u}_j = -\frac{Z_j e}{m_j} \nabla \phi, \quad (16)$$

$$\frac{\partial n_j}{\partial t} + \nabla \cdot (n_j \mathbf{u}_j) = 0 \quad (j = L, H), \quad (17)$$

where $\mathbf{u}_j = \mathbf{u}_j(\mathbf{r}, t)$ is the fluid velocity. If the ions are described kinetically, their Vlasov equation for the phase-space distribution $f_j = f_j(\mathbf{r}, \mathbf{v}, t)$ is

$$\frac{\partial f_j}{\partial t} + \mathbf{v} \cdot \nabla f_j - \frac{Z_j e}{m_j} \nabla \phi \cdot \frac{\partial f_j}{\partial \mathbf{v}} = 0. \quad (18)$$

Most of the general studies of plasma expansion and related ion acceleration developed both before and after TNSA experiments¹⁰ as well as more specific models of TNSA¹¹ so far proposed in the literature can be considered as suitable simplifications of the previous equations, falling into one of the two above mentioned categories (or suitable combinations of them) and obtained adding further, physically motivated assumptions. Most of these models assume a 1D geometry, consistently with the electrostatic approximation, and planar in most cases. This latter assumption, when applied to TNSA modeling, requires the rear surface to be sufficiently flat and

¹⁰General studies of plasma expansion in vacuum include Gurevich, Pariiskaya, and Pitaevskii (1966), Allen and Andrews (1970), Widner, Alexeff, and Jones (1971), Crow, Auer, and Allen (1975), Pearlman and Morse (1978), Denavit (1979), Mora and Pellat (1979), and Dorozhkina and Semenov (1998). Early papers focused on modeling ion acceleration in laser-produced plasmas include Pearlman and Morse (1978), Wickens, Allen, and Rumsby (1978), True, Albritton, and Williams (1981), and Kishimoto *et al.* (1983). More recent works stimulated by the TNSA experiments include Kovalev and Bychenkov (2003), Mora (2003, 2005), Betti *et al.* (2005), Ceccherini *et al.* (2006), and Peano *et al.* (2007).

¹¹A list of papers describing TNSA models mostly based on a static modeling includes Passoni and Lontano (2004, 2008), Passoni *et al.* (2004), Albright *et al.* (2006), Lontano and Passoni (2006), Robinson, Bell, and Kingham (2006), and Schreiber *et al.* (2006).

the electron cloud to be spatially uniform in the plane normal to the ion motion.

Note that all the models proposed to describe TNSA are, to a large extent, phenomenological, i.e., they need as input parameters physical quantities which are not precisely known. Since these descriptions give a simplified picture of the acceleration process, the best model in this context may be considered the one which provides the best fit of experimental data with the lowest set of laser and target parameters. This issue will be discussed in Sec. III.D. In principle, these difficulties could be overcome performing realistic numerical simulations, but these generally consider “model” problems due to intrinsic difficulties in the numerical study of these phenomena, such as, for example, the large variations of density from the solid target to the strongly rarefied expansion front. At present, a complementary use of simple models, presented in Secs. III.C.1, III.C.2, and III.C.3, and advanced simulations, discussed in Sec. III.C.4, seems the most suitable option to theoretically approach TNSA.

1. Quasistatic models

Static models assume, on the time scale of interest (i.e., in the sub-ps regime), immobile heavy ions, an isothermal hot electron population, and a sufficiently low number of light ions so that their effect on the evolution of the potential can be neglected and they can be treated as test particles. In this limit, if Eq. (15) is used to describe hot electrons and one neglects thermal effects for cold electrons, the potential in planar geometry is determined by

$$\begin{aligned} \frac{\partial^2 \phi}{\partial x^2} &= 4\pi e [n_{0h} e^{e\phi/T_h} - (Z_H n_{0H} - n_{0c})] \\ &= 4\pi e n_{0h} [e^{e\phi/T_h} - \Theta(-x)], \end{aligned} \quad (19)$$

where we assumed the background charge to fill the $x < 0$ region with uniform density. The corresponding electron density and electric field can be calculated, as well as the energies of test ions moving in such potential. This can be considered the simplest self-consistent approach to describe the TNSA accelerating field. The solution of Eq. (19) in the semi-infinite region $x > 0$ is (Crow, Auer, and Allen, 1975)

$$\phi(x) = -\frac{2T_h}{e} \left[\ln \left(1 + \frac{x}{\sqrt{2e}\lambda_{Dh}} \right) - 1 \right], \quad (20)$$

where $\lambda_{Dh} = \sqrt{T_h/4\pi e^2 n_{0h}}$. The field reaches its maximum at the surface and is given by

$$E(0) = \sqrt{\frac{2}{e}} E_0, \quad E_0 = \frac{T_h}{e\lambda_{Dh}}, \quad (21)$$

which justifies the simple estimates used in Sec. II.C. However, the electrostatic potential (20) leads to an infinite acceleration of a test proton which is initially at zero energy in $x = 0$. The reason is that the apparently reasonable choice of the Boltzmann relation poses several difficulties to the analysis (Passoni and Lontano, 2004) because, in order to have an electron density equal to zero at infinity, the self-consistent electrostatic potential must diverge at large

distance from the target [mathematically, $\phi \rightarrow -\infty$ as $x \rightarrow +\infty$, see Eq. (15)]. This is not a pathological consequence of the one-dimensional approximation but it is related instead to the fact that the Boltzmann relation implies the existence of particles with infinite kinetic energy, which is not physically meaningful [see also Sec. 38 of Landau and Lifshitz (1980)]. This unphysical behavior can be avoided by assuming an upper energy cutoff \mathcal{E}_c in the electron distribution function, so that $e\phi \rightarrow -\mathcal{E}_c$ as $x \rightarrow +\infty$ and the electric field turns to zero at a finite distance. The cutoff assumption can be justified as a consequence of the laser-solid interaction producing electrons with a maximum kinetic energy and of the escape from the system of the most energetic ones (Lontano and Passoni, 2006; Passoni and Lontano, 2008). Experimental indications of target charging due to electron escape have been found by Kar *et al.* (2008b) and Quinn *et al.* (2009a). The finite range of the electric field driving TNSA is also apparent in direct measurements (Romagnani *et al.*, 2005).

Still using the Boltzmann relation, it can be assumed the 1D solution given by Eq. (20) to hold only up to a longitudinal distance roughly equal to the transverse size of the sheath, because at larger distances 3D effects should be taken into account (Nishiuchi *et al.*, 2006). Alternatively, by assuming that the hot electron population occupies only a finite region of width h , the solution of Eq. (19) in the vacuum region $0 < x < h$ together with the corresponding electric field and electron density can be determined (Passoni and Lontano, 2004).

Another possibility, explored by Schreiber *et al.* (2006), has been to heuristically assume that the hot electron expansion in vacuum creates a cylindrical quasistatic cloud in the vacuum, behind the target, and a circular positive surface charge on its rear face. The generated electrostatic potential is evaluated on the symmetry axis, along which the most energetic ions are accelerated. The total surface charge and the radius of the distribution are model parameters estimated from experiments (see also Sec. III.D).

In order to consistently overcome the previously discussed limits, Lontano and Passoni (2006) proposed to solve the Poisson equation by assuming that a quasistationary state is established where only those electrons (*trapped electrons*) with negative total energy $W = mc^2(\gamma - 1) - e\phi$ are retained, while those with positive total energy are lost from the system. The corresponding trapped electron density, given by $n_h = \int_{W<0} f_e(x, p) dp$, is included in the Poisson equation and the analytical solutions are determined (Lontano and Passoni, 2006; Passoni and Lontano, 2008; Passoni, Bertagna, and Zani, 2010b). As a general feature, the potential, the electrostatic field, and the electron density distributions go to zero at a finite position x_f of the order of several hot Debye lengths.

If both electron populations, hot and cold, are considered, it is possible to find an implicit analytical solution of Eq. (19) both inside the target and in the vacuum region. Using a two-temperature Boltzmann relation to describe the electron density, that is, $n_e = n_{0h} \exp(e\phi/T_h) + n_{0c} \exp(e\phi/T_c)$, the electric field profile turns out to be governed by the parameters $a \equiv n_{0c}/n_{0h}$ and $b \equiv T_c/T_h$, as shown in Fig. 15 (Passoni *et al.*, 2004). The presence of the cold

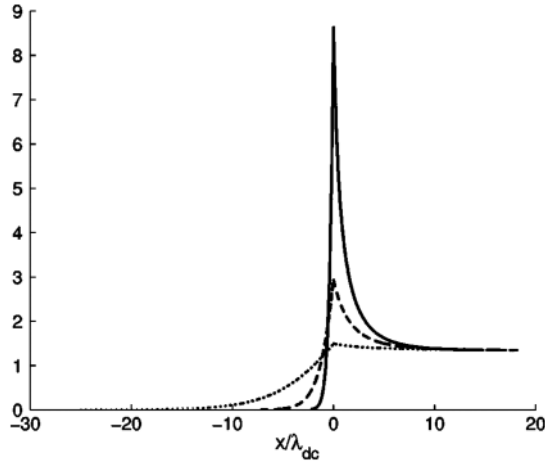


FIG. 15. Electric field profile in a sheath with two electron temperatures. The field is normalized to $T_h/e\lambda_{De}$ and is shown for cold-to-hot electron temperature ratio $b = T_c/T_h = 0.01$ and for different values of the pressure ratio $ab = p_{0c}/p_{0h} = 1$ (dotted line), $ab = 10$ (dashed line), and $ab = 100$ (solid line). The x coordinate is normalized to the cold electron Debye length λ_{De} corresponding to $ab = 10$. From Passoni *et al.*, 2004.

electron population strongly affects the spatial profiles of the field, which drops almost exponentially inside the target over a few cold electron Debye lengths. An estimate of T_c , as determined by the Ohmic heating produced by the return current (see Sec. II.B.3), is required. A simple analytical model of the process has been proposed (Davies, 2003; Passoni *et al.*, 2004), to which we refer for further details and results.

The quasistatic approach allows one to draw several general properties of the accelerating TNSA field. The spatial profile is characterized by very steep gradients, with the field peaking at the target surface and decaying typically over a few μm distance. The most energetic ions, accelerated in the region of maximum field, cross the sheath in a time shorter than the typical time scale for plasma expansion, electron cooling, and sheath evolution. As a consequence the static approximation will be more accurate for the faster ions. Assuming a time-independent field also requires the electron cloud to not be affected by the ions flowing through it, which implies a number of accelerated ions much smaller than that of the hot electrons, $N_i \ll N_e$. A quasistatic model not requiring this assumption was proposed by Albright *et al.* (2006) who included effects of the accelerated ion charge on the electric field by modeling the layer of light ions (having areal charge density Q_L) as a surface layer of density $n_L = (Q_L/Z_L e)\delta(x - x_L)$. Equation (19) is then solved as a function of the instantaneous position x_L . An extension of this model, using an adiabatic description of the hot electrons, was proposed by Andreev *et al.* (2008) to investigate the variation of the maximum light ion energy as a function of the heavy ion target thickness.

On the basis of the above discussion we expect static models to be most reliable for estimating the cutoff in the ion energy spectrum. This estimate requires a few parameters as input, depending on the model. This issue will be discussed in Sec. III.D.

2. Plasma expansion into vacuum

A description of ion acceleration over relatively long times and/or under conditions such that the quasistatic modeling of Sec. III.C.1 is not valid anymore demands for the inclusion of the ion dynamics. The description may be based either on a fluid model, using Eqs. (16) and (17), or on a kinetic one using Eq. (18).

The simplest approach is obtained using a 1D fluid approach, invoking quasineutrality, using Eq. (15) and assuming a single ion and electron population expanding in the semi-infinite space $x > 0$. Equation (19) is substituted by the simpler condition $n_e = Z_i n_i$, the index i denoting the single ion component. The boundary conditions are that the electron density should remain equal to the background value well inside the plasma, so that $n_e(-\infty) = n_0$, and should vanish in vacuum far from the surface, i.e., $n_e(+\infty) = 0$. Together with Eqs. (16) and (17), the resulting system admits the classical self-similar solution first found by Gurevich, Pariiskaya, and Pitaevskii (1966),

$$n_i = n_0 \exp\left(-\frac{x}{c_s t} - 1\right), \quad u_i = c_s + \frac{x}{t}, \quad (22)$$

where x/t is the self-similar variable, $L = n_i/|\partial_x n_i| = c_s t$ is the local density scale length, and the expressions are valid for $x > -c_s t$. The profiles corresponding to Eqs. (22) are sketched in Fig. 16.

As a consequence of the quasineutral approximation, the physical quantities describing the plasma dynamics present several diverging behaviors, such as the unlimited increase of u_i with x . This implies that the neutral solution must become invalid at some point, which can be estimated by equating the local density scale length L to the local Debye length λ_D . This provides $x_f(t) = c_s t [2 \ln(\omega_{pi} t) - 1]$, the corresponding velocity $u_f = dx_f/dt = 2c_s \ln(\omega_{pi} t)$, and the electric field at the ion front $E_f = E(x_f) = 2E_0/\omega_{pi} t$, where $E_0 = (4\pi n_0 T_h)^{1/2}$. This estimate gives twice the self-similar field $E = T_h/ec_s t$. The argument also defines the front of the fastest ions moving at velocity u_f and thus it gives also the high-energy cutoff in the energy spectrum of the ions in this description.

Equations (22) are also singular for $t \rightarrow 0$, i.e., at the earliest instants of the expansion, when quasineutrality also breaks down. In general, in the sub-ps regime

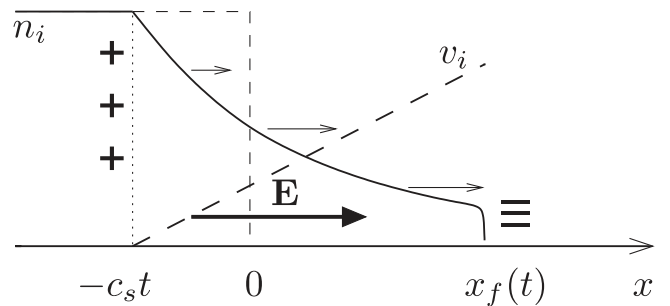


FIG. 16. Sketch of the density and velocity profiles from the self-similar solution for isothermal plasma expansion; Eq. (22). The front of charge separation at $x = x_f(t)$ and the rarefaction front at $x = -c_s t$ are also indicated. The electric field is uniform in the $-c_s t < x < x_f(t)$ region.

the inertia of ions is important and the assumption of quasineutrality must be abandoned. Ultimately, a self-consistent analysis can be developed through numerical simulations (see Sec. III.C.4). Still assuming, for simplicity, that only a single ion population and a single-temperature Boltzmann electron population are present, and $n_i(t=0) = n_0 \Theta(-x)$, Eq. (20) can be used to define the initial conditions for the electric field at the time $t=0$ at which the ion acceleration process begins. The following interpolation formulas for the electric field and ion velocity at the ion front:

$$E(t) \simeq \sqrt{\frac{2}{e}} \frac{E_0}{\sqrt{\tau^2 + 1}}, \quad (23)$$

$$u_f(t) \simeq 2c_s \ln(\tau + \sqrt{\tau^2 + 1}), \quad (24)$$

where $\tau = \omega_{pi}t/\sqrt{2e}$, give the correct behavior at $t=0$ for both the electric field [see Eq. (21)] and the front velocity, and reduce to previous expressions for $\omega_{pi}t \gg 1$. These formulas fit well numerical calculations by Mora (2003) using a Lagrangian fluid code. Related results of similar studies using fluid and kinetic descriptions can be found in the literature.¹²

The major drawback of Eq. (24) is that the maximum velocity of ions, and hence the cutoff energy, diverges logarithmically with time. This is not surprising, being an unavoidable consequence of the isothermal assumption and the chosen boundary conditions: the system has an infinite energy reservoir in the electron fluid and thus it is able to accelerate ions indefinitely. Nevertheless, the simplicity of Eq. (24) has proven to be attractive; thus it has been suggested to insert a phenomenological “maximum acceleration time” t_{acc} at which the acceleration should stop. Such a formula has been used in attempts to fit experimental data (Fuchs *et al.*, 2006b). We return to this point in Sec. III.D. There is no easier way to remove this unphysical behavior from the 1D planar model but to give a constraint of finite energy (per unit surface). In this way, the electron temperature decays in time due to the plasma expansion and to collisional and radiative losses. The electron cooling cooperates with the effects of finite acceleration length and maximum electron energy in the determination of a finite value for the maximum energy gain.

The expansion of plasma slabs (foils) of finite thickness, and hence of finite energy, has been considered analytically and numerically. In these models the electron temperature is taken as a function of time $T_h = T_h(t)$, determined either by the energy conservation equations (Betti *et al.*, 2005; Mora, 2005) or with *ad hoc* modeling of $T_h(t)$ (Bychenkov *et al.*, 2004).

Analytical solutions for the plasma expansion can be found in the quasineutral approximation, also for the kinetic Vlasov equation (18), using either the self-similar theory (Dorozhkina and Semenov, 1998) or a renormalized group theoretical approach (Kovalev, Bychenkov, and Tikhonchuk,

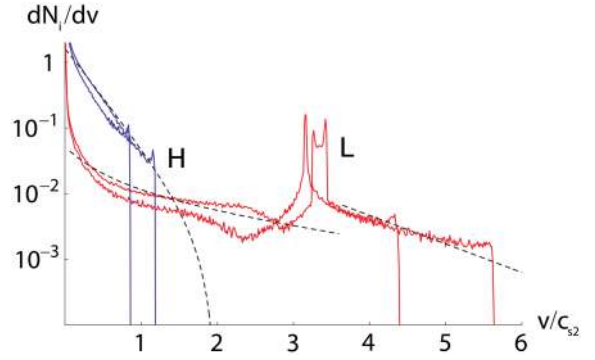


FIG. 17 (color online). Velocity spectrum of heavy ions (H) and light ions (L) at two different times from the numerical simulation of the expansion of a two-species plasma using a Boltzmann-Vlasov-Poisson model. Black dashed lines are analytical profiles based on self-similar solutions. The spectrum of light ions shows a peak typical of a multispecies expansion. From Tikhonchuk *et al.*, 2005.

2001, 2002). Two-temperature electron distributions have also been considered.¹³

3. Multispecies expansion

We now describe the expansion of a two species plasma, in which the dynamics of a heavy ion component (labeled with H in the following) is considered in addition to light ions (labeled with L). The most peculiar effect of the presence of two (or more) ion species, for appropriate parameters, is the appearance of spectral peaks, which are of interest as both a strong experimental signature and for application purposes.

The problem of two species expansion was studied by Gurevich, Pariiskaya, and Pitaevskii (1973), Bezzerides, Forslund, and Lindman (1978), and Srivastava, Sinha, and Lawande (1988). Here we mostly follow the more recent work of Tikhonchuk *et al.* (2005), where a simplified description is given based on the ordering assumptions

$$\alpha = \frac{A_H/Z_H}{A_L/Z_L} \gg 1, \quad N = \frac{Z_H n_H}{Z_L n_L} > \alpha. \quad (25)$$

These conditions state that the H species is quite heavier than the L one, that the concentration of the latter is small, and that the L ion plasma frequency is higher so that the dynamics of L ions is faster. These assumptions allow one to assume that, near the rarefaction front, the effect of L ions is unimportant and that the dynamics of the H ions can be described as a single species expansion as in Sec. III.C.2, where the relevant parameter is the H ion sound speed $c_H = \sqrt{Z_H T_h / A_H m_p} < c_L$, the L ions sound speed. L ions are treated as test particles in this region, where they are accelerated by the electric field $E \propto c_H^{-1}$ [see Eq. (13)], which is thus stronger than what would be created in the expansion of the L ions alone. The L ion velocity and density in this region can be obtained using the 1D fluid, self-similar equations with the above given

¹²See, e.g., Widner, Alexeff, and Jones (1971), Crow, Auer, and Allen (1975), Pearlman and Morse (1978), Denavit (1979), and Mora (2003) for the case of a single electron population and Bychenkov *et al.* (2004), Mora (2005), and Tikhonchuk *et al.* (2005) for the case of two electron components.

¹³See, e.g., Bezzerides, Forslund, and Lindman (1978), Wickens, Allen, and Rumsby (1978), Gurevich, Anderson, and Wilhelmsson (1979), True, Albritton, and Williams (1981), Kovalev, Bychenkov, and Tikhonchuk (2002), and Diaw and Mora (2011).

electric field (Tikhonchuk *et al.*, 2005), obtaining for the velocity profile $v_L \simeq c_L \sqrt{2(1 + x/c_H t)^{1/2}}$. Noticeably, the L ions velocity and density profiles vary slowly in space compared to the H ion ones, and the L ion flux is almost constant. Beyond the H ion front, only L ions are present and they can be described again by a single species expansion with $v_L \simeq c_L + x/t$ [see Eq. (22)]. However, matching of the velocity profiles in the region behind the H ion front implies the existence of a transition region where the velocity is approximately constant. This corresponds to a plateau region in the phase space and to a peak in the L ion energy spectrum. The heuristic reason for plateau formation is that the L ions are accelerated more efficiently behind the H ion front than ahead of it. Figure 17 shows the velocity spectrum from numerical results (Tikhonchuk *et al.*, 2005) using a Boltzmann-Vlasov-Poisson model (Bychenkov *et al.*, 2004) based on Eqs. (14), (15), and (18), compared with analytical estimates from the self-similar solution.

According to the above model the peak energy of L ions is

$$\mathcal{E}_L \simeq Z_L T_h \ln(4\sqrt{2}\alpha N/e). \quad (26)$$

As an important indication from this model, the mass ratio and the relative concentration of the two species might be engineered to optimize the L ion spectrum. Several simulation studies¹⁴ have been devoted to this issue and to the modeling of observations of multispecies spectra in both planar and spherical (droplet) targets (see Sec. III.E).

4. Numerical simulations

Even in their simplest formulation TNSA models are highly nonlinear and the set of available analytical solutions is limited. A numerical approach can be used to overcome these limitations and to address additional effects.

Referring to the 1D problem of plasma expansion, an hydrodynamic two-fluid approach may be used to take charge separation effects into account as reported by Mora (2003). The hydrodynamic model, however, cannot take into account kinetic effects such as non-Maxwell distribution and breakdown of equilibrium conditions. To address these effects a numerical solution of the Vlasov equation for the distribution function of electron and ions in phase space is needed. To this aim the PIC approach (see Sec. II.D) may be used, with the drawback of much larger computational requirements compared to hydrodynamics simulations. The reason is that, in order to obtain full numerical convergence and accurate, low-noise results, a very large number of particles should be used to resolve the strong density variations in the plasma expansion.

In its simplest formulation the 1D simulation of collisionless plasma expansion takes a single ion species into account and a limited set of parameters, such as the initial electron temperature and the initial thickness of the plasma; this is equivalent to fixing the total energy of the system. Such simplified simulations already reproduce qualitative features observed in the experiment and may match measured quantities such

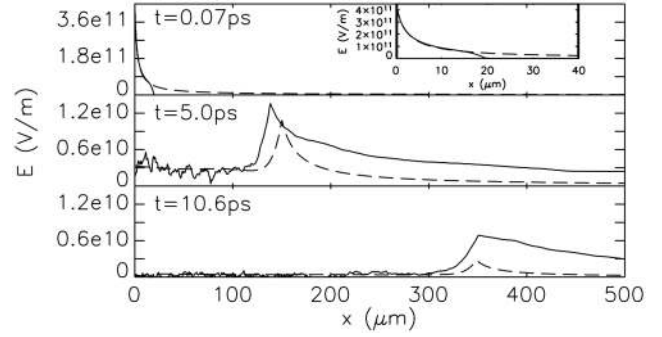


FIG. 18. Electric field profiles at different times from the numerical simulation of the collisionless expansion of a slab of warm plasma. Thick and dashed lines show results from a PIC code (Betti *et al.*, 2005) and a hydrodynamics code (Mora, 2003), respectively. Both simulations assume a 40 μm thick proton plasma slab with initial density $n_0 = 3 \times 10^{19} \text{ cm}^{-3}$ and electron temperature $T_{e0} = 500 \text{ keV}$. The inset shows the detail of the field distributions at early times, with the field in the PIC simulation extending over a finite distance. From Romagnani *et al.*, 2005.

as the ion front velocity, with a proper choice of initial parameters. As an example, Fig. 18 shows simulation results performed to support experimental observations by Romagnani *et al.* (2005), using both a hydrodynamics and a PIC code. The two approaches use different initial conditions, i.e., a Boltzmann equilibrium for fixed ions and a zero charge density distribution, respectively. The latter condition enables one to resolve in the PIC calculation the propagation of the electron front, resulting in the electric field vanishing at the front position and showing a strong temporal maximum at the earliest instants, in agreement with experimental observations.

The use of supercomputers allows one to perform multi-dimensional PIC simulations and to simulate the laser-plasma interaction and the generation of hot electrons, rather than imposing *a priori* their number and temperature. The computational challenges and limitations of such large-scale simulations have been discussed in Sec. II.D. In addition, most PIC simulations do not include collisions, which may play an important role in the transport of hot electrons through the target (see Sec. II.B.3). Nevertheless, PIC simulations have been vastly used as a valuable support in the interpretation of measurements of ion acceleration and were able to reproduce at least qualitatively several observed features of the TNSA picture; see, e.g., Pukhov (2001), Wilks *et al.* (2001), and Fuchs *et al.* (2005).

As an alternative to the PIC method, Gibbon *et al.* (2004) used a gridless, electrostatic “tree” particle code to simulate ion acceleration from wire targets. Such a code has the advantages of an unlimited spatial region for particles and of “automatic” inclusion of collisions at the cost of being purely electrostatic so that the laser-plasma interaction may be modeled only phenomenologically and magnetic field generation is not included.

D. Comparison between models and experiments

TNSA has been thoroughly investigated in a large number of experiments, performed, in the past decade, in many laser

¹⁴See, e.g., Kemp and Ruhl (2005), Brantov *et al.* (2006), Robinson, Bell, and Kingham (2006), Robinson and Gibbon (2007), Psikal *et al.* (2008), Robinson, Gibbon, Pfothner *et al.* (2009), and Brady and Arber (2011).

facilities all over the world. The maximum observed value of the ion energy \mathcal{E}_{\max} has probably been the most characterizing parameter of such experiments. Another important feature, mostly in light of potential applications, is the profile of the energy spectrum.

All this effort has resulted in an extensive collection of experimental data, against which the predictive capability of the TNSA theoretical models can be tested. Moreover, a new generation of laser facilities will soon be available, and it will then be possible to investigate a wider range of experimental parameters. Therefore the challenge of satisfactorily predicting the result of a TNSA experiment, providing sufficiently reliable scaling laws to extrapolate guidelines for the future experiments, is even more important.

Experimentally, great effort has been devoted to properly addressing the correlation among the above mentioned ion properties and the main laser and target parameters. Because of the importance of the laser irradiance in establishing the regime of interaction (see Sec. II), in the literature it has become common to report the maximum ion (mainly proton) energy \mathcal{E}_{\max} as a function of this parameter (see, e.g., Fig. 4). Collections of experimental data for \mathcal{E}_{\max} have been reported in several papers.¹⁵ On the other hand, it is apparent that the irradiance is not the only laser parameter playing a role in determining \mathcal{E}_{\max} . In particular, it has been established by many experiments that, at fixed irradiance, more energetic pulses lead to higher \mathcal{E}_{\max} . Moreover, already from the early experiments the strong influence of the laser prepulse level and duration and of the target properties on \mathcal{E}_{\max} has been evident. We devote Sec. III.E to a discussion of these topics, while here we point out the general difficulties which can be encountered when attempting to provide predictions of \mathcal{E}_{\max} for comparison with experimental data.

For all the models introduced in Sec. III.C, \mathcal{E}_{\max} can be evaluated once the required parameters of the physical system are known. This is a very delicate and often controversial issue because the input parameters are different in number, nature, and reliability. Some models use experimental laser and target parameters, which are known or controlled with well-defined precision, such as, e.g., mean irradiance, spot radius, energy and duration of the laser pulse, target thickness and chemical composition, or surface density of impurity protons in the target. Other models use, as input parameters, physical quantities determined by interaction and transport processes. We refer, in particular, to hot electron properties (see Sec. II.B.2) such as conversion efficiency η_h , temperature T_h , density n_h , cutoff energy, and beam divergence angle θ_{div} . These quantities may in principle be modeled and/or measured but most times are not precisely known. Finally, some models include purely phenomenological parameters such as the ion acceleration time t_{acc} (see Sec. III.C.2) and numerical parameters determined by fitting set of experimental data or numerical simulations. The experimental and theoretical uncertainties and the different nature of the model parameters inevitably impose some limitations to the conclusions that one could draw from a quantitative comparison.

We briefly touch on this problem following the work by [Perego et al. \(2011\)](#). The descriptions which have been selected in this paper are the fluid expansion models proposed by [Mora \(2003, 2005\)](#), the quasistatic approaches of [Schreiber et al. \(2006\)](#) and [Passoni and Lontano \(2008\)](#), and the “hybrid” descriptions by [Albright et al. \(2006\)](#) and [Robinson, Bell, and Kingham \(2006\)](#) (see Sec. III.C). The calculations used to implement these models and evaluate \mathcal{E}_{\max} are also summarized. To perform the comparison a database containing an extensive collection of published experimental parameters and results, referring to a wide range of laser and target parameters, has been considered. This analysis shows that, despite all the uncertainties, the predictions of the TNSA models can be considered quite good, and in some cases remarkable, for a wide range of experimental parameters. In particular, quasistatic models, especially the one proposed by [Passoni and Lontano \(2008\)](#), appear more suitable for the prediction of \mathcal{E}_{\max} . These conclusions are strongly affected by the estimates of the required parameters, and a more realistic approach to evaluate these quantities could improve the predicting capability of both expansion and hybrid models.

The possibility to compare model predictions with experimental parametric studies under well-defined and controlled laser conditions, aimed at providing reliable and clear scaling laws, can significantly enhance the effectiveness of the analysis. Figure 19 shows results from a parametric study of the dependence of \mathcal{E}_{\max} on laser power and duration ([Zeil et al., 2010](#)). Several other parametric investigations of the dependence of \mathcal{E}_{\max} on laser pulse irradiance, duration, energy, and fluence have been reported ([Fuchs et al., 2006b](#); [Nayuki et al., 2006](#); [Robson et al., 2007](#); [Flippo, Workman et al., 2008](#); [Flacco et al., 2010](#)) as well as attempts in interpreting part of these findings ([Passoni et al., 2009](#); [Passoni, Bertagna, and Zani, 2010a](#); [Zani, Sgattoni, and Passoni, 2011](#)).

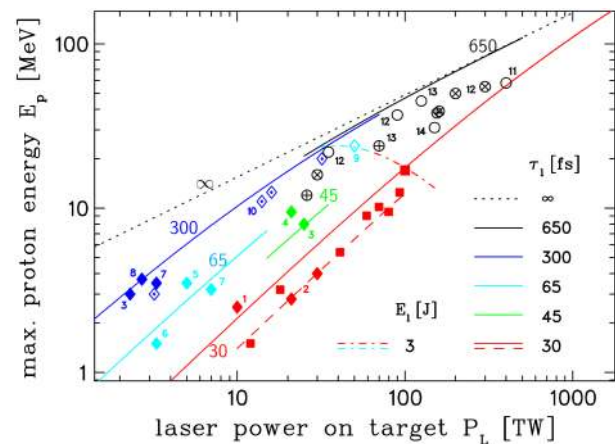


FIG. 19 (color online). Experimental scaling of proton energy cutoff with laser power and pulse duration. Squares are data from experiments performed with the DRACO laser at FZD (Dresden), showing a linear scaling with power in the short-pulse (30 fs) regime. Other points are data from other laboratories; see [Zeil et al. \(2010\)](#) for references and details. The fitting lines correspond to the static model by [Schreiber et al. \(2006\)](#) with different colors (labels) corresponding to different values of the pulse duration τ_1 as given in the legend. From [Zeil et al., 2010](#).

¹⁵See, e.g., [Krushelnick et al. \(2005\)](#), [Borghesi et al. \(2006, 2008\)](#), [Fuchs et al. \(2006b\)](#), [Robson et al. \(2007\)](#), and [Perego et al. \(2011\)](#).

E. Experimental optimization

After the first years of research, the combined vigorous development in both laser technology and advanced target manufacturing allowed the investigation of TNSA exploring a continuously increasing range of laser and target parameters. In most cases the two sets of parameters are intimately related. For example, the use of “extreme” geometrical target properties, such as thicknesses in the submicrometric range, requires the availability of extraordinarily clean, prepulse-free pulses to avoid early target evaporation and deformation. Such pulses can be obtained with recently developed techniques, such as plasma mirrors (Dromey *et al.*, 2004; Fuchs *et al.*, 2006a; Thaury *et al.*, 2007, and references therein), optical parametric amplification (Shah *et al.*, 2009), or crossed polarized wave (XPW) generation (Jullien *et al.*, 2005; Zaouter *et al.*, 2011, and references therein).

1. Energy cutoff enhancement

Mackinnon *et al.* (2002) studied the dependence of ion acceleration on the target thickness, with the aim of addressing the role played by the electron temporal dynamics and its effect on the formation of the accelerating sheath electric field. The experimental results showed an increase in the peak proton energy from 6.5 to 24 MeV when the thickness of the Al foil target was decreased from 100 to 3 μm . These data clearly indicate that an increase in the target thickness implies a lower mean density of the hot electrons at the surface and a consequent lowering of the peak proton energy.

The influence of the laser prepulse due to amplified spontaneous emission (ASE) on the acceleration of protons in thin-foil experiments has been investigated in detail by Kaluza *et al.* (2004). In this experiment Al foils of different thickness (from 0.75 to 86 μm) were used in the presence of an ASE prepulse whose duration could be controllably varied. The results indicated an optimal value for the target thickness, strongly depending on the prepulse duration, at which the TNSA process leads to the highest proton energies. For thinner targets, a prepulse-induced plasma formation at the rear side effectively suppressed TNSA, in agreement with the considerations developed in Secs. II.C and III.A. Related experimental work, where a wide range of laser parameters and different target materials have been considered, can be found in the literature (Spencer *et al.*, 2003; Fuchs *et al.*, 2006b).

Effective suppression of the laser prepulse level, that is, the adoption of ultrahigh laser contrast, can significantly alter the physical picture, since ultrathin targets, down to the nm level, can maintain their integrity until the interaction with the main pulse. With these conditions a more effective acceleration process can be expected because the refluxing and concentration of hot electrons in a smaller volume may lead to the establishment of a stronger electric field and, consequently, to higher ion energies. These ideas have been successfully tested by Neely *et al.* (2006), using Al target with thicknesses as low as 20 nm in combination with 33 fs pulses with ASE intensity contrast reaching 10^{10} . A significant increase of both maximum proton energy and laser-to-proton energy conversion efficiency was found at an optimum thickness of 100 nm.

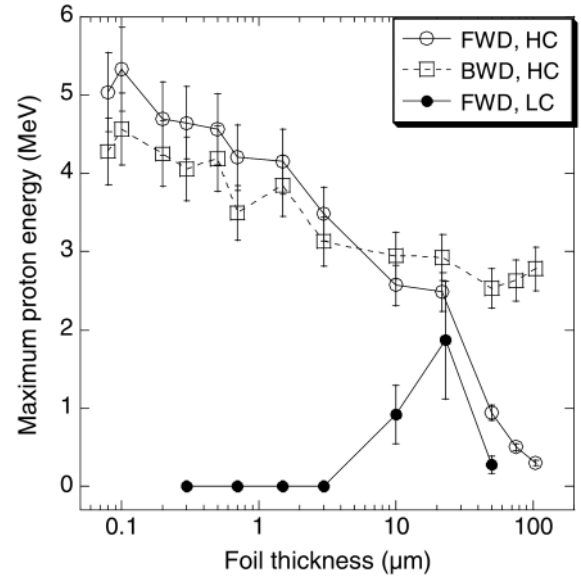


FIG. 20. Maximum detectable proton energy as a function of target thickness for high-contrast (HC) and low-contrast (LC) conditions. Data are shown for both backward (BWD) and forward (FWD) directed ions, respectively, showing the symmetrical behavior of TNSA for HC and ultrathin targets. The LC results show the existence of an “optimal” thickness determined by the laser prepulse causing early target disruption, similar to Kaluza *et al.* (2004). The laser pulse had 65 fs duration, $(0.5\text{--}1) \times 10^{19} \text{ W cm}^{-2}$ intensity, 45° incidence, and P polarization. From Ceccotti *et al.*, 2007.

Similar results have been obtained by Antici *et al.* (2007) and Ceccotti *et al.* (2007). As a further interesting feature of this latter experiment, a symmetrical TNSA on both front and rear sides has been demonstrated, as shown in Fig. 20, when a sufficiently high ($> 10^{10}$) laser contrast is used. This result confirms the universality of the TNSA process, which may also occur at the front side (accelerating ions in the backward direction) if the density profile is sharp enough. Recently, using a laser pulse with similar contrast, 40 fs duration, $10^{21} \text{ W cm}^{-2}$ and irradiating targets of 800 nm thickness, Ogura *et al.* (2012) reported proton energies up to 40 MeV, the highest value reported so far for pulse energies below 10 J.

Another possible strategy to exploit the effectiveness in the formation of the accelerating field in mass-limited targets is to reduce the lateral dimensions. Numerical investigations (Psikal *et al.*, 2008) have shown that a reduced surface leads to higher densities of hot electrons at the rear side of the target and, thus, to higher accelerating electric fields. Buffechoux *et al.* (2010) experimentally confirmed these findings showing that in targets having limited transverse extent, down to tens of μm , the laser-generated hot electrons moving with a component of the velocity along the lateral direction can be reflected from the target edges during time scales of the same order of the acceleration of the most energetic ions. This transverse refluxing can result in a hotter, denser, and more homogeneous electron sheath at the target-vacuum interface. A significant increase in the maximum proton energy (up to threefold), as well as increased laser-to-ion conversion efficiency, can be obtained with these conditions, as shown in Fig. 21. Similar results,

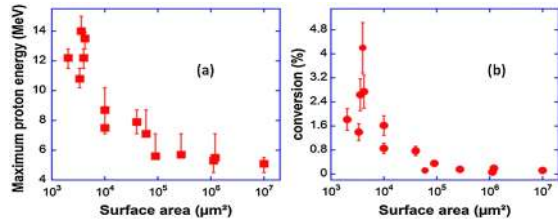


FIG. 21 (color online). Experimentally observed (a) cutoff proton energies and (b) conversion efficiency (for >1.5 MeV protons) for $2 \mu\text{m}$ thick Au targets as a function of surface area, evidencing the effect of electron refluxing. The laser pulse had 400 fs duration, $2 \times 10^{19} \text{ W cm}^{-2}$ intensity, 45° incidence, and P polarization. From Buffechoux *et al.*, 2010.

obtained with different laser and target parameters, have been found by Tresca *et al.* (2011), who also measured an increase in the maximum energy of protons accelerated from the edges of the target with decreasing target area.

Several other attempts have been made to increase the energy density of the hot electrons in the sheath and, consequently, the maximum proton energy. Following from the indications of Kaluza *et al.* (2004), McKenna *et al.* (2008) investigated whether there exists an optimum density profile at the front of the target which maximizes the laser absorption. The proton cutoff energy was increased by 25% with respect to a sharp interface case at “intermediate” plasma scale length (tens of μm). Under such conditions, the higher conversion efficiency into fast electrons was attributed to self-focusing of the driver pulse. Other studies of controlled prepulse effects on ion acceleration have been reported by Flacco *et al.* (2008) and Batani *et al.* (2010).

Recently, an energy cutoff increase up to 67.5 MeV, 35% higher than for comparator flat foil shots, was demonstrated by Gaillard *et al.* (2011) using specially devised targets, namely, flattop hollow microcones (Flippo *et al.*, 2008), which are a modification of conical targets used in fast ignition experiments (see Sec. V.C). The laser pulse is focused inside the target and starts interacting with the walls of the cone that it grazes while focusing down toward the flattop section. The reported result, obtained with 80 J of laser energy on the Trident laser at Los Alamos National Laboratory (LANL), is attributed to an efficient mechanism of electron acceleration taking place on the inner cone walls, named “direct laser-light-pressure acceleration.” The resulting increase in the number of high-energy electrons results in the increase of the maximum proton energy.

The use of targets with various structures has also been investigated with the particular aim to increase the ion energy already at relatively low laser intensities (below $10^{18} \text{ W cm}^{-2}$), using, e.g., double layer targets (Badziak *et al.*, 2001) and more recently nanowire-covered targets (Zigler *et al.*, 2011) for which surprisingly high energies up to 5.5–7.5 MeV for a $5 \times 10^{17} \text{ W cm}^{-2}$, 40 fs laser pulse were reported.

2. Source spectrum manipulation

Various approaches have been proposed in order to manipulate the spectrum of TNSA protons and ions, in most cases with the intent of obtaining narrow-band peaks, in other

cases with the aim to enhance proton numbers throughout the whole spectrum or in some spectral bands as required by specific applications. We first review a number of approaches in which the proton spectrum is modified at the source, leaving approaches which act on the proton beam after the initial acceleration to Sec. III.E.3.

Spectral peaks can appear as a consequence of multispecies plasma expansion (see Sec. III.C.3). This effect has been invoked to explain observations in proton beams from thin foils, where the peaks appear as modulation of a continuum exponential spectrum (Allen *et al.*, 2003) and in experiments employing droplets of heavy water, where peaks are observed in the deuterium spectrum (Ter-Avetisyan *et al.*, 2006). Spectral peaks have been observed in experiments employing high- Z metallic targets where a plastic layer [$0.5 \mu\text{m}$ polymethyl methacrylate (PMMA)] was coated as a dot on the rear surface of a $5 \mu\text{m}$ Ti foil (Schwoerer *et al.*, 2006; Pfothner *et al.*, 2008). These results, obtained on the 10 TW JETI laser in Jena, were explained on the basis of the proton depletion approach first suggested by Esirkepov *et al.* (2002). Robinson and Gibbon (2007) suggested instead that the proton density in the multispecies plastic layer is the important factor in determining the appearance of the spectral peak. Experimental implementation required the removal of the native contaminant layer present at the surface and resulted in peaks in the proton spectra at ~ 2 MeV, with $\sim 10\%$ spread and good reproducibility (Pfothner *et al.*, 2008).

Another experiment also relied on the (partial) removal of hydrogen contaminants from the surface of a palladium target (Heglich *et al.*, 2006) so that protons did not appear in the spectrum. Instead, monoenergetic features appeared

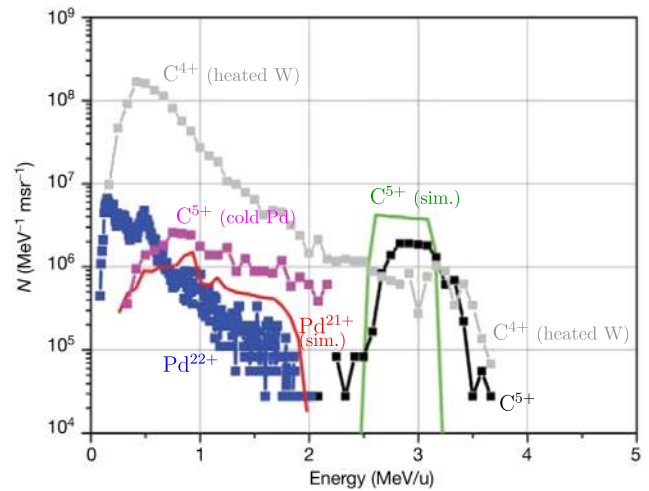


FIG. 22 (color online). Ion spectra from preheated Pd substrate targets from which hydrogen contaminants have been removed (Heglich *et al.*, 2006). Black curve: spectrum of C^{5+} ions. Blue curve: spectrum of the dominant substrate charge state Pd^{22+} . Green and red curves: simulated C^{5+} and Pd^{21+} spectra. Gray curve: spectrum of dominant C^{4+} ions from a heated W target. Magenta curve: C^{5+} signal from a cold Pd target. In the cases of black and blue curves, an ultrathin layer of graphite is present on the target surface, and a quasimonoenergetic spectrum appears. In the last two cases (gray and magenta curves) the targets have a thick layer of carbon contaminants and do not form a monolayer source, resulting in exponential-like spectra. From Heglich *et al.*, 2006.

in the C spectrum (specifically C^{5+}), suggesting that an ultrathin layer of graphite is formed as a result of phase changes of the carbon compounds in the contaminant and that all C^{5+} ions from the layer experience approximately the same accelerating field as theoretically predicted (Esirkepov *et al.*, 2002; Albright *et al.*, 2006). Figure 22 shows spectra for targets with and without contaminant removal, together with hybrid simulation predictions.

3. Staged acceleration and beam control

Staged acceleration employing two laser pulses on two separate targets has also been investigated as a possible route to spectral manipulation of laser-driven ion beams. This idea relies on accelerating a TNSA beam from a first target and direct it through a second foil, which is irradiated by a second laser pulse at the time that a particular group of TNSA protons crosses the foil. These protons should thus experience an accelerating field as they transit through the rear surface of the second foil and gain additional energy. An experiment by Pfothner *et al.* (2010), also carried out on the JETI laser, tested this idea. Peaks and dips in the spectrum were observed at energies of ~ 1 MeV which correlated well with the time of flight of protons reaching the second target as it is irradiated, showing that the field on the second target slightly boosts protons in a given energy range resulting in the spectral modification. Burza *et al.* (2011) reported a two-stage approach employing spherical shell targets, irradiated by a single laser pulse, in which protons accelerated by TNSA at the front of the shell experience a second accelerating field while they transit through the opposite side of the shell, which modifies the high-energy end of the spectrum. The field is due to a hot electron charge wave spreading along the target surface from the interaction point, as reported in several experiments (Toncian *et al.*, 2006; McKenna *et al.*, 2007; Quinn *et al.*, 2009a).

A different type of two-stage approach was tested by Markey *et al.* (2010) on the VULCAN laser. Two pulses of sub-ps duration were sequentially focused, with controllable delay, on the same target in order to modify the temporal history of the hot electron source driving the TNSA, as suggested originally by Robinson *et al.* (2007). An optimal delay was seen to result in an increase of energy and conversion efficiency and, additionally, a modification of the slope of the spectral profile. In this case, besides an optimization of hot

electron production by the main pulse in a front surface plasma gradient, similar to Kaluza *et al.* (2004) and McKenna *et al.* (2008), they suggest that an additional modification of the proton spectrum arises from the fact that proton acceleration by the main pulse takes place in an already expanding multi-species, plasma sheath at the target rear surface. Under these conditions, the electrostatic field peaks at the front separating protons from heavier species, and reaccelerates mainly the lower energy part of the spectrum. Similarly, in a recent experiment, Dollar *et al.* (2011) obtained spectral modifications, resulting in the appearance of narrow-band spectral peaks at ~ 2 –3 MeV energies, by focusing a prepulse (10^{-5} of the 10^{21} W cm $^{-2}$ peak intensity) on ultrathin foils a few tens of ps before the peak of the main pulse.

A staged technique which acts on the protons after the acceleration, but employing all-optical means, was demonstrated by Toncian *et al.* (2006, 2011). A transient electric field is excited at the inner surface of a metal cylinder (having \sim mm diameter and length) irradiated on the outer surface by a high-intensity laser pulse while a laser-driven proton beam transits through it; see Figs. 23(a)–23(c). The field acts on the protons by modifying their divergence leading to a narrow, collimated beamlet. As the field is transient, typically lasting for ~ 10 ps, it affects only the proton component transiting through the cylinder within this time window, i.e., within a narrow energy band, leading to a spike in the energy spectrum, as visible in Fig. 23(f), showing a 0.2 MeV band at ~ 6 MeV. Further experiments have shown that the position of the spectral peak can be controlled by varying the delay between the two laser pulses (Toncian *et al.*, 2011) and confirmed that the focusing is chromatic, i.e., the focal position varies with proton energy.

A similar approach, but employing a single pulse, was developed by Kar *et al.* (2008b) for reducing the proton beam divergence. Also conceptually similar to the approach described above by Burza *et al.* (2011), the scheme employs specially designed targets in which a thin foil is inserted in a thicker frame, so that the charge wave expanding outward from the acceleration region at the rear of the foil generates on the frames surface an electric field transverse to the expanding beam, which partially constrains its natural divergence.

Other proposed methods of optical control of proton beam properties include beam steering triggered by shock waves

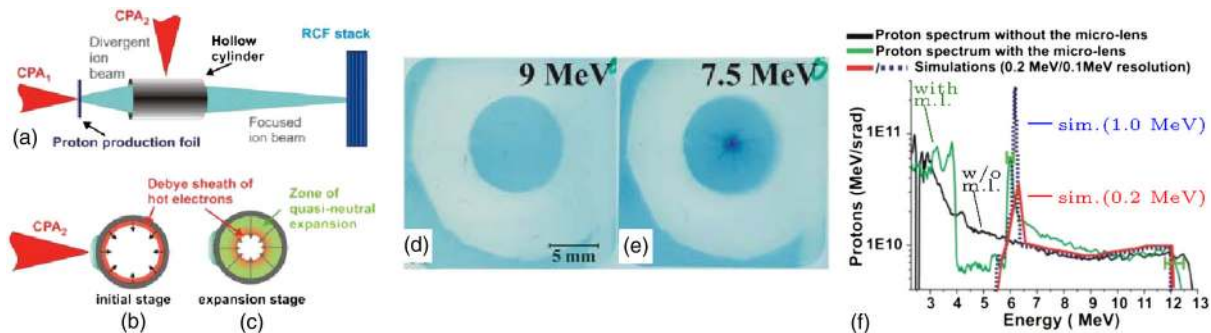


FIG. 23 (color online). (a)–(c) Schematic of laser-driven electrostatic lens. (d), (e) RCF stack beam profiles for protons of 9 and 7.5 MeV, respectively, showing that the 7.5 MeV protons are focused by the fields inside the cylinder and form a black spot on the RCF. (f): Proton spectra. Green line: spectrum obtained under same triggering conditions as in (e). Black line: typical exponential spectrum obtained when cylinder is not triggered. From Toncian *et al.*, 2006.

locally deforming the target surface (Lindau *et al.*, 2005; Lundh *et al.*, 2007), an effect also reported by Zeil *et al.* (2010), and control of the beam homogeneity and cross section profile by focusing an annular beam around the high-intensity interaction region, which modifies the properties of hot electrons refluxing through the target (Carroll *et al.*, 2007).

The high degree of beam laminarity, and the fact that ion emission is substantially normal to the target surface, led early on to the suggestion that by appropriately shaping the surface it should be possible to ballistically focus down the protons to a tight spot (Ruhl *et al.*, 2001; Wilks *et al.*, 2001), ideally recovering the properties of the virtual source. The idea is consistent with (and complementary to) observations of TNSA ions from wire targets, where the curvature of the target leads to a highly diverging beam ion with the form of an expanding disk (Beg *et al.*, 2004). An indirect experimental demonstration of focusing was obtained via enhanced, localized heating of a secondary target, as discussed in Sec. V.B (Patel *et al.*, 2003; Snavely *et al.*, 2007). Recently, a more direct demonstration of proton beam focusing was obtained by mesh projection methods in experiments where, employing targets with hemicylindrical (Kar *et al.*, 2011) or hemispherical shape (Bartal *et al.*, 2012), beam focusing (down to 20–25 μm spots) over the whole spectrum (up to 25 MeV) was demonstrated. The data highlighted the achromatic nature of the focusing at the different energies, consistent with the energy dependent variations in divergence from a planar foil.

Several groups implemented conventional accelerator techniques for energy selection or transport of laser-accelerated protons, in view of possible downstream applications of the proton beam (see Sec. V). Besides simple energy selection with bending magnets, the range of options explored includes the use of pairs of quadrupole magnets for refocusing protons at distances in the 5–60 cm range and in $\sim 100 \mu\text{m}$ spots (Schollmeier *et al.*, 2008; Nishiuchi *et al.*, 2009) or to collimate (Ter-Avetisyan *et al.*, 2008) protons within a given spectral band up to 14 MeV as found by Schollmeier *et al.* (2008). A crucial parameter in this approach is the acceptance angle of the quadrupole system, which may limit the number of particles that can be focused. Large acceptance pulsed solenoids (~ 9 T) were also used (Roth *et al.*, 2009; Harres *et al.*, 2010) for collimation and transport of a large number of $\sim 10^{12}$ particles.

The use of synchronous rf fields for phase rotation resulted in the appearance of multiple peaks across a broadband spectrum (Ikegami *et al.*, 2009). Although demonstrated only at relatively low energy and over low-energy bands, this technique is in principle interesting as, rather than “slicing” a portion of the spectrum, which is effectively what is done in several of the methods above, it can concentrate in a narrow spectral band protons originally contained within a larger spectral region. The phase rotation can be accompanied under the right conditions by a collimation effect.

Some of these techniques have already been implemented sequentially in test beam lines operating at 1 Hz repetition (Nishiuchi *et al.*, 2010a) with a view to future biomedical applications (see Sec. V.D).

IV. OTHER ACCELERATION MECHANISMS

A. Radiation pressure acceleration

EM waves carry momentum, which may be delivered to a nontransparent (either absorbing or reflecting) medium. This is the origin of radiation pressure¹⁶ whose expression for a plane, monochromatic EM wave of intensity I and frequency ω normally incident on the plane surface of a medium at rest, is given by

$$P_{\text{rad}} = (1 + R - T) \frac{I}{c} = (2R + A) \frac{I}{c}, \quad (27)$$

where R , T , and A are the reflection, transmission, and absorption coefficients (with $R + T + A = 1$) defined as a function of the refractive index and thus of the wave frequency, e.g., as done in the derivation of Fresnel formulas (Jackson, 1998). Radiation pressure is related to the total steady PF on the medium (see Secs. II.A and II.B.1). Being proportional to the inverse of the particle mass, the PF effectively acts on the electrons. At the surface of an overdense plasma the electrons are pushed inward by the PF, leaving a charge separation layer and creating an electrostatic, backholding field that in turn acts on the ions and leads to their acceleration.

In the case of normal incidence of a plane wave on a flat surface the PF density is the cycle-averaged value of the $\mathbf{J} \times \mathbf{B}$ force. In the following discussion of RPA we refer to such a case unless otherwise stated and consider only the steady action of radiation pressure. As discussed in Sec. II.B.1, the oscillating component of the $\mathbf{J} \times \mathbf{B}$ force drives a sweeping oscillation at 2ω of the density profile and causes strong absorption and hot electron generation, except in the case of circular polarization for which the oscillating component vanishes. In the latter case, on the time scale of ion motion it may be assumed that the electrons are mostly in a mechanical equilibrium so that the PF and electrostatic force locally balance each other.

1. Thick targets: Hole boring regime

The intense radiation pressure of the laser pulse pushes the surface of an overdense plasma inward, steepening the density profile. For a realistic laser beam of finite width, the radiation pressure action drives a parabolic deformation of the plasma surface allowing the laser pulse to penetrate deeply into the target; this process is commonly named hole boring, even when referring to a planar geometry, and it is associated with ion acceleration at the front side of the target. Note that in the literature different definitions, such as “sweeping acceleration” (Sentoku *et al.*, 2003) or “laser piston” (Schlegel *et al.*, 2009), are also used to refer to essentially the same process.

The recession velocity of the plasma surface, also named the HB velocity v_{HB} , may be simply estimated by balancing the EM and mass momentum flows in a planar geometry (Denavit, 1992; Wilks *et al.*, 1992; Robinson, Gibbon, Zepf *et al.*, 2009;

¹⁶The electromagnetic theory of radiation pressure is due to James Clerk Maxwell (1873). It is, however, interesting that the Italian physicist Adolfo Bartoli (1884) also independently obtained Maxwell’s result in 1875 from thermodynamic considerations.

Schlegel *et al.*, 2009). In the instantaneous frame where the surface is at rest we observe incoming ions with density $n_i \gamma_{\text{HB}}$ and velocity $-v_{\text{HB}}$ bouncing back at the surface. The EM momentum flow, i.e., the radiation pressure, must then balance a momentum flow difference equal to $n_i \gamma_{\text{HB}} (2m_i \gamma_{\text{HB}} v_{\text{HB}}) v_{\text{HB}}$ with $\gamma_{\text{HB}} = (1 - v_{\text{HB}}^2/c^2)^{-1/2}$. In this reference frame, the radiation pressure is $P_{\text{rad}} = (2I/c)(1 - v_{\text{HB}}/c)/(1 + v_{\text{HB}}/c)$ as demonstrated by a Lorentz transformation.¹⁷ The global momentum balance thus gives¹⁸

$$\frac{2I}{c} \frac{1 - v_{\text{HB}}/c}{1 + v_{\text{HB}}/c} = n_i \gamma_{\text{HB}} (2m_i \gamma_{\text{HB}} v_{\text{HB}}) v_{\text{HB}}. \quad (28)$$

Solving for v_{HB} yields

$$\frac{v_{\text{HB}}}{c} = \frac{\Pi^{1/2}}{1 + \Pi^{1/2}}, \quad \Pi = \frac{I}{m_i n_i c^3} = \frac{Z n_c m_e}{A n_e m_p} a_0^2. \quad (29)$$

The fastest ions are those bouncing back from the surface in the moving frame, resulting in a maximum energy per nucleon in the laboratory frame

$$\mathcal{E}_{\text{max}} = 2m_p c^2 \frac{\Pi}{1 + 2\Pi^{1/2}}. \quad (30)$$

In the nonrelativistic regime where $\Pi \ll 1$ and $v_{\text{HB}} \ll c$, we obtain $v_{\text{HB}}/c \approx \Pi^{1/2}$ and $\mathcal{E}_{\text{max}} \approx 2m_p c^2 \Pi$.

Essentially the same results are obtained with a dynamical model of ion acceleration in the charge separation region at the surface (Macchi *et al.*, 2005). Such model and related PIC simulations show that the ions pile up at the end of the skin layer producing a sharp density spike and causing hydrodynamical breaking and collapse of the electron equilibrium. This process leads to the production of a narrow bunch of fast ions at the velocity $2v_{\text{HB}}$ which penetrates into the plasma bulk. Eventually the quasiequilibrium condition is established again and the process repeats itself as long as the laser pulse is on. HB acceleration is thus of pulsed nature, although on the average it may be described by a steady model (Schlegel *et al.*, 2009).¹⁹

Equation (30) indicates that with present-day intensities high energies may be obtained via HB acceleration if the density can be reduced to be slightly above n_c , which is possible if a gas jet target and a long wavelength laser, i.e., CO₂, is used. This scheme would be interesting for

¹⁷Note that the relativistic correction is equivalent to account for the energy depletion of the incident radiation in the adiabatic approximation. This can easily be shown by the heuristic model of radiation pressure as resulting from the reflection of a number N (per unit surface) of photons with energy momentum $(\hbar\omega, \hbar\omega/c)$ contained in a short bunch of duration τ , corresponding to an intensity $I = N\hbar\omega/\tau$. If the surface is moving at velocity $V = \beta c$, the frequency of the reflected photons is $\omega_r = \omega(1 - \beta)/(1 + \beta)$ and the reflection time is $\tau_r = \tau/(1 - \beta)$. The resulting pressure is $P = |\Delta p|/\Delta t = (N\hbar/c)(\omega + \omega_r)/\tau_r = (2I/c)(1 - \beta)/(1 + \beta)$.

¹⁸For simplicity we assume I to be independent of time. Generalization to a time-dependent profile $I(t)$ is discussed by Robinson, Gibbon, Zepf *et al.* (2009).

¹⁹For theoretical or simulation studies of HB by circularly polarized laser pulses, see also Liseikina and Macchi (2007), M. Chen *et al.* (2008), Liseykina *et al.* (2008), Yin *et al.* (2008), and Naumova *et al.* (2009) for a single ion species case, and Robinson, Kwon, and Lancaster (2009) and Zhang *et al.* (2009) for two ion species plasmas.

applications since it allows control of the background density, the use of a pure proton target, and high-repetition rate since the gas is flowing. In a recent experiment (Palmer *et al.*, 2011) employing 10 μm wavelength, $\sim 6 \times 10^{15} \text{ W cm}^{-2}$ circularly polarized pulses ($a_0 \approx 0.5$), and a hydrogen gas jet with density of a few times n_c , protons of energy up to 1.2 MeV and a narrow energy spread were observed (see Fig. 24). The observed ion energies were fairly consistent with a linear scaling with I/n_e as predicted by the HB model. The energies were actually higher than expected considering the vacuum laser intensity, suggesting that self-focusing in the underdense region could have increased the intensity in the plasma.

We note that Palmer *et al.* (2011) reported on protons accelerated by a shock driven by radiation pressure, similarly to several who refer to HB or piston acceleration in thick targets as acceleration in the electrostatic shock sustained by the laser pressure at the front surface (Zhang, Shen, Yu *et al.*, 2007; Schlegel *et al.*, 2009; Zhang *et al.*, 2009). In the context of ion acceleration by a laser, we prefer to reserve the term “shock” for the regime described in Sec. IV.B which implies the generation of a true electrostatic shock wave, able to propagate into the plasma bulk and drive ion acceleration there. From the point of view of fluid theory, a shock wave launched with velocity v_{sho} requires the sound speed, and thus the electron temperature, to be large enough to prevent the Mach number $M = v_{\text{sho}}/c_s$ from exceeding the critical value $M_{\text{cr}} \approx 6.5$ above which one does not have a shock but a “pure piston” (Forslund and Freidberg, 1971). Thus, formation of a true, high speed shock wave may be inhibited for circular polarization because of the reduced electron heating.

Experimental evidence of HB acceleration in solid targets is less clear at present. Badziak *et al.* (2004) reported a series of observations of high-density, $\sim \text{keV}$ energy ion pulses (plasma “blocks”) for subrelativistic irradiation ($< 10^{18} \text{ W cm}^{-2}$) of solid targets (but in the presence of significant preplasma). These results were interpreted using a model of ponderomotive skin-layer acceleration at the critical surface, a concept that sounds rather similar to HB-RPA. Akli *et al.* (2008) reported on heating of solid-density matter due to laser-driven density profile sweeping

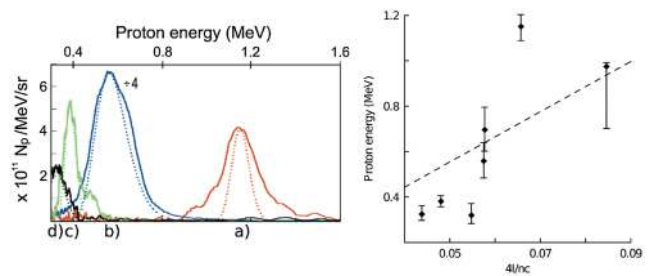


FIG. 24 (color online). Hole boring acceleration by a CO₂ laser pulse in a gas jet. The left frame shows ion spectra for various values of the intensity I_{15} (in units of $10^{15} \text{ W cm}^{-2}$) and the electron density $n = n_e/n_c$: (a) $I_{15} = 6.4$, $n = 6.1$; (b) $I_{15} = 5.5$, $n = 6.1$; (c) $I_{15} = 5.9$, $n = 7.6$; (d) $I_{15} = 5.7$, $n = 8.0$. The right frame shows the observed scaling of ion energies with the ratio $4I_{15}/(nc)$. From Palmer *et al.*, 2011.

and shock formation at intensities up to $5 \times 10^{20} \text{ W cm}^{-2}$, and Henig *et al.* (2009a) reported on ion acceleration by a converging shock in spherical targets irradiated at $1 \times 10^{20} \text{ W cm}^{-2}$. For both these experiments, the analysis of data and supporting PIC seems also compatible with HB-RPA occurring at the front surface, although the electron heating due to the use of linear polarization complicates the picture. Indications of strong radiation pressure effects were also obtained from the modeling of collimated, high-density plasma jets at the rear side of targets with a few micron thickness, at intensities up to $2 \times 10^{20} \text{ W cm}^{-2}$ (Kar *et al.*, 2008a). It should be noted that, although the scaling of Eq. (30) leads to relatively modest energies in solid-density targets, the foreseeable values are of interest for applications requiring large numbers of ions at energies of only a few MeV (see Sec. V).

2. Thin targets: Light sail regime

As discussed above, hole boring RPA applies to a “thick” target, i.e., much thicker than the skin layer in which ion acceleration by the space-charge field occurs. The laser pulse penetrates into the target by pushing adjacent surface layers via a repeated cycle of ion bunch acceleration. The situation changes when a target is thin enough that all the ions are accelerated before the end of the laser pulse, i.e., a complete hole boring occurs. In such a case, the laser pulse is able to further accelerate ions to higher energies since the ions are not screened by a background plasma anymore.

The thin target regime of RPA has been named light sail as the term is appropriate to refer to a *thin* object of finite inertia, having large surface and low mass, so that it can receive a significant boost from radiation pressure. The invention of the laser soon stimulated possible applications of the LS concept, including visionary ones such as laser-driven spacecraft propulsion (Forward, 1984). To support this idea Marx (1966) used calculations based on the simple model of a flat, perfect mirror boosted by a plane wave. The analytical solution and scaling laws provided by such basic model (Simmons and McInnes, 1993) are useful to illustrate the most appealing features of LS-RPA, such as high conversion efficiency in the relativistic limit and the possibility to reach very high energies with foreseeable laser and target technology.

The equation of motion for a moving target (sail) in the laboratory frame can be obtained with the help of a Lorentz transformation, similarly to Eq. (28). Neglecting absorption for simplicity ($A = 0$) we obtain

$$\frac{d}{dt}(\beta\gamma) = \frac{2I(t_{\text{ret}})}{\sigma c^2} R(\omega') \frac{1 - \beta}{1 + \beta}, \quad \frac{dX}{dt} = \beta c, \quad (31)$$

where X is the position of the sail, $\beta = V/c$ is its velocity in units of c , $\gamma = (1 - \beta^2)^{-1/2}$, $\sigma = m_i n_i \ell$ is the mass density per unit surface, and $\omega' = \omega[(1 - \beta)/(1 + \beta)]^{1/2}$ is the EM wave (laser) frequency in the rest (sail) frame. Note that the intensity I is in general a function of the retarded time $t_{\text{ret}} = t - X/c$.

Analytical solutions to Eqs. (31) exist depending on suitable expressions for $R(\omega)$, the simplest case being

that of a perfectly reflecting mirror ($R = 1$) and a pulse of constant intensity I (Simmons and McInnes, 1993).²⁰ The γ factor as a function of time is given by

$$\gamma(t) = \sinh(u) + \frac{1}{4\sinh(u)}, \quad u \equiv \frac{1}{3} \text{asinh}(3\Omega t + 2), \quad (32)$$

where $\Omega \equiv (Zm_e a_0^2 / Am_p \zeta) \omega$ and ζ has been defined in Eq. (5). Asymptotically, $\gamma(t) \simeq (3\Omega t)^{1/3}$ [see Fig. 25(a)].

The most significant quantities can be obtained for an arbitrary pulse shape $I(t)$ as a function of the dimensionless pulse fluence \mathcal{F} (the pulse energy per unit surface):

$$\mathcal{F}(t_{\text{ret}}) = \frac{2}{\sigma c^2} \int_0^{t_{\text{ret}}} I(t') dt'. \quad (33)$$

The sail velocity β , the corresponding energy per nucleon $\mathcal{E} = m_p c^2 (\gamma - 1)$, and the instantaneous efficiency η (i.e., the ratio between the mechanical energy delivered to the sail and the incident pulse energy)²¹ are given by

$$\beta(t_{\text{ret}}) = \frac{[1 + \mathcal{F}(t_{\text{ret}})]^2 - 1}{[1 + \mathcal{F}(t_{\text{ret}})]^2 + 1}, \quad (34)$$

$$\mathcal{E}(t_{\text{ret}}) = m_p c^2 \frac{\mathcal{F}^2(t_{\text{ret}})}{2[\mathcal{F}(t_{\text{ret}}) + 1]}, \quad (35)$$

$$\eta(t_{\text{ret}}) = \frac{2\beta(t_{\text{ret}})}{1 + \beta(t_{\text{ret}})} = 1 - \frac{1}{[\mathcal{F}(t_{\text{ret}}) + 1]^2}. \quad (36)$$

Thus, $\eta \rightarrow 1$ when $\beta(t_{\text{ret}}) \rightarrow 1$. The final energy per nucleon \mathcal{E}_{max} is obtained from the total fluence $\mathcal{F}_{\infty} = \mathcal{F}(t_{\text{ret}} = \infty)$. For a constant intensity $\mathcal{F}_{\infty} = \Omega \tau_p$, where τ_p is the duration of the laser pulse. In practical units $\mathcal{F}_{\infty} = 2.2 F_{1e8} \rho_1^{-1} \ell_{10}^{-1}$, where F_{1e8} is the fluence in units of 10^8 J cm^{-2} , $\rho_1 = m_i n_i / 1 \text{ g cm}^{-3}$, and $\ell_{10} = \ell / 10 \text{ nm}$. The scalings for \mathcal{E}_{max} are summarized in Fig. 25(b). With present-day or near-term laser technology, fluence values of 10^8 J cm^{-2} seem affordable, while target manufacturing can produce films of a few nm thickness, e.g., diamondlike carbon (DLC) foils. These values yield $\mathcal{F}_{\infty} > 1$ allowing one to approach a regime of high efficiency, relativistic ions, and favorable scaling with the pulse energy.

The above estimates have been obtained assuming a perfectly reflecting sail ($R = 1$) that, for a given surface density parameter ζ , limits the laser amplitude to $a_0 < \zeta$ due to the onset of relativistic transparency [Eq. (5)] that reduces the boost on the foil. This effect suggests $a_0 = \zeta$ as an “optimal” condition for LS acceleration (Macchi, Veghini, and Pegoraro, 2009; Tripathi *et al.*, 2009)²² which might be,

²⁰For a constant intensity I , Eqs. (31) are identical to those for a charge accelerating during Thomson scattering from a plane wave; see Landau and Lifshitz (1962) who leave the solution as an exercise for the reader.

²¹The expression for η also follows from “photon number” conservation and frequency downshift (see Sec. IV.A.1). In the reflection of N photons from the mirror, the energy transferred to the mirror is $N\hbar(\omega - \omega_r) = [2\beta/(1 + \beta)]N\hbar\omega \equiv \eta(N\hbar\omega)$.

²²Some give a similar condition for the optimal thickness but with slightly different numerical factors (Yan *et al.*, 2008, 2009a; Ji *et al.*, 2009).

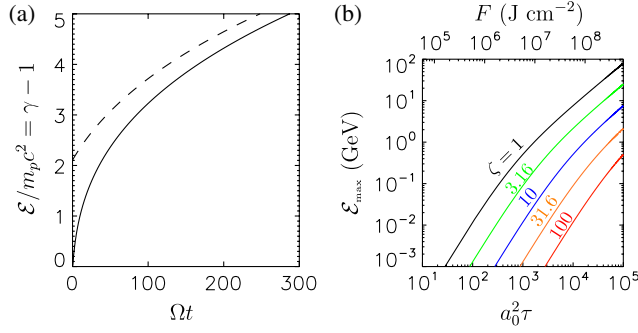


FIG. 25 (color online). (a) Energy per nucleon vs time from the analytical solution [Eq. (32)] of the LS model with $R = 1$. The dashed line gives the asymptotic $\sim t^{1/3}$ behavior. (b) Scaling of the energy per nucleon as a function of the dimensionless pulse fluence $a_0^2 \tau$ (where τ is the pulse duration in units of the laser period) and of the surface density ζ [Eq. (5)] for $\zeta = 1$ (black line), 3.16 (green line), 10 (blue line), 31.6 (orange line) and 100 (red line). The values on the upper horizontal axis give the fluence in J cm^{-2} corresponding to $a_0^2 \tau$ for $\lambda = 0.8 \mu\text{m}$.

however, relaxed by the effect of frequency decrease in the moving foil frame, increasing $R(\omega')$ [see Eq. (31)]. For $a_0 > \zeta$, all electrons are pushed away from the foil. In this regime the ions in the foil undergo a Coulomb explosion producing a broad ion spectrum. In a composite target the ion field after electron expulsion might be used for monoenergetic acceleration of a proton layer (Bulanov *et al.*, 2008; Grech *et al.*, 2009).

The interest in the LS regime was greatly stimulated by three-dimensional PIC simulations of thin-foil acceleration by Esirkepov *et al.* (2004) which showed that the temporal dependence and typical values of the ion energy were well described by the LS model. The simulations assumed a laser pulse with peak amplitude $a_0 = 316$ ($I\lambda^2 = 1.4 \times 10^{23} \text{ W cm}^{-2}$) and 8 cycles duration, and a proton slab of density $49n_c$ and 1λ thickness. Most of the ions in a thin-foil target are accelerated coherently up to relativistic energies ($\sim 1.5 \text{ GeV}$) as shown in Fig. 26. According to Esirkepov *et al.* (2004), in order for RPA to become the dominant acceleration mechanism the ions have to acquire relativistic energies already within one laser cycle, so that they can promptly follow electrons which are displaced in the longitudinal direction by the ponderomotive force. Later theoretical studies of such a so-called radiation pressure dominant (RPD) regime include Rayleigh-Taylor-like instability of the foil (Pegoraro and Bulanov, 2007) and the effects of radiation friction which play a significant role at ultrarelativistic intensities (Tamburini *et al.*, 2010). Of particular interest is the possibility of a self-regulated regime where the transverse expansion of the foil decreases the density along the axis [while the frequency downshift in the foil frame compensates the effect of decreasing ζ on $R(\omega')$], allowing for an increase of the ion energy at the expense of the total number of accelerated ions (Bulanov *et al.*, 2010a, 2010b). For a 3D expansion, theory predicts an asymptotic scaling with time of kinetic energy $K(t)/mc^2 \approx (3\Omega t)^{3/5}$ that is more favorable than for plane acceleration. This effect has recently been confirmed by 3D simulations (Tamburini *et al.*, 2012) showing a *higher* peak energy than found in lower dimensionality simulations.

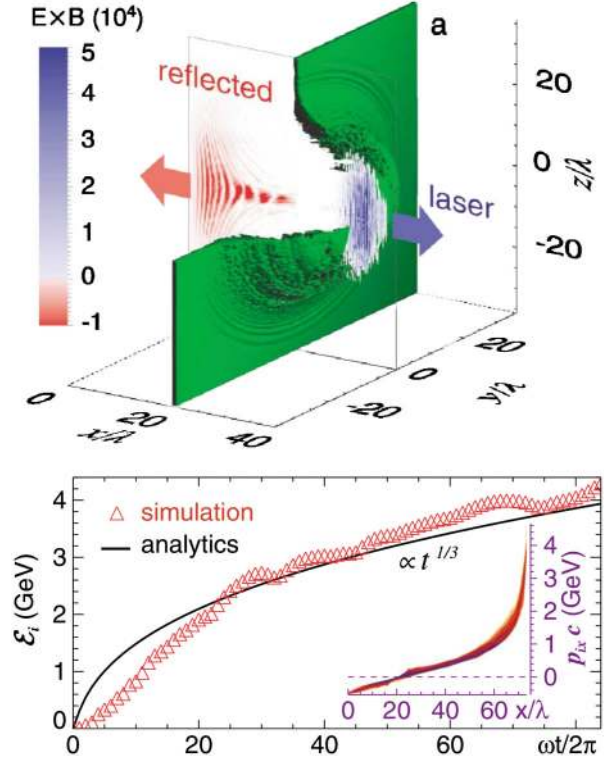


FIG. 26 (color online). Three-dimensional simulations of thin-foil acceleration in the radiation pressure dominant regime (see text for parameters). Top: Snapshots at $t = 40 \text{ T}$ of ion density isosurface and Poynting vector in the $y = 0$ plane. Bottom: The maximum ion kinetic energy vs time and the ion phase-space projection (x, p_x) at $t = 80 \text{ T}$. The solid line corresponds to the analytical calculation according to the LS model. From Esirkepov *et al.*, 2004.

The ultrahigh intensities needed for RPD acceleration are still above present-day laser technology. However, after the proposal of Esirkepov *et al.* (2004) it was realized that exploring the concept using pulses with circular polarization (CP) at normal laser incidence would enable an investigation of a RPD regime at lower intensities as theoretically discussed by Macchi *et al.* (2005) in thick targets. Three papers (Zhang, Shen, Li *et al.*, 2007; Klimo *et al.*, 2008; Robinson *et al.*, 2008) independently showed that the use of CP allowed an optimal coupling with an ultrathin foil target as well as rather monoenergetic spectra. Much theoretical work has been devoted to LS-RPA with CP pulses, unfolding a dynamics that is much richer than what is included in the simple “accelerating mirror” model. In particular, formation of a monoenergetic ion distribution is not straightforward (Eliasson *et al.*, 2009; Macchi, Veghini, and Pegoraro, 2009; Macchi *et al.*, 2010) and may require one to control and engineer both the pulse and target properties (Qiao *et al.*, 2009, 2010; T.-P. Yu *et al.*, 2010; Grech *et al.*, 2011).

Several multidimensional simulation studies suggested using flattop transverse profiles to keep a quasi-1D geometry (Klimo *et al.*, 2008; Liseykina *et al.*, 2008; Robinson *et al.*, 2008; Qiao *et al.*, 2009) in order to avoid target deformation that would favor electron heating, to prevent early pulse breakthrough due to transverse expansion, and to keep a monoenergetic spectrum against the inhomogeneous distribution of the laser intensity; to address this last issue, a target

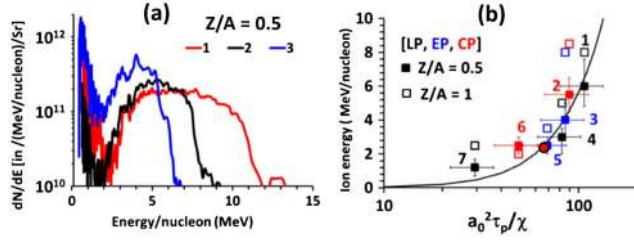


FIG. 27 (color online). (a) Three typical narrow-band spectra for $Z/A = 1/2$ impurity ions observed from thin ($0.1 \mu\text{m}$) metallic targets [for parameters of shots 1–3, see the explanation in (b)]. (b) Peak energies for both ions with $Z/A = 1/2$ (filled squares) and protons with $Z/A = 1$ (empty squares) for seven shots with different polarization parameters [see, e.g., Eq. (11)]: $\epsilon = 0$ (LP), 0.47 (EP), and 0.88 (CP). The peak energy is plotted as a function of the parameter $a_0^2 \tau_p / \chi$, which corresponds to $(m_p/2m_e)\Omega\tau_p$ in our notations. The parameter set [a_0 , target material, thickness (μm), polarization] for the data points 17 is [15.5, Cu, 0.1, LP], [10, Cu, 0.05, CP], [13.8, Cu, 0.1, EP], [7.5, Al, 0.1, LP], [6.9, Al, 0.1, EP], [13.6, Al, 0.5, CP], and [14.1, Al, 0.8, LP], respectively. The circle is the data point from Henig *et al.* (2009c). The solid line is the LS scaling (35). From Kar *et al.*, 2012.

with modulated surface density was also proposed (M. Chen *et al.*, 2009). In contrast to these studies Yan *et al.* (2009b) used a Gaussian intensity profile and found the formation of a narrow, high-energy ion bunch via a self-organization mechanism somewhat similar to that inferred by Bulanov *et al.* (2010b). Another open issue is the stability of the foil against transverse perturbations.²³ Recent simulation studies characterized regimes of efficient LS-RPA for linearly polarized pulses at irradiances $\sim 10^{21} \text{ W cm}^2 \mu\text{m}^2$ (Dover and Najmudin, 2012; Qiao *et al.*, 2012).

Possible indications of the onset of the LS regime have recently been provided in an experiment performed using 800 fs, $3 \times 10^{20} \text{ W cm}^{-2}$ high-contrast (10^9) pulses from the VULCAN laser and very thin ($\sim 0.1 \mu\text{m}$) metallic targets (Kar *et al.*, 2012). Narrow-band spectra with peak energies up to $\approx 10 \text{ MeV/nucleon}$ were observed for both proton and heavier $Z/A = 1/2$ ions present as surface impurities [see Fig. 27(a)], while heavier bulk ions had a broad spectrum at lower energies. The peak energies scaled with the fluence parameter as $\sim \mathcal{F}_\infty^2 \sim a_0^4 t_p^2$ [see Fig. 27(b)], in agreement with Eq. (35) for nonrelativistic ions, and differently from scalings as a_0 , a_0^2 , or $a_0^2 t_p$ which have been inferred for TNSA or for other mechanisms effective for ultrathin targets (see Sec. IV.C). The $Z/A = 1$ peaks are at slightly higher energy than the $Z/A = 1/2$ ones, suggesting that the LS stage is accompanied by a multispecies expansion (see Sec. III.C.3) in the sheath field where protons gain additional energy and the spectral peak separation may be further enforced.

The scaling plot in Fig. 27(b) also contains data from Henig *et al.* (2009c) who investigated LS using 45 fs, CP pulses at ultrahigh contrast ($\sim 10^{11}$) and $\sim 5 \times 10^{19} \text{ W cm}^{-2}$ intensity, and few-nm DLC foils. Experimental spectra of

fully ionized C^{6+} ions show a difference between linearly and circularly polarized pulses, with a broad peak at $\approx 30 \text{ MeV}$ appearing in the latter case, and reduced electron heating for CP. More recent experimental data by Dollar *et al.* (2012) using tightly focused ($f/1$) pulses with intensity up to $2 \times 10^{21} \text{ W cm}^{-2}$ showed a weak difference between CP and linear polarization (LP), which was attributed to the early deformation of the thin targets causing excessive electron heating. Recently, preliminary indications of a transverse instability resulting in spatial modulations of the accelerated proton beam have been reported (Palmer *et al.*, 2012).

To summarize the experimental evidence, to date there is a confirmation of the expected LS scaling, but also indications of significant detrimental effects. The observed ion spectrum is relatively broad, suggesting that transverse inhomogeneity and heating effects need to be reduced. In perspective, the relatively slow growth of the ion energy with time (see Fig. 25) might pose the challenge to increase the acceleration length against the effect of, e.g., pulse diffraction and instabilities.

B. Collisionless shock acceleration

Acceleration of particles by shock waves (briefly, shocks) in plasmas is a problem of great interest in astrophysics (Martins *et al.*, 2009). The existence of an ion component that is reflected by the shock front is actually integral to the formation of the collisionless, electrostatic shock waves in basic fluid theory, where the electrons are assumed to be in a Boltzmann equilibrium (Forslund and Shonk, 1970; Forslund and Freidberg, 1971; Tidman and Krall, 1971). In the frame moving at the shock velocity, ions are reflected by the shock if the height of the electrostatic potential barrier Φ_{max} at the front is such that $Ze\Phi_{\text{max}} > m_i v_1^2/2$, with v_1 the velocity of the ion component in the shock frame. Behind the shock front, the fields have an oscillatory behavior. Reflected ions initially at rest acquire a velocity in the laboratory frame equal to $2v_{\text{sho}}$, where v_{sho} is the shock front velocity.

CSA was proposed as an ion acceleration mechanism in superintense laser interaction with an overdense plasma on the basis of PIC simulations by Denavit (1992) and Silva *et al.* (2004).²⁴ In the latter work simulations showed the generation of shocks with high Mach numbers $M = v_{\text{sho}}/c_s = 2-3$, where the sound speed is estimated using the hot electron energy as the temperature, i.e., $T_h \approx \mathcal{E}_p$ [Eq. (6)]. The shocks are generated at the front surface with a velocity close to v_{HB} given by Eq. (29), consistently with the assumption that they are driven by the piston action of radiation pressure. By estimating $v_{\text{sho}} \approx v_{\text{HB}}$,²⁵ in the

²⁴In experiments on underdense plasmas created either by using gas jet targets (Wei *et al.*, 2004) or by the effect of long prepulses in solid targets (Habara *et al.*, 2004b), the observation of ion acceleration along the radial direction has been attributed to radial shock generation in a laser-driven channel.

²⁵Note that $v_{\text{sho}} \approx v_{\text{HB}}$ implies that “reflected” ions directed into the bulk will have a velocity $\sim 2v_{\text{HB}}$, i.e., twice the surface recession velocity, as the fastest ions generated by the piston action in HB acceleration (see Sec. IV.A.1). This similarity may explain why HB and CSA are often confused in the literature.

²³See, e.g., Pegoraro and Bulanov (2007), Klimo *et al.* (2008), Tikhonchuk (2010), T.-P. Yu *et al.* (2010), Chen *et al.* (2011), and Adusumilli, Goyal, and Tripathi (2012).

strongly relativistic limit $a_0 \gg 1$ the condition to obtain supersonic shocks driven by radiation pressure ($M > 1$) can be written as $\sqrt{2}a_0 > n_e/n_c$. The reflected ions may get further acceleration by the transient sheath field at the rear surface as in TNSA, eventually producing a plateau in the ion spectrum. A similar signature was observed experimentally by Zepf *et al.* (2003) and thus interpreted as evidence of the front side contribution to ion acceleration, in contrast to pure TNSA at the rear side of the target. Under particular conditions, the staged CSA-TNSA acceleration might produce the highest energy component in the ion spectrum as observed in simulation studies (d'Humières *et al.*, 2005; Chen *et al.*, 2007) which, however, also suggest lower efficiency and brilliance with respect to pure TNSA.

Recently, CSA has been indicated as the mechanism responsible for monoenergetic acceleration of protons up to 22 MeV (see Fig. 28) in the interaction of CO₂ laser pulses with hydrogen gas jets at intensities up to $6.5 \times 10^{16} \text{ W cm}^{-2}$ corresponding to $a_0 = 2.5$ (Haberberger *et al.*, 2012). The particular temporal structure of the laser pulse, i.e., a 100 ps train of 3 ps pulses, was found to be essential for the acceleration mechanism, since no spectral peaks were observed for a smooth, not modulated pulse. Comparison with PIC simulations suggested that the multiple pulses lead to efficient generation of suprathermal electrons, and that this process (rather than radiation pressure) drives the shocks which eventually accelerate protons. Simulations also suggest that the process could scale in order to produce 200 MeV protons at $10^{18} \text{ W cm}^{-2}$ that may be foreseeable with future CO₂ laser development. Such a scheme based on gas lasers and gas jet target would have the advantage of high-repetition rate operation, but the efficiency per shot might be low with respect to other approaches: in the experiment of Haberberger *et al.* (2012) the number of ions ($\sim 2.5 \times 10^5$) in the narrow spectral peak at $\approx 22 \text{ MeV}$ for a 60 J pulse energy implies a conversion efficiency of $\sim 10^{-8}$.

In addition to collisionless shocks, the standard fluid theory also predicts solitons (Tidman and Krall, 1971) propagating at the velocity v_{sol} with $1 < v_{\text{sol}}/c_s \leq 1.6$. These solitons are characterized by $Ze\Phi_{\text{max}} < m_i v_{\text{sol}}^2/2$ and are thus transparent to background ions “by construction.” However, the generation of electrostatic solitons may lead to ion acceleration in some circumstances, e.g., when the soliton breaks in the expanding rear sheath due to the effect of the plasma flow (Zhidkov *et al.*, 2002). Additional simulation studies of shock and solitary wave acceleration have been reported by He *et al.* (2007), Liu *et al.* (2009), and Macchi, Nindrayog, and Pegoraro (2012).

C. Transparency regime: Breakout afterburner

If ultrathin foils are used as targets (which requires ultrahigh-contrast, prepulse-free conditions), the expansion of the foil may lead to the onset of transparency during the short-pulse interaction, when the electron density n_e is further decreased down to the cutoff value (of the order of γn_c due to relativistic effects, see Sec. II.A). While this effect limits the energy attainable via RPA (see Sec. IV.A.2), it can lead to enhanced ion acceleration via different mechanisms.

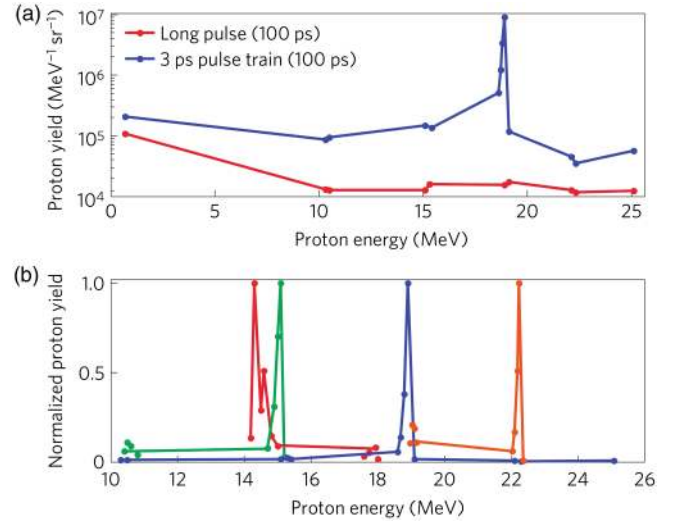


FIG. 28 (color online). Proton spectra from CO₂ laser interaction with a hydrogen gas jet. (a) Different spectra for a smooth (long) pulse (lower line) and a pulse train of 3 ps spikes (upper line); in the latter case, a peak appears in the spectrum. (b) Narrow spectra obtained in different shots. See text for parameters. From Haberberger *et al.*, 2012.

Several related experiments were performed at the TRIDENT laser facility at LANL, using pulse durations in the 500–700 fs range. C⁶⁺ ions with energies up to 15 MeV per nucleon were observed by irradiating DLC foils with $\sim 40 \text{ J}$, $\sim 7 \times 10^{19} \text{ W cm}^{-2}$ pulses, for an optimal thickness of 30 nm that is determined by the condition that relativistic transparency occurs at the pulse peak (Henig *et al.*, 2009b). Figure 29 shows spectra for different polarizations. For more energetic and intense pulses ($\sim 80 \text{ J}$, $10^{21} \text{ W cm}^{-2}$) and thicker targets (140 nm), broad C⁶⁺ spectra with higher cutoff energies beyond 40 MeV/nucleon were observed, and the inferred conversion efficiency was $\sim 10\%$ (Hegelich *et al.*, 2011). Narrower C⁶⁺ spectra ($\Delta\mathcal{E}_i/\mathcal{E}_i \approx 15\text{--}20\%$) at lower energies ($\sim 3\text{--}10 \text{ MeV}$) were observed using either loose focusing or circular polarization (Hegelich *et al.*, 2011; Jung *et al.*, 2011b). Recently, energies up to 80 MeV/nucleon for carbon and 120 MeV/protons have been communicated (Hegelich, 2011). The onset of relativistic transparency in these conditions was recently investigated in detail with ultrafast temporal resolution (Palaniyappan *et al.*, 2012).

Simulation studies of this regime show that the increase of the cutoff energy is related to enhanced and volumetric

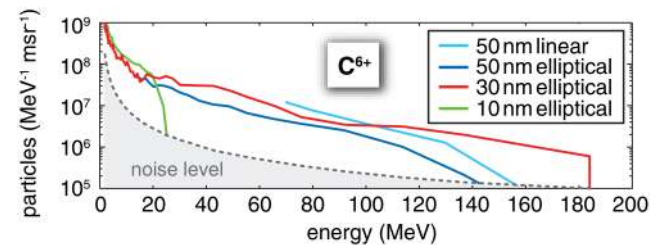


FIG. 29 (color online). Spectra of C⁶⁺ ions from laser interaction with ultrathin targets in the regime of relativistic transparency as a function of target thickness and laser polarization. From Henig *et al.*, 2009b.

heating of electrons as the target becomes transparent, leading to a stronger accelerating field for ions; the name “break-out afterburner” was proposed for such regime by the Los Alamos group (Yin *et al.*, 2007). 3D PIC simulations of BOA have been reported by Yin *et al.* (2011a). Modeling of BOA is not simple as the process appears to involve different stages. Analytical descriptions of BOA have been reported by Albright *et al.* (2010) and Yan *et al.* (2010) and a scaling of the maximum ion energy $\mathcal{E}_{\max} \approx (1 + 2\alpha)ZT_e$, with T_e the electron temperature and α a phenomenological parameter (estimated to be ~ 3 from simulations), has been proposed. A fast growing relativistic Buneman instability, excited due to the relative drift between electron and ions, has been invoked as a mechanism enhancing the coupling with ions (Albright *et al.*, 2007). Theoretical explanations for narrow C^{6+} spectra, based on an electromagnetic “ion-soliton” model (fundamentally different from electrostatic solitons described in Sec. IV.B), have been discussed by Yin *et al.* (2011b).

D. Acceleration in near-critical and underdense plasmas

A number of studies have been devoted to ion acceleration in near-critical plasmas with electron density close to the cutoff value ($n_e \approx n_c$), in order to allow a more efficient generation of hot electrons to drive TNSA. Production of a low-density plasma by a laser prepulse has been investigated for laser and target parameters such that at the time of interaction with the main short pulse the preplasma was either underdense (Matsukado *et al.*, 2003) or slightly overdense (Yogo *et al.*, 2008); in the latter experiment, protons up to 3.8 MeV are observed at 10^{19} W cm $^{-2}$ intensity and directed slightly off the normal to the target rear side. Analysis of these experiments gave indication of a regime where the pressure due to a self-generated magnetic field at the rear surface strongly contributes to charge separation.

An alternative strategy to reduce the electron density is to use special target materials such as foams, which may be manufactured in order to have an average value of n_e slightly larger, or even lower than n_e (the average is meant over a length larger than the typical submicrometric scale of inhomogeneity). Experimentally, proton acceleration in low-density foams [$n_e = (0.9 - 30)n_c$] has been investigated by Willingale *et al.* (2009, 2011a) at intensities up to 10^{21} W cm $^{-2}$, showing that the proton energy is close to that obtained for solid foils and the same laser pulse for the lowest density value ($n_e \approx 0.9n_c$). In this experiment, proton acceleration has mostly been investigated as an indication of the onset of relativistic transparency, leading to enhanced laser penetration and collimation of hot electrons and ions by self-generated magnetic fields. Recent simulation studies of ion acceleration in a solid target covered with foam layers (Zani *et al.*, 2013) have also been reported (Nakamura *et al.*, 2010; Sgattoni *et al.*, 2012).

Experimental investigations of ion acceleration using gas jet targets, with typical densities below 10^{20} cm $^{-3}$, have also been performed. These experiments include the already described investigations of hole boring RPA (see Sec. IV.A.1) and shock acceleration (see Sec. IV.B) using CO $_2$ lasers for which gas jets are near-critical targets. Using optical or

near-infrared lasers, several experiments of high-intensity laser interaction with underdense gas jets have reported observations of energetic ions accelerated in the *radial* direction with respect to the laser pulse propagation axis (Krushelnick *et al.*, 1999; Sarkisov *et al.*, 1999; Wei *et al.*, 2004) by the electric field created by the electron displacement in the channel drilled by the ponderomotive force. The ion spectrum may provide information on the self-focusing and channeling dynamics of the laser pulse and the acceleration mechanism shows indeed some similarity with those active in the interaction with solid targets (Macchi, Ceccherini *et al.*, 2009). However, radial acceleration of ions is of modest interest for applications since the ions are not collimated at all.

A collimated emission in the forward direction from an underdense He gas jet was reported by Willingale *et al.* (2006). Using a laser pulse of 1 ps duration, energy up to 340 J, and intensity up to 6×10^{20} W cm $^{-2}$, He ions up to 40 MeV were observed collimated in a beam with $<10^\circ$ aperture. The data were interpreted by assuming that a large electric field was generated at the rear side of the gas jet by escaping hot electrons. Different from TNSA in solid targets, the mechanism was considered to be effective despite the relatively long density scale length at the rear surface because a larger fraction of hot electrons was generated by electron acceleration in the underdense plasma. Further analysis of simulations of the experiment (Willingale *et al.*, 2007) also showed a significant contribution due to the generation of a quasistatic magnetic field at the rear surface, which in turn enhances the accelerating electric field via magnetic pressure and induction effects according to the model by Bulanov and Esirkepov (2007) that was also used to explain the above mentioned experimental results by Yogo *et al.* (2008) in a near-critical plasma. Figure 30 shows a sketch of such a mechanism.

Acceleration sustained by a magnetic field was also indicated as the dominant mechanism in an experiment by Fukuda *et al.* (2009), where ions in a 10–20 MeV range and collimated in a 3.4° aperture cone were observed in the interaction of a 7×10^{17} W cm $^{-2}$, 40 fs laser pulse with an underdense gas jet where CO $_2$ clusters were formed.

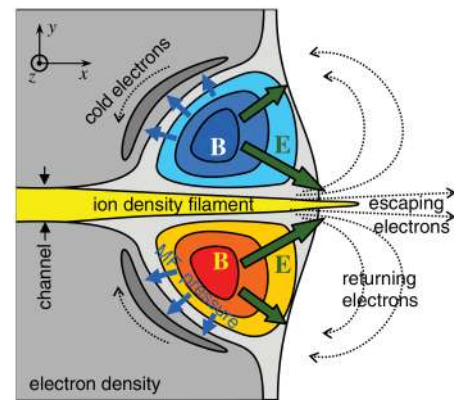


FIG. 30 (color online). Sketch of magnetic field sustained acceleration of ions, showing the topology of the magnetic and electric fields and the flows of escaping and returning electron currents. From Bulanov and Esirkepov, 2007.

The role of the clusters was apparently that of enhancing the self-channeling and focusing of the laser pulse, leading to an increase of the intensity in the plasma, rather than contributing to ion acceleration via cluster explosions.

The generation of collimated ions from underdense plasmas at ultrahigh intensities ($> 10^{21} \text{ W cm}^{-2}$) was investigated theoretically and with numerical simulations more than a decade ago (Esirkepov *et al.*, 1999; Bulanov *et al.*, 2000; Sentoku *et al.*, 2000). In particular, in these papers it was predicted that, for $a_0 > (m_i/m_e)^{1/2} \simeq 43A^{1/2}$, the effective inertia of the highly relativistic electrons in the laser field becomes comparable to those of ions. As a consequence the ions closely follow the electron displacement due to the ponderomotive action and the acceleration process may become similar to what is observed in an overdense plasma. A few more recent simulation studies investigated a regime where a small ion target is placed in an underdense plasma (Shen *et al.*, 2009; L.-L. Yu *et al.*, 2010). The superintense laser pulse accelerates and overruns the ion target and then generates a wakefield in the underdense plasma, where ions may be trapped and accelerated in a way similar to the well-known scheme for laser acceleration of electrons (Esarey, Schroeder, and Leemans, 2009). In those simulations GeV energies were reached, but the required laser pulses should have multipetawatt power and multi-kJ energy, still far beyond present-day laser technology.

E. Resistively enhanced acceleration

Already during the “front versus rear side acceleration” debate related to experiments reported in 2000 (see Sec. I), it was suggested that protons may also be accelerated in the target bulk through a mechanism depending on the target resistivity η (Davies, 2002). The electric field generated in the target bulk to provide the return current $\mathbf{E} = \mathbf{j}_r/\eta$ (see Sec. II.B.3) increases for low η reducing the penetration of hot electrons through the target and at the same time favoring acceleration in the front and bulk regions versus TNSA. The mechanism was theoretically investigated by Gibbon (2005a) using a collisional tree-code approach.

Indications of dominant front side acceleration due to resistivity effects have been reported in solid plastic targets (Lee *et al.*, 2008, 2011) and also in low-density foams (Li *et al.*, 2005), where an anomalously high resistivity might be due to spatially localized fields in the locally inhomogeneous material.

V. CURRENT AND FUTURE APPLICATIONS

A. Proton radiography

The use of ion beams, and particularly proton beams, for radiographic applications was first proposed in the 1960s (Koehler, 1968). Quasimonochromatic beams of ions from conventional accelerators have been used for detecting areal density variations in samples via modifications of the proton beam density cross section, caused by differential stopping of the ions, or by scattering. Radiography with very high-energy protons ($\sim 1\text{--}10 \text{ GeV}$) is being developed as a tool for weapon testing (King *et al.*, 1999). Ion beams from accelerators have also been employed on some occasions for electric

field measurements in plasmas, via the detection of the proton deflection, e.g., by Mendel and Olsen (1975). In practice, the difficulties and high cost involved in coupling externally produced particle beams of sufficiently high energy to laser-plasma experiments (or indeed magnetic confinement experiments) and the relatively long duration of ion pulses produced from conventional accelerators have limited the application of such diagnostic techniques.

The unique properties of protons from high-intensity laser-matter interactions, particularly in terms of spatial quality and temporal duration, have opened up a totally new area of application of proton probing or radiography. As seen in Sec. III.B, TNSA protons from a laser-irradiated foil can be described as emitted from a virtual, pointlike source located in front of the target (Borghesi *et al.*, 2004). A point-projection imaging scheme is therefore automatically achieved with magnification M set by the geometrical distances at play. Backlighting with laser-driven protons has intrinsically high spatial resolution, which, for negligible scattering in the investigated sample, is determined by the size d of the virtual proton source and the width δs of the point spread function of the detector (mainly due to scattering near the end of the proton range), offering the possibility of resolving details with spatial dimensions of a few μm . As discussed in Sec. II.E, multilayer detector arrangements employing RCFs or CR39 layers offer the possibility of energy-resolved measurements despite the broad spectrum. Energy dispersion provides the technique with an intrinsic multi-frame capability. In fact, since the sample to be probed is situated at a finite distance from the source, protons with different energies reach it at different times. As the detector performs spectral selection, each RCF layer contains, in a first approximation, information pertaining to a particular time, so that a movie of the interaction made up of discrete frames can be taken in a single shot. Depending on the experimental conditions, 2D proton deflection map frames spanning up to 100 ps can be obtained. The ultimate limit of the temporal resolution is given by the duration of the proton burst at the source, which is of the order of the laser pulse duration.

Several radiographic applications of laser-produced protons have been reported to date and radiographs of objects for various size and thickness (down to a few $\sim \mu\text{m}$) have been obtained (Cobble *et al.*, 2002; Roth *et al.*, 2002; Borghesi *et al.*, 2004; Mackinnon *et al.*, 2006). Density diagnosis via proton radiography has potential application in ICF. A preliminary test studying the compression of empty CH shells under multibeam isotropic irradiation at the moderate irradiance of $10^{13} \text{ W cm}^{-2}$ has been carried out at the Rutherford Appleton Laboratory (Mackinnon *et al.*, 2006). Radiographs of the target at various stages of compression were obtained. Modeling of proton propagation through a target and a detector carried out using Monte Carlo codes permits the retrieval of density and core size at maximum compression (3 g/cm^3 , $80 \mu\text{m}$) in good agreement with hydrodynamic simulations. Radiographic analysis of cylindrically compressed matter (Volpe *et al.*, 2011) and of shock wave propagation (Ravasio *et al.*, 2010) has also been carried out, although the available detail with low energy protons is limited.

The most successful applications to date of proton probing are related to the detection of electric and magnetic fields in plasmas (Borghesi *et al.*, 2002b; Mackinnon *et al.*, 2004). Jointly with a parallel technique using monoenergetic protons from fusion reactions driven from laser-driven compressions (Li *et al.*, 2006), proton probing with laser-accelerated protons has provided in this way novel and unique information on a broad range of plasma phenomena. The high temporal resolution is here fundamental in allowing the detection of highly transient fields following short-pulse interaction.

Two main arrangements have been explored. In *proton imaging*, i.e., simple backlighting projection of the sample (Borghesi *et al.*, 2001, 2002b), the deflections cause local modulations in the proton density n_p across the proton beam cross section, which, under the approximation of small deflections, can be written as

$$\frac{\delta n_p}{n_p} \simeq -\frac{eL}{2\epsilon_p M} \int_{-b/2}^{+b/2} \nabla_{\perp} \left(\mathbf{E} + \frac{\mathbf{v}_p}{c} \times \mathbf{B} \right) dx, \quad (37)$$

where v_p and ϵ_p are the proton velocity and energy, M is the projection magnification, L is the distance between the plasma and the detector, and the integral is along the trajectory of the protons, crossing a region $|x| < b/2$, where the fields \mathbf{E} and \mathbf{B} to be probed are present. Under simplified assumptions the above formula can be used to yield line-averaged values of the fields (Sarri *et al.*, 2010a). In *proton deflectometry*, thin meshes are inserted in the beam between the proton source and the object as “markers” of the different parts of the proton beam cross sections (Mackinnon *et al.*, 2004). The meshes impress a modulation pattern in the beam before propagating through the electric field configuration to be probed. The beam is in this way effectively divided in a series of beamlets, and their deflection can be obtained directly from the pattern deformation. A technique employing two grids to generate a set of moiré fringes has also been proposed as a way to increase the sensitivity to small electric fields (Mackinnon *et al.*, 2003).

The proton probing technique has provided uniquely detailed information on nonlinear phenomena in high-intensity laser-plasma interactions, such as ion acoustic solitons and collisionless shock waves (Romagnani *et al.*, 2008), phase-space electron holes (Sarri *et al.*, 2010b), self-organized field structures in counterstreaming plasmas (Kugland *et al.*, 2012), the charge-displacement channel formation dynamics following relativistic self-focusing of laser pulses (Kar *et al.*, 2007; Sarri *et al.*, 2010c; Willingale *et al.*, 2011b), and the evolution of remnants of coherent electromagnetic structures and instabilities of various types (Borghesi *et al.*, 2002a, 2005; Romagnani *et al.*, 2010; Sarri *et al.*, 2010d, 2011b). Application to ns laser-produced plasmas of ICF interest has also allowed one to investigate laser filamentation in underdense plasmas (Lancia *et al.*, 2011; Sarri *et al.*, 2011a), plasma expansion inside hohlraums (Sarri *et al.*, 2010a), and self-generation of magnetic fields (Nilson *et al.*, 2006; Cecchetti *et al.*, 2009; Willingale *et al.*, 2010; Sarri *et al.*, 2011a). As an example of the use of a time-resolved proton diagnostic, Fig. 13 reports data from an experiment where the protons are used to probe the rear of a foil following ultra-intense irradiation of the front of the foil (Romagnani *et al.*, 2005). The probe proton pattern is modified by the fields

appearing at the target rear as a consequence of the interaction, and the technique effectively allows spatially and temporally resolved mapping of the electrostatic fields associated with TNSA acceleration from the foil (see Sec. III.A). Figure 13(a) shows the setup for both imaging and deflectometry measurements. Figures 13(b)–13(g) correspond to proton images at different times taken in a single shot, resolving the expansion of the plasma sheath and highlighting the multiframe capability of this diagnostic.

It should be noted then on the basis of Eq. (37) it may not be possible in principle to unambiguously attribute the measured deflections to the sole action of either electric or magnetic fields. Confidence in the interpretation of observed patterns can be increased by supporting the analysis method of both imaging and deflectometry data with particle tracing codes. Such codes simulate the propagation of the protons through a given space- and time-dependent field configuration, which can be modified iteratively until the computational proton profile reproduces the experimental ones. State-of-the-art tracers allow realistic simulations including experimental proton spectrum and emission geometry, as well as detector response. Moreover, in some specific experiments it was possible to provide evidence of magnetic fields, discriminating their effect on probe protons from that due to electric fields, by using different probing directions (Cecchetti *et al.*, 2009) or even exploiting the divergence of the probe beam (Romagnani *et al.*, 2010). An example is given in Fig. 31 where the presence of an azimuthal \mathbf{B} field

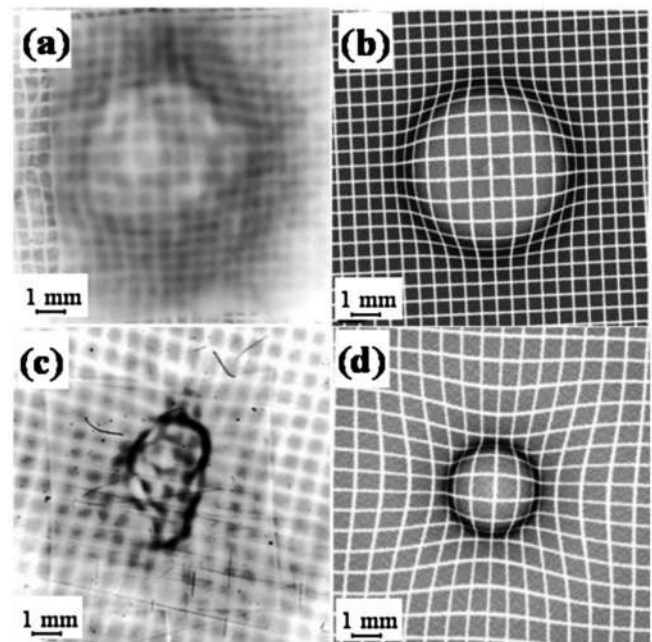


FIG. 31. Proton probing of magnetic fields. (a), (c) Probing deflectogram of a laser-irradiated foil (ns pulse, $10^{15} \text{ W cm}^{-2}$ on a $6 \mu\text{m}$ Al foil) obtained with a 5.5 MeV proton beam facing the foil, entering from the nonirradiated side in (a) and from the opposite, laser-irradiated side in (c). The inversion of the deflection pattern reveals the effect of a toroidal \mathbf{B} field [the asymmetrical pattern in (c) is due to a nonideal intensity distribution in the focus]. (b), (d) Particle tracing simulations for the conditions of (a) and (c) assuming a suitably parametrized \mathbf{B} field. From Cecchetti *et al.*, 2009.

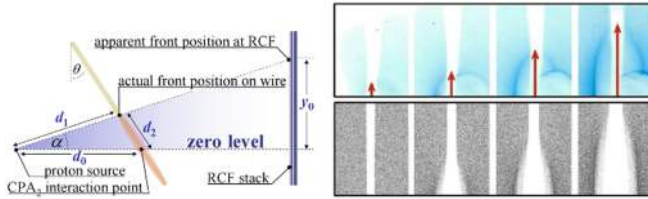


FIG. 32 (color online). The left shows the proton imaging setup with increased dynamical range in the time domain (Quinn *et al.*, 2009a, 2009b). By placing a wire target at an angle with respect to the probe beam it is possible to resolve the propagation at a velocity close to c of a field front along the laser-irradiated wire, as shown in the right (top: experimental images, bottom: particle tracing simulations). From Quinn *et al.*, 2009a.

has been revealed with mesh deflectometry by either a compression or outward dilation of the mesh lines, depending on whether the \mathbf{B} field has clockwise or counterclockwise direction compared to the propagation direction of the probe beam.

The divergence of the probe beam also implies that the effective probing time is a function of the position on the image plane because of the different time of flight for protons at different angles. This effect has to be taken into account for measurement of field structures propagating at relativistic speeds (Kar *et al.*, 2007; Quinn *et al.*, 2009a) and actually may improve the capability to characterize such structures, as it was obtained by a slightly modified arrangement (Quinn *et al.*, 2009b). This allowed one to observe the ultrafast, transient field front associated with the early stage of TNSA where electromagnetic effects come into play (see Fig. 32). A *proton streak deflectometry* technique for obtaining continuous temporal mapping (but only one spatial dimension is resolved) has also been proposed in which the energy resolution is achieved by means of magnet dispersion (Sokollik *et al.*, 2008).

B. Production of warm dense matter

Laser-driven ions have found application in a number of experiments aimed to heat up solid-density matter via isochoric heating, and create so-called warm dense matter (WDM) states, i.e., matter at 1–10 times solid density and temperatures up to 100 eV (Koenig *et al.*, 2005) of broad relevance to material, geophysical, and planetary studies (Ichimaru, 1982; Lee *et al.*, 2003). The high-energy flux and short temporal duration of laser-generated proton beams are crucial parameters for this class of applications. WDM states can be achieved by several other means, e.g., x-ray heating (Tallents *et al.*, 2009) and shock compression (Kritcher *et al.*, 2008). However, when studying fundamental properties of WDM, such as the equation of state (EOS) or opacity, it is desirable to generate large volumes of uniformly heated material; ion beams, which can heat the material in depth, are in principle better suited to this purpose than the methods described above.

Heating of solid-density material with ions can be achieved with accelerator-based or electrical-pulsed ion sources; see, e.g., Bailey *et al.* (1990), Hoffmann *et al.* (2000), and Tahir *et al.* (2006). However, the relatively

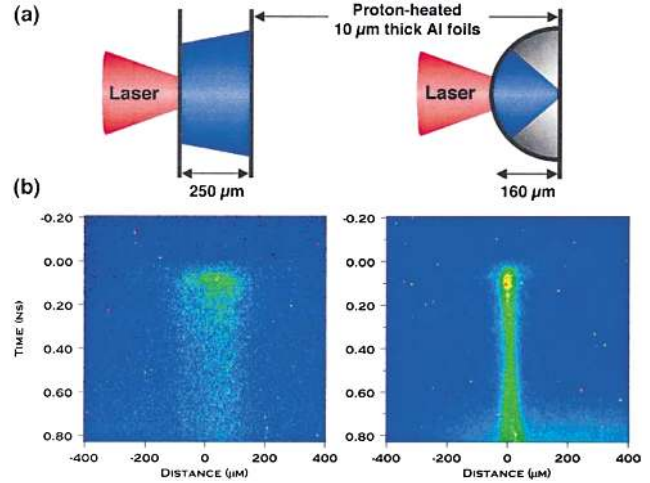


FIG. 33 (color online). Heating of solid targets by protons. (a) Experimental setup for flat and focusing target geometries. Each target consists of a flat or hemispherical 10 μm thick Al foil irradiated by the laser, and a flat 10 μm thick Al foil to be heated by the protons. (b) Corresponding streak camera images showing space- and time-resolved thermal emission at 570 nm from the rear side of the proton-heated foil. Proton focusing by the hemispherical foil leads to a stronger, more localized heating. From Patel *et al.*, 2003.

long durations of ion pulses from these sources (1–10 ns) imply that the materials undergo significant hydrodynamic expansion already during the heating period. On the contrary, laser-generated proton beams, emitted in ps bursts, provide a means of very rapid heating, on a time scale shorter than the hydrodynamic time scale. By minimizing the distance between the ion source and the sample to be heated, it is possible to limit the heating time to tens of ps. The target then stays at near-solid density before significant expansion occurs, and the WDM properties can be investigated within this temporal window.

The first demonstration of laser-generated proton heating was obtained by Patel *et al.* (2003). In this experiment a 10 J pulse from the 100 fs JanUSP laser at LLNL was focused onto an Al foil producing a 100–200 mJ proton beam used to heat a second Al foil. Target heating was monitored via time-resolved rear surface emission, as shown in Fig. 33. A focused proton beam, produced from a spherically shaped target (see Sec. III.E.3), was seen to heat a small target region to a temperature (of ~ 23 eV). With a similar ion focusing arrangement on a higher energy laser system, Gekko at ILE Osaka, Snavely *et al.* (2007) demonstrated secondary target heating up to 80 eV by imaging both visible and extreme-ultraviolet Planckian emission from the target's rear surface.

Subsequent experiments have investigated the properties of the WDM produced with this approach with a number of diagnostics, either passive or in pump-probe configurations, combined to self-consistent modeling of sample heating and expansion. Warm solid Al at temperatures up to 15–20 eV (Dyer *et al.*, 2008; Mančić *et al.*, 2010b) and carbon up to ~ 2 eV (Roth *et al.*, 2009) have been produced in this manner. Dyer *et al.* (2008) reconstructed the EOS of the heated material by measuring the temperature and expansion rate of the heated

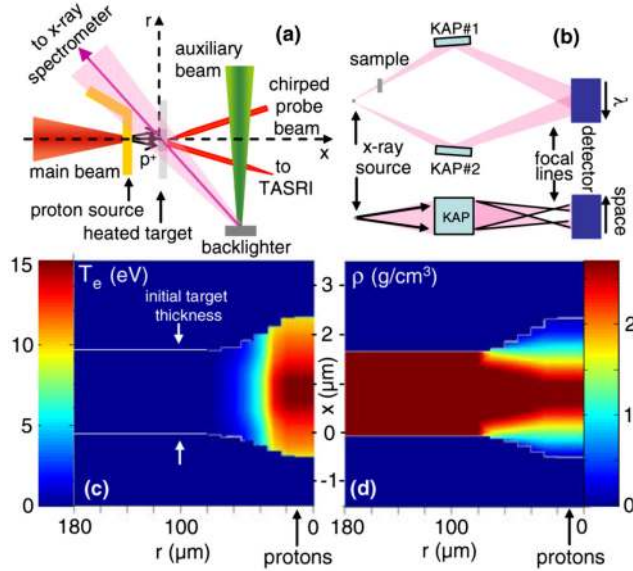


FIG. 34 (color online). Setup for x-ray probing of a solid Al target heated by protons: (a) top view of the experiment, (b) schematic of the x-ray spectrometer; (c), (d) snapshots of temperature and density profiles of the heated 1.6 μm thick Al foil as given by self-consistent simulations, demonstrating isochoric heating up to 15 eV temperatures. From [Mančić et al., 2010a](#).

target, via streaked thermal emission and chirped pulse interferometry.

Pump-probe arrangements have been used in recent, more sophisticated experiments, which have provided novel information on the transition phase between cold solid and plasmas in isochorically heated Al and C targets. [Mančić et al. \(2010a\)](#) investigated the short range disordering of warm Al at solid density by applying time-resolved x-ray absorption near-edge spectroscopy (see Fig. 34). Progressive smoothing of spectral features near the K edge allowed one to place an upper bound on the onset of ion lattice disorder within the heated solid-density medium of 10 ps. [Pelka et al. \(2010\)](#) recently diagnosed ultrafast melting of carbon samples, by x-ray scattering techniques, which allowed determination of the fraction of melted carbon in the heated sample. Comparison to predictions based on different theoretical descriptions of the EOS of carbon indicates a departure from existing models, with implications for planetary core studies.

In all the experiments mentioned above the isochoric heating by the protons is volumetric, but not uniform ([Brambrink et al., 2007](#)); see, e.g., Fig. 34(c). Uniform heating requires some degree of proton energy selection, and choosing the sample thickness so that the Bragg peak of the selected protons does not fall within the sample, as suggested, for example, by [Schollmeier et al. \(2008\)](#).

C. Fast ignition of fusion targets

The traditional route to ICF ([Atzeni and Meyer-ter-Vehn, 2004](#)) relies on the driven implosion of a pellet of thermonuclear fuel (a DT mixture). Ignition occurs in a central “hot spot” following pulse compression. This approach requires an extremely high symmetry and is prone to

hydrodynamics instabilities, making ICF a historically difficult goal.

In the fast ignition (FI) concept [see [Key \(2007\)](#) for a compact review] ignition is driven by an external trigger, creating the hot spot in a time much shorter than the typical fuel disassembly time. Hence, ignition is separated from pulse compression. The FI approach might relax symmetry and stability requirements, reduce the energy need for ignition, and allow fuel burn in an isochoric regime with high fusion gain.

In the original FI proposal by [Tabak et al. \(1994\)](#), the ignitor beam consisted of multi-MeV electrons accelerated by a petawatt laser pulse via the mechanisms described in Sec. II.B. Subsequent research showed that, besides generating an electron beam with enough power to ignite, most problematic were the issues of energy transport and deposition in the core. Concerning the latter issue, the energy deposition profile of electrons is a smooth function, making it difficult to produce a localized hot spot.

Observation of efficient generation of multi-MeV proton beams in petawatt experiments ([Hatchett et al., 2000](#); [Snively et al., 2000](#)) soon stimulated the proposal of the use of such protons as the ignitor beam ([Roth et al., 2001](#)). The most promising features of proton beam ignition as claimed were the highly localized energy deposition profile (see Fig. 3), the low emittance of the beam, and its focusability, for instance, by parabolically shaping the rear side of the proton-producing target as suggested by numerical simulations ([Ruhl et al., 2001](#); [Wilks et al., 2001](#)).

Detailed calculations by [Atzeni, Temporal, and Honrubia \(2002\)](#) and [Temporal, Honrubia, and Atzeni \(2002\)](#) addressed, in particular, the effects of the quasithermal energy distribution typical of TNSA protons, and of the related temporal dispersion. The latter could be beneficial for energy deposition since the proton stopping range increases with plasma temperature. Hence, heating due to the more energetic protons favors energy deposition by the less energetic ones which arrive later in the dense fuel region. A fit of simulations for a proton temperature of 5 MeV provided the following estimate of the ignition energy²⁶ \mathcal{E}_{ig} as a function of fuel density ρ and distance d between proton source and fuel core:

$$\mathcal{E}_{\text{ig}} \simeq 90(d/\text{mm})^{0.7}(\rho/100 \text{ g cm}^{-3})^{-1.3} \text{ kJ.} \quad (38)$$

Integration of the foil inside the cone of conical ICF targets already designed for electron FI was then proposed in order to reduce d and thus \mathcal{E}_{ig} . This raised the issue of shielding the foil from preheating caused, e.g., by external radiation, which may jeopardize efficient TNSA (see Sec. III.E.1); a preliminary analysis was mentioned by [Geissel et al. \(2005\)](#). Figure 35 sketches the target and foil assembly and summarizes suitable parameters for proton FI with cone targets. [Temporal \(2006\)](#) and [Temporal, Honrubia, and Atzeni \(2008\)](#) investigated a similar scheme but used two proton beams with suitably shaped radial profiles, obtaining a 40% reduction of the ignition energy.

²⁶ \mathcal{E}_{ig} includes only the energy of the proton beam. The total energy of the laser driver is $\mathcal{E}_{\text{ig}}/\eta_p$ with $\eta_p < 1$ the conversion efficiency into protons.

competitive option. Several projects are currently active worldwide to explore the potential of laser-driven proton and ion sources for biomedical applications; see, e.g., Bolton *et al.* (2010), Borghesi *et al.* (2011), and Enghardt *et al.* (2011). In view of future applications, several authors have started to design possible delivery systems, including target chamber and shielding (Ma *et al.*, 2006), particle energy selection, and beam collimation systems to enable operation with the broadband and diverging laser-driven beams (Fourkal, Li, Ding *et al.*, 2003; Nishiuchi *et al.*, 2010b; Hofmann *et al.*, 2011).

While currently a relative energy spread $\Delta E/E \simeq 10^{-2}$ is required for optimal dose delivery over the tumor region, many have also modeled approaches in which the native broad spectrum of laser-accelerated ions is used to directly obtain the spread out Bragg peak distributions which are normally used to cover the tumor region (Fourkal *et al.*, 2007; Luo *et al.*, 2008) and more in general advanced methods exploiting the properties of laser-accelerated beams (Schell and Wilkens, 2010).

An important step in view of their future medical use is to assess the biological effect of laser-driven ions and highlight any peculiarity associated with their pulsed, ultrashort temporal profile. Yogo *et al.* (2009) first demonstrated the feasibility of cell irradiation studies using laser-driven protons, employing a suitable beam transport setup and then applied a refined technique to infer, via a clonogenic assay, the relative biological effectiveness (RBE) of ~ 2 MeV laser-accelerated protons, as compared to irradiation with a standard x-ray source (Yogo *et al.*, 2011), in human cancer cells. The RBE observed (1.2 ± 0.1) is comparable with literature results employing rf-accelerated protons of comparable linear energy transfer (LET) (Folkard, 1996). The dose required to

cause significant cell damage (typically 1 to several gray) was obtained in several irradiations taking place at 1 Hz repetition rate. Kraft *et al.* (2010) also carried out proton irradiations of cells, highlighting dose-dependent incidence of a double-strand DNA break in the cells (see Fig. 36).

The peculiar characteristics of laser-driven protons have required the development of innovative dosimetric approaches, as described, for example, by Fiorini *et al.* (2011) and Richter *et al.* (2011). In all these experiments, the dose [1–10 grays (Gy)] is delivered to the cells in short bursts of \sim ns duration. In experiments by Kraft *et al.* (2010) and Yogo *et al.* (2011) the dose is fractionated and the average dose rate is comparable to the one used in irradiations with conventional accelerator sources (~ 0.1 Gys $^{-1}$). In a recent experiment (Fiorini *et al.*, 2011; Doria *et al.*, 2012) employing a high-energy ps laser system, it was possible to reach up to 5 Gy in a single exposure, reaching dose rates as high as 10^9 Gys $^{-1}$. This allows access to a virtually unexplored regime of radiobiology, where, in principle, nonlinear collective effects (Fourkal *et al.*, 2011) on the cell due to the high proton density in the bunch may become relevant.

Besides cancer therapy, application of laser-driven ion beams in medical diagnosis has also been proposed. Multi-MeV proton beams can induce nuclear reactions in low-Z materials (see Sec. V.E) in order to produce neutrons of possible interest for boron neutron capture therapy for cancer, or short-lived positron emitting isotopes which may be employed in positron emission tomography (PET). PET has proven to be extremely useful in medical imaging of blood flow and amino acid transport and in the detection of tumors. Usually, reactions for PET are carried out by using up to 20 MeV protons or similar energy deuterons from cyclotrons with the concomitant problems of large size and cost and extensive radiation shielding. Production of short-lived isotopes via laser-driven proton beams may be feasible in the near future with the possibility of employing moderate energy, ultrashort, high-repetition tabletop lasers. Extrapolations based on present results point to the possibility of reaching the gigaBecquerel (GBq) activities required for PET if laser systems capable of delivering 1 J, 30 fs pulses focused at 10^{20} Wcm $^{-2}$ with kHz repetition will become available (Fritzler *et al.*, 2003; Lefebvre *et al.*, 2006) and economically competitive with existing technologies.

E. Nuclear and particle physics

The interaction of laser-driven high-energy ions with secondary targets can initiate nuclear reactions of various types, which as mentioned (see Sec. II.E) can be used as a tool to diagnose the beam properties. This also presents the opportunity of carrying out nuclear physics experiments in laser laboratories rather than in accelerator or reactor facilities, and to apply the products of the reaction processes in several areas. Reactions initiated by laser-accelerated high-Z ions have been studied in a number of experiments. McKenna *et al.* (2003a, 2003b, 2004) showed that reactions between fast heavy ions from a laser-produced plasma and stationary atoms in an adjacent “activation” sample create compound nuclei in excited states, which deexcite through the evaporation of protons, neutrons, and α particles. A similar experiment

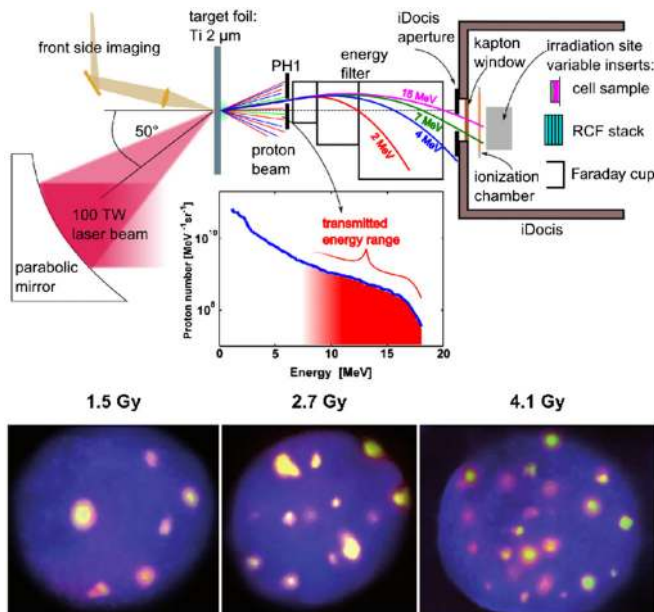


FIG. 36 (color online). Top: Overview of an experimental setup for integrated dosimetry and cell irradiation system by laser-accelerated protons. Bottom: Fluorescence microscopy view of SKX tumor cell nuclei irradiated with such system, showing that the number of DNA double-strand breaks (bright spots, yellow-pink in the color version) increases with the delivered dose. From Kraft *et al.*, 2010.

with protons driving nuclear reactions and excitations in a Cu target was reported by Hannachi *et al.* (2007). Nuclear reactions of interest for spallation physics have also been investigated by employing multi-MeV proton beams (McKenna *et al.*, 2005). The broad energy distribution of the beams is in this case advantageous for the determination of residual nuclide generation arising from specific spallation processes such as evaporation. In addition, MeV proton interaction with low- Z materials can produce short-lived isotopes²⁹ of medical interest, e.g., for PET diagnostic (see Sec. V.D).

Recently, a scheme of a “fission-fusion” process driven by RPA (see Sec. IV.A) was also proposed to produce neutron-rich nuclei in the range of the r process (Habs *et al.*, 2011); such studies, of relevance for astrophysical nucleosynthesis, would require intensities above 3×10^{22} W cm⁻² that may be available with next-generation short-pulse laser facilities.

Neutrons are an important product of the above mentioned nuclear reactions, with potential applications in cancer therapy, neutron radiography, radiation damage of materials, and transmutation of nuclear waste. The potential for laser-driven neutron sources is considerable and offers advantages over accelerator- and reactor-driven sources in terms of cost, compactness, brightness, and short duration for applications such as fast neutron radiography (Lancaster *et al.*, 2004) and studies of impulsive damage of matter (Perkins *et al.*, 2000). This has motivated several experiments on the production of neutrons initiated by laser-driven proton beams on secondary targets. Experiments carried out at the VULCAN laser facility revealed neutron yields up to 4×10^9 sr⁻¹ per pulse at a laser intensity of 3×10^{20} W cm⁻² (Yang *et al.*, 2004a), produced via the $^{11}\text{B}(p, n)^{11}\text{C}$ and $^7\text{Li}(p, n)^7\text{Be}$ reactions. The latter was also investigated by Youssef, Kodama, and Tampo (2006) as a diagnostic of proton acceleration. Neutron production was also observed in interactions with solid targets containing deuterium (typically deuterated plastic), which can be either directly irradiated by high-intensity laser pulses (Norreys *et al.*, 1998; Disdier *et al.*, 1999; Habara *et al.*, 2003, 2004b; Willingale *et al.*, 2011a) or irradiated by ions accelerated on a separate target (Fritzier *et al.*, 2002; Karsch *et al.*, 2003). In both cases the neutrons are produced in the course of fusion reactions of the type $\text{D}(d, n)^3\text{He}$ involving laser-accelerated deuterium ions as also observed in gaseous targets (Ditmire *et al.*, 1997; Grillon *et al.*, 2002). Numerical modeling and theoretical investigations of laser-driven neutron production have been carried out; see, e.g., Toupin, Lefebvre, and Bonnaud (2001), Macchi (2006), Davis and Petrov (2008, 2011), and Ellison and Fuchs (2010).

Application of laser-accelerated ions in particle physics requires “by definition” the ions to be relativistic, i.e., their total energy must exceed the rest energy whose value per nucleon is $\sim m_p c^2 \approx 0.94$ GeV. Presently, observed cutoff energies are more than an order of magnitude below this threshold. Nevertheless, the scalings inferred from either experiments or theoretical models and the foreseen availabil-

ity of higher laser powers in a few years suggests that GeV ions may eventually be produced and applied in selected particle physics experiments. Moreover, it should be noted that the very low emittance that can be obtained for laser-accelerated ions makes them suitable for postacceleration, e.g., as an injection source for heavy ion accelerators (Krushelnick *et al.*, 2000). Specific advantages might be the high number of ions produced per shot combined with the short duration.

Bychenkov, Sentoku *et al.* (2001) estimated the threshold for production of pions by protons accelerated in a solid target, obtaining that at intensities above 10^{21} W cm⁻² the flux of pions may be much higher than obtained with conventional accelerator techniques. It should be noted that the prompt laser-driven, high field-gradient acceleration of pions is of much interest because of the finite lifetime of such particles; a related discussion was given by Mourou, Tajima, and Bulanov (2006).

Pakhomov (2002) proposed the use of laser-accelerated protons at intensities of $\approx 10^{23}$ W cm⁻² to drive, via pion generation and decay, pulses of 20 MeV muon neutrinos of interest for, e.g., studies of neutrino oscillations. Bulanov *et al.* (2005) further explored this concept suggesting the radiation pressure dominated acceleration regime (see Sec. IV.A.2) as suitable for this class of experiments. A more general discussion of the required laser developments was given by Terranova *et al.* (2006).

VI. CONCLUSIONS AND OUTLOOK

We reviewed about 12 years of research on ion acceleration driven by superintense laser pulses. The most investigated acceleration mechanism, namely, the so-called target normal sheath acceleration, has been extensively discussed, surveying both the main experimental achievements and the underlying theoretical interpretation. In addition, we provided an outlook to other proposed acceleration schemes, such as radiation pressure acceleration, shock acceleration, breakout afterburner, acceleration in near-critical and underdense plasmas, and resistively enhanced acceleration. For these mechanisms, the fundamental theoretical ideas have been presented, together with the most promising experimental results. A brief presentation of promising possible applications of the laser-generated ion beams has been given. While we were completing our work, another extended review on this topic was published (Daido, Nishiuchi, and Pirozhkov, 2012), which we recommend as complementary reading.

This field of research has attracted much interest and has shown unique potential both for innovative investigations and for applicative purposes. The development in laser technology and the increasing use of advanced methods of material science for target manufacturing has resulted in a high level of sophistication of current experiments, with new physical issues continuously emerging from experimental investigations. At the same time, theory and simulation have naturally found a fertile field, which poses original problems and suggests unexplored paths for reaching their solution. The vitality of this research area is well demonstrated by the need for frequent updates during the preparation of this review, as new significant results continuously appeared in the literature.

²⁹Typical short-lived positron emitters include ^{11}B , ^{11}C , ^{13}N , ^{15}O , ^{18}O , and ^{18}F . Related experiments have been reported, by Nemoto *et al.* (2001), Fritzier *et al.* (2003), Ledingham, McKenna, and Singhal (2003), Clarke *et al.* (2006), Fujimoto *et al.* (2008, 2009), and Ogura *et al.* (2009).

As discussed in the Introduction, future developments and achievements are naturally linked to foreseen developments in laser technology, providing for the first time extreme laser intensities close to or even beyond the limit at which the ions become relativistic. Emerging laser projects will enable one to verify the scaling of ion acceleration physics in the ultra-high intensity regimes and its suitability for proposed applications, as well as to test theoretical ideas and provide to fundamental physics an example of “relativity in action” in a macroscopic, many-body system. The expected progress is not exclusively related to further developments of the solid state laser technology which has been so far the preferred route to producing high-intensity laser pulses, as, for example, recent experiments have attracted novel interest also in old technology such as CO₂ laser systems. Smart and advanced target engineering, e.g., development of multilayer, low-density, microstructured, and nanostructured targets, will also play an important role in establishing future directions of ion acceleration.

The successful developments in this first period lead to a series of open questions, which will inform research in this field over the coming years. Will it be possible to reach and break the GeV/nucleon threshold? Will researchers achieve an active and satisfactory experimental control on the physics of laser ion acceleration by working on the detailed properties of laser pulses and of target material and structure? Is there hope to pursue front-edge nuclear and particle physics research in small-scale laboratories thanks to the use of laser-driven ion beams? Will the research on ion acceleration result in practical, technological applications of direct societal benefit? We leave to the future experimental and theoretical research the answer to these and many other questions, some of which we probably do not even imagine today.

ACKNOWLEDGMENTS

We acknowledge support of EPSRC, Grant No. EP/E035728/1 (LIBRA consortium), the Ministry of Education of the Czech Republic (Projects ECOP No. CZ.1.07/2.3.00/20.0279 and ELI- Beamlines No. CZ.1.05/1.1.00/02.0061), and from the Italian Ministry of University and Research via the FIRB project “Superintense Laser-Driven Ion Sources.”

REFERENCES

- Adusumilli, K., D. Goyal, and V.K. Tripathi, 2012, *Phys. Plasmas* **19**, 013102.
- Akli, K. U., *et al.*, 2008, *Phys. Rev. Lett.* **100**, 165002.
- Albright, B. J., L. Yin, K. J. Bowers, B. M. Hegelich, K. A. Flippo, T. J. T. Kwan, and J. C. Fernández, 2007, *Phys. Plasmas* **14**, 094502.
- Albright, B. J., *et al.*, 2010, *J. Phys. Conf. Ser.* **244**, 042022.
- Albright, B. J., L. Yin, B. M. Hegelich, K. J. Bowers, T. J. T. Kwan, and J. C. Fernández, 2006, *Phys. Rev. Lett.* **97**, 115002.
- Allen, J. E., and J. G. Andrews, 1970, *J. Plasma Phys.* **4**, 187.
- Allen, M., P. K. Patel, A. MacKinnon, D. Price, S. Wilks, and E. Morse, 2004, *Phys. Rev. Lett.* **93**, 265004.
- Allen, M., *et al.*, 2003, *Phys. Plasmas* **10**, 3283.
- Amaldi, U., and G. Kraft, 2005, *Rep. Prog. Phys.* **68**, 1861.
- Andreev, A., A. Lévy, T. Ceccotti, C. Thauray, K. Platonov, R. A. Loch, and P. Martin, 2008, *Phys. Rev. Lett.* **101**, 155002.
- Antici, P., *et al.*, 2007, *Phys. Plasmas* **14**, 030701.
- Antici, P., M. Migliorati, A. Mostacci, L. Picardi, L. Palumbo, and C. Ronsivalle, 2011, *Phys. Plasmas* **18**, 073103.
- Atzeni, S., and J. Meyer-ter-Vehn, 2004, *The Physics of Inertial Fusion* (Oxford University Press, New York).
- Atzeni, S., M. Temporal, and J. Honrubia, 2002, *Nucl. Fusion* **42**, L1.
- Badziak, J., S. Glowacz, S. Jablonski, P. Parys, J. Wołowski, and H. Hora, 2004, *Appl. Phys. Lett.* **85**, 3041.
- Badziak, J., G. Mishra, N. K. Gupta, and A. R. Holkundkar, 2011, *Phys. Plasmas* **18**, 053108.
- Badziak, J., E. Woryna, P. Parys, K. Y. Platonov, S. Jabłoński, L. Ryć, A. B. Vankov, and J. Wołowski, 2001, *Phys. Rev. Lett.* **87**, 215001.
- Bailey, J., *et al.*, 1990, *Laser Part. Beams* **8**, 555.
- Barriga-Carrasco, M. D., G. Maynard, and Y. K. Kurilenkov, 2004, *Phys. Rev. E* **70**, 066407.
- Bartal, T., *et al.*, 2012, *Nat. Phys.* **8**, 139.
- Bartoli, A., 1884, *Il Nuovo Cimento B* **15**, 193.
- Batani, D., *et al.*, 2010, *New J. Phys.* **12**, 045018.
- Bauer, D., P. Mulser, and W. H. Steeb, 1995, *Phys. Rev. Lett.* **75**, 4622.
- Beg, F. N., A. R. Bell, A. E. Dangor, C. N. Danson, A. P. Fews, M. E. Glinsky, B. A. Hammel, P. Lee, P. A. Norreys, and M. Tatarakis, 1997, *Phys. Plasmas* **4**, 447.
- Beg, F. N., *et al.*, 2004, *Phys. Plasmas* **11**, 2806.
- Bell, A. R., A. P. L. Robinson, M. Sherlock, R. J. Kingham, and W. Rozmus, 2006, *Plasma Phys. Controlled Fusion* **48**, R37.
- Bellei, C., *et al.*, 2010, *New J. Phys.* **12**, 073016.
- Betti, S., F. Ceccherini, F. Cornolti, and F. Pegoraro, 2005, *Plasma Phys. Controlled Fusion* **47**, 521.
- Bezzerrides, B., D. W. Forslund, and E. L. Lindman, 1978, *Phys. Fluids* **21**, 2179.
- Bigongiari, A., M. Raynaud, C. Riconda, A. Héron, and A. Macchi, 2011, *Phys. Plasmas* **18**, 102701.
- Birdsall, C. K., and A. B. Langdon, 1991, *Plasma Physics Via Computer Simulation* (Institute of Physics, Bristol).
- Bolton, P., T. Hori, H. Kiriya, M. Mori, H. Sakaki, K. Sutherland, M. Suzuki, J. Wu, and A. Yogo, 2010, *Nucl. Instrum. Methods Phys. Res., Sect. A* **620**, 71.
- Borghesi, M., J. Fuchs, S. V. Bulanov, A. J. MacKinnon, P. K. Patel, and M. Roth, 2006, *Fusion Sci. Technol.* **49**, 412 [http://www.new.ans.org/pubs/journals/fst/a_1159].
- Borghesi, M., A. J. MacKinnon, D. H. Campbell, D. G. Hicks, S. Kar, P. K. Patel, D. Price, L. Romagnani, A. Schiavi, and O. Willi, 2004, *Phys. Rev. Lett.* **92**, 055003.
- Borghesi, M., A. Schiavi, D. H. Campbell, M. G. Haines, O. Willi, A. J. MacKinnon, L. A. Gizzi, M. Galimberti, R. J. Clarke, and H. Ruhl, 2001, *Plasma Phys. Controlled Fusion* **43**, A267.
- Borghesi, M., *et al.*, 2002a, *Phys. Rev. Lett.* **88**, 135002.
- Borghesi, M., *et al.*, 2002b, *Phys. Plasmas* **9**, 2214.
- Borghesi, M., *et al.*, 2005, *Phys. Rev. Lett.* **94**, 195003.
- Borghesi, M., *et al.*, 2008, *Plasma Phys. Controlled Fusion* **50**, 124040.
- Borghesi, M., *et al.*, 2011, *Proc. SPIE Int. Soc. Opt. Eng.* **8079**, 80791E.
- Bourdier, A., 1983, *Phys. Fluids* **26**, 1804.
- Brady, C. S., and T. D. Arber, 2011, *Plasma Phys. Controlled Fusion* **53**, 015001.
- Brambrink, E., *et al.*, 2007, *Phys. Rev. E* **75**, 065401.

- Brambrink, E., J. Schreiber, T. Schlegel, P. Audebert, J. Cobble, J. Fuchs, M. Hegelich, and M. Roth 2006, *Phys. Rev. Lett.* **96**, 154801.
- Brantov, A. V., V. T. Tikhonchuk, O. Klimo, D. V. Romanov, S. Ter-Avetisyan, M. Schnrer, T. Sokollik, and P. V. Nickles, 2006, *Phys. Plasmas* **13**, 122705.
- Breschi, E., M. Borghesi, D. Campbell, M. Galimberti, D. Giulietti, L. A. Gizzi, L. Romagnani, A. Schiavi, and O. Willi, 2004, *Laser Part. Beams* **22**, 393.
- Brunel, F., 1987, *Phys. Rev. Lett.* **59**, 52.
- Brunel, F., 1988, *Phys. Fluids* **31**, 2714.
- Buffechoux, S., *et al.*, 2010, *Phys. Rev. Lett.* **105**, 015005.
- Bulanov, S., T. Esirkepov, V. Khoroshkov, A. Kuznetsov, and F. Pegoraro, 2002, *Phys. Lett. A* **299**, 240.
- Bulanov, S. S., *et al.*, 2008, *Phys. Rev. E* **78**, 026412.
- Bulanov, S. V., E. Y. Echkina, T. Z. Esirkepov, I. N. Inovenkov, M. Kando, F. Pegoraro, and G. Korn, 2010a, *Phys. Plasmas* **17**, 063102.
- Bulanov, S. V., E. Y. Echkina, T. Z. Esirkepov, I. N. Inovenkov, M. Kando, F. Pegoraro, and G. Korn, 2010b, *Phys. Rev. Lett.* **104**, 135003.
- Bulanov, S. V., *et al.*, 2000, *JETP Lett.* **71**, 407.
- Bulanov, S. V., T. Esirkepov, P. Migliozzi, F. Pegoraro, T. Tajima, and F. Terranova, 2005, *Nucl. Instrum. Methods Phys. Res., Sect. A* **540**, 25.
- Bulanov, S. V., and T. Z. Esirkepov, 2007, *Phys. Rev. Lett.* **98**, 049503.
- Bulanov, S. V., and V. Khoroshkov, 2002, *Plasma Phys. Rep.* **28**, 453.
- Burza, M., A. Gonoskov, G. Genoud, A. Persson, K. Svensson, M. Quinn, P. McKenna, M. Marklund, and C.-G. Wahlström, 2011, *New J. Phys.* **13**, 013030.
- Bychenkov, V., W. Rozmus, A. Maksimchuk, D. Umstadter, and C. Capjack, 2001, *Plasma Phys. Rep.* **27**, 1017.
- Bychenkov, V., Y. Sentoku, S. Bulanov, K. Mima, G. Mourou, and S. Tolokonnikov, 2001, *JETP Lett.* **74**, 586.
- Bychenkov, V. Y., V. N. Novikov, D. Batani, V. T. Tikhonchuk, and S. G. Bochkarev, 2004, *Phys. Plasmas* **11**, 3242.
- Carroll, D. C., *et al.*, 2007, *Phys. Rev. E* **76**, 065401.
- Cattani, F., A. Kim, D. Anderson, and M. Lisak, 2000, *Phys. Rev. E* **62**, 1234.
- Ceccherini, F., S. Betti, F. Cornolti, and F. Pegoraro, 2006, *Laser Phys.* **16**, 594.
- Cecchetti, C. A., *et al.*, 2009, *Phys. Plasmas* **16**, 043102.
- Ceccotti, T., A. Lévy, H. Popescu, F. Réau, P. D'Oliveira, P. Monot, J. P. Geindre, E. Lefebvre, and P. Martin, 2007, *Phys. Rev. Lett.* **99**, 185002.
- Ceccotti, T., A. Lévy, F. Réau, H. Popescu, P. Monot, E. Lefebvre, and P. Martin, 2008, *Plasma Phys. Controlled Fusion* **50**, 124006.
- Chen, H., A. U. Hazi, R. van Maren, S. N. Chen, J. Fuchs, M. Gauthier, S. L. Pape, J. R. Rygg, and R. Shepherd, 2010, *Rev. Sci. Instrum.* **81**, 10D314.
- Chen, H., A. J. Link, R. van Maren, P. K. Patel, R. Shepherd, S. C. Wilks, and P. Beiersdorfer, 2008, *Rev. Sci. Instrum.* **79**, 10E533.
- Chen, H., S. C. Wilks, W. L. Kruer, P. K. Patel, and R. Shepherd, 2009, *Phys. Plasmas* **16**, 020705.
- Chen, M., N. Kumar, A. Pukhov, and T.-P. Yu, 2011, *Phys. Plasmas* **18**, 073106.
- Chen, M., A. Pukhov, Z. M. Sheng, and X. Q. Yan, 2008, *Phys. Plasmas* **15**, 113103.
- Chen, M., A. Pukhov, T. P. Yu, and Z. M. Sheng, 2009, *Phys. Rev. Lett.* **103**, 024801.
- Chen, M., Z.-M. Sheng, Q.-L. Dong, M.-Q. He, Y.-T. Li, M. A. Bari, and J. Zhang, 2007, *Phys. Plasmas* **14**, 053102.
- Clark, E. L., *et al.*, 2000a, *Phys. Rev. Lett.* **84**, 670.
- Clark, E. L., K. Krushelnick, M. Zepf, F. N. Beg, M. Tatarakis, A. Machacek, M. I. K. Santala, I. Watts, P. A. Norreys, and A. E. Dangor, 2000b, *Phys. Rev. Lett.* **85**, 1654.
- Clarke, R., *et al.*, 2008, *Nucl. Instrum. Methods Phys. Res., Sect. A* **585**, 117.
- Clarke, R. J., *et al.*, 2006, *Appl. Phys. Lett.* **89**, 141117.
- Cobble, J. A., R. P. Johnson, T. E. Cowan, N. R.-L. Galloudec, and M. Allen, 2002, *J. Appl. Phys.* **92**, 1775.
- Cowan, T. E., *et al.*, 2004, *Phys. Rev. Lett.* **92**, 204801.
- Crow, J. E., P. L. Auer, and J. E. Allen, 1975, *J. Plasma Phys.* **14**, 65.
- Daido, H., M. Nishiuchi, and A. S. Pirozhkov, 2012, *Rep. Prog. Phys.* **75**, 056401.
- Davies, J. R., 2002, *Laser Part. Beams* **20**, 243.
- Davies, J. R., 2003, *Phys. Rev. E* **68**, 056404.
- Davies, J. R., A. R. Bell, M. G. Haines, and S. M. Guérin, 1997, *Phys. Rev. E* **56**, 7193.
- Davis, J., and G. M. Petrov, 2008, *Phys. Plasmas* **15**, 083107.
- Davis, J., and G. M. Petrov, 2011, *Phys. Plasmas* **18**, 073109.
- Dawson, J., 1962, *Phys. Fluids* **5**, 445.
- Dawson, J. M., 1983, *Rev. Mod. Phys.* **55**, 403.
- Denavit, J., 1979, *Phys. Fluids* **22**, 1384.
- Denavit, J., 1992, *Phys. Rev. Lett.* **69**, 3052.
- d'Humières, E., E. Lefebvre, L. Gremillet, and V. Malka, 2005, *Phys. Plasmas* **12**, 062704.
- Diaw, A., and P. Mora, 2011, *Phys. Rev. E* **84**, 036402.
- Di Piazza, A., C. Müller, K. Z. Hatsagortsyan, and C. H. Keitel, 2012, *Rev. Mod. Phys.* **84**, 1177.
- Disdier, L., J.-P. Garçonnet, G. Malka, and J.-L. Miquel, 1999, *Phys. Rev. Lett.* **82**, 1454.
- Ditmire, T., J. W. G. Tisch, E. Springate, M. B. Mason, N. Hay, R. A. Smith, J. Marangos, and M. H. R. Hutchinson, 1997, *Nature (London)* **386**, 54.
- Ditmire, T., J. Zweiback, V. P. Yanovsky, T. E. Cowan, G. Hays, and K. B. Wharton, 1999, *Nature (London)* **398**, 489.
- Dollar, F., *et al.*, 2011, *Phys. Rev. Lett.* **107**, 065003.
- Dollar, F., *et al.*, 2012, *Phys. Rev. Lett.* **108**, 175005.
- Doria, D., *et al.*, 2012, *AIP Adv.* **2**, 011209.
- Dorozhkina, D. S., and V. E. Semenov, 1998, *Phys. Rev. Lett.* **81**, 2691.
- Dover, N. P., and Z. Najmudin, 2012, *High Energy Density Phys.* **8**, 170.
- Dromey, B., S. Kar, M. Zepf, and P. Foster, 2004, *Rev. Sci. Instrum.* **75**, 645.
- Dyer, G. M., *et al.*, 2008, *Phys. Rev. Lett.* **101**, 015002.
- Dzelzainis, T., *et al.*, 2010, *Laser Part. Beams* **28**, 451.
- Einstein, A., 1905, *Ann. Phys. (Berlin)* **322**, 891.
- Eliasson, B., C. S. Liu, X. Shao, R. Z. Sagdeev, and P. K. Shukla, 2009, *New J. Phys.* **11**, 073006.
- Ellison, C. L., and J. Fuchs, 2010, *Phys. Plasmas* **17**, 113105.
- Engel, W., 1995, *Radiation Measurements* **25**, 11.
- Enghardt, W., M. Bussmann, T. Cowan, F. Fiedler, M. Kaluza, J. Pawelke, U. Schramm, R. Sauerbrey, A. Tünnermann, and M. Baumann, 2011, *Proc. SPIE Int. Soc. Opt. Eng.* **8079**, 80791F.
- Esarey, E., C. B. Schroeder, and W. P. Leemans, 2009, *Rev. Mod. Phys.* **81**, 1229.
- Esirkepov, T., M. Borghesi, S. V. Bulanov, G. Mourou, and T. Tajima, 2004, *Phys. Rev. Lett.* **92**, 175003.
- Esirkepov, T., *et al.*, 1999, *JETP Lett.* **70**, 82.
- Esirkepov, T., M. Yamagiwa, and T. Tajima, 2006, *Phys. Rev. Lett.* **96**, 105001.

- Esirkepov, T. Z., *et al.*, 2002, *Phys. Rev. Lett.* **89**, 175003.
- Evans, R. G., 2007, *Plasma Phys. Controlled Fusion* **49**, B87.
- Fernández, J. C., J. Honrubia, B. J. Albright, K. A. Flippo, D. C. Gautier, B. M. Hegelich, M. J. Schmitt, M. Temporal, and L. Yin, 2009, *Nucl. Fusion* **49**, 065004.
- Fews, A. P., P. A. Norreys, F. N. Beg, A. R. Bell, A. E. Dangor, C. N. Danson, P. Lee, and S. J. Rose, 1994, *Phys. Rev. Lett.* **73**, 1801.
- Fiorini, F., *et al.*, 2011, *Phys. Med. Biol.* **56**, 6969.
- Fiuza, F., M. Marti, R. A. Fonseca, L. O. Silva, J. Tonge, J. May, and W. B. Mori, 2011, *Plasma Phys. Controlled Fusion* **53**, 074004.
- Flacco, A., A. Guemnie-Tafo, R. Nuter, M. Veltcheva, D. Batani, E. Lefebvre, and V. Malka, 2008, *J. Appl. Phys.* **104**, 103304.
- Flacco, A., F. Sylla, M. Veltcheva, M. Carrié, R. Nuter, E. Lefebvre, D. Batani, and V. Malka, 2010, *Phys. Rev. E* **81**, 036405.
- Flippo, K. A., J. Workman, D. C. Gautier, S. Letzring, R. P. Johnson, and T. Shimada, 2008, *Rev. Sci. Instrum.* **79**, 10E534.
- Flippo, K. A., *et al.*, 2008, *Phys. Plasmas* **15**, 056709.
- Folkard, M., 1996, *Int. J. Radiat. Biol.* **69**, 729.
- Forslund, D. W., and J. P. Freidberg, 1971, *Phys. Rev. Lett.* **27**, 1189.
- Forslund, D. W., J. M. Kindel, and K. Lee, 1977, *Phys. Rev. Lett.* **39**, 284.
- Forslund, D. W., and C. R. Shonk, 1970, *Phys. Rev. Lett.* **25**, 1699.
- Forward, R. L., 1984, *J. Spacecr. Rockets* **21**, 187.
- Fourkal, E., J. S. Li, M. Ding, T. Tajima, and C.-M. Ma, 2003, *Med. Phys.* **30**, 1660.
- Fourkal, E., J. S. Li, W. Xiong, A. Nahum, and C.-M. Ma, 2003, *Phys. Med. Biol.* **48**, 3977.
- Fourkal, E., I. Velchev, J. Fan, W. Luo, and C.-M. Ma, 2007, *Med. Phys.* **34**, 577.
- Fourkal, E., I. Velchev, C.-M. Ma, and J. Fan, 2011, *Phys. Med. Biol.* **56**, 3123.
- Freeman, R. R., D. Batani, S. Baton, M. Key, and R. Stephens, 2006, *Fusion Sci. Technol.* **49**, 297 [http://www.new.ans.org/pubs/journals/fst/a_1150].
- Freeman, C. G., *et al.*, 2011, *Rev. Sci. Instrum.* **82**, 073301.
- Fritzier, S., V. Malka, G. Grillon, J. P. Rousseau, F. Burgy, E. Lefebvre, E. d'Humières, P. McKenna, and K. W. D. Ledingham, 2003, *Appl. Phys. Lett.* **83**, 3039.
- Fritzier, S., *et al.*, 2002, *Phys. Rev. Lett.* **89**, 165004.
- Fuchs, J., P. Antici, E. d'Humières, E. Lefebvre, M. Borghesi, E. Brambrink, C. Cecchetti, T. Toncian, H. Pépin, and P. Audebert, 2006a, *J. Phys. IV (France)* **133**, 1151.
- Fuchs, J., *et al.*, 1999, *Phys. Plasmas* **6**, 2569.
- Fuchs, J., *et al.*, 2003, *Phys. Rev. Lett.* **91**, 255002.
- Fuchs, J., *et al.*, 2005, *Phys. Rev. Lett.* **94**, 045004.
- Fuchs, J., *et al.*, 2006b, *Nat. Phys.* **2**, 48.
- Fujimoto, M., K. Matsukado, H. Takahashi, Y. Kawada, S. Ohsuka, and S.-I. Aoshima, 2009, *Rev. Sci. Instrum.* **80**, 113301.
- Fujimoto, M., K. Matsukado, H. Takahashi, Y. Kawada, S. Ohsuka, and S. Ichiro Aoshima, 2008, *Appl. Phys. Lett.* **93**, 251101.
- Fukuda, Y., *et al.*, 2009, *Phys. Rev. Lett.* **103**, 165002.
- Gaillard, S., J. Fuchs, N. R.-L. Galloudec, and T. E. Cowan, 2007, *Rev. Sci. Instrum.* **78**, 013304.
- Gaillard, S. A., *et al.*, 2011, *Phys. Plasmas* **18**, 056710.
- Geissel, M., *et al.*, 2005, *Nucl. Instrum. Methods Phys. Res., Sect. A* **544**, 55.
- Gibbon, P., 1994, *Phys. Rev. Lett.* **73**, 664.
- Gibbon, P., 2005a, *Phys. Rev. E* **72**, 026411.
- Gibbon, P., 2005b, *Short Pulse Laser Interaction with Matter* (Imperial College Press, London).
- Gibbon, P., A. Andreev, E. Lefebvre, G. Bonnaud, H. Ruhl, J. Delettrez, and A. R. Bell, 1999, *Phys. Plasmas* **6**, 947.
- Gibbon, P., F. N. Beg, E. L. Clark, R. G. Evans, and M. Zepf, 2004, *Phys. Plasmas* **11**, 4032.
- Gibbon, P., and A. R. Bell, 1992, *Phys. Rev. Lett.* **68**, 1535.
- Gitomer, S. J., R. D. Jones, F. Begay, A. W. Ehler, J. F. Kephart, and R. Kristal, 1986, *Phys. Fluids* **29**, 2679.
- Gizzi, L. A., S. Betti, E. Förster, D. Giulietti, S. Höfer, P. Köster, L. Labate, R. Löttsch, A. P. L. Robinson, and I. Uschman, 2011, *Phys. Rev. ST Accel. Beams* **14**, 011301.
- Goloviznin, V. V., and T. J. Schep, 2000, *Phys. Plasmas* **7**, 1564.
- Grech, M., S. Skupin, A. Diaw, T. Schlegel, and V. T. Tikhonchuk, 2011, *New J. Phys.* **13**, 123003.
- Grech, M., S. Skupin, R. Nuter, L. Gremillet, and E. Lefebvre, 2009, *New J. Phys.* **11**, 093035.
- Green, J. S., *et al.*, 2011, *Proc. SPIE Int. Soc. Opt. Eng.* **8079**, 807919.
- Green, J. S., *et al.*, 2010, *New J. Phys.* **12**, 085012.
- Green, J. S., *et al.*, 2008, *Phys. Rev. Lett.* **100**, 015003.
- Gremillet, L., G. Bonnaud, and F. Amiranoff, 2002, *Phys. Plasmas* **9**, 941.
- Grillon, G., *et al.*, 2002, *Phys. Rev. Lett.* **89**, 065005.
- Gurevich, A., D. Anderson, and H. Wilhelmsson, 1979, *Phys. Rev. Lett.* **42**, 769.
- Gurevich, A. V., L. V. Pariiskaya, and L. P. Pitaevskii, 1966, *Sov. Phys. JETP* **22**, 449 [<http://www.jetp.ac.ru/cgi-bin/e/index/e/22/2/p449?a=list>].
- Gurevich, A. V., L. V. Pariiskaya, and L. P. Pitaevskii, 1973, *Sov. Phys. JETP* **36**, 274 [<http://www.jetp.ac.ru/cgi-bin/e/index/e/36/2/p274?a=list>].
- Habara, H., R. Kodama, Y. Sentoku, N. Izumi, Y. Kitagawa, K. A. Tanaka, K. Mima, and T. Yamanaka, 2003, *Phys. Plasmas* **10**, 3712.
- Habara, H., R. Kodama, Y. Sentoku, N. Izumi, Y. Kitagawa, K. A. Tanaka, K. Mima, and T. Yamanaka, 2004a, *Phys. Rev. E* **69**, 036407.
- Habara, H., *et al.*, 2004b, *Phys. Rev. E* **70**, 046414.
- Haberberger, D., S. Tochitsky, and C. Joshi, 2010, *Opt. Express* **18**, 17865.
- Haberberger, D., *et al.*, 2012, *Nat. Phys.* **8**, 95.
- Habs, D., P. Thirolf, M. Gross, K. Allinger, J. Bin, A. Henig, D. Kiefer, W. Ma, and J. Schreiber, 2011, *Appl. Phys. B* **103**, 471.
- Hannachi, F., *et al.*, 2007, *Plasma Phys. Controlled Fusion* **49**, B79.
- Harres, K., *et al.*, 2010, *Phys. Plasmas* **17**, 023107.
- Hatchett, S. P., *et al.*, 2000, *Phys. Plasmas* **7**, 2076.
- He, M.-Q., Q.-L. Dong, Z.-M. Sheng, S.-M. Weng, M. Chen, H.-C. Wu, and J. Zhang, 2007, *Phys. Rev. E* **76**, 035402.
- Hegelich, B., *et al.*, 2011, *Nucl. Fusion* **51**, 083011.
- Hegelich, B. M., 2011, *Bull. Am. Phys. Soc.* **56**, 322 [<http://meetings.aps.org/link/BAPS.2011.DPP.UI2.4>].
- Hegelich, B. M., *et al.*, 2005, *Phys. Plasmas* **12**, 056314.
- Hegelich, B. M., B. J. Albright, J. Cobble, K. Flippo, S. Letring, M. Paffett, H. Ruhl, J. Schreiber, R. K. Schulze, and J. C. Fernandez, 2006, *Nature (London)* **439**, 441.
- Hegelich, M., *et al.*, 2002, *Phys. Rev. Lett.* **89**, 085002.
- Henig, A., *et al.*, 2009a, *Phys. Rev. Lett.* **102**, 095002.
- Henig, A., *et al.*, 2009b, *Phys. Rev. Lett.* **103**, 045002.
- Henig, A., *et al.*, 2009c, *Phys. Rev. Lett.* **103**, 245003.
- Hey, D. S., M. H. Key, A. J. Mackinnon, A. G. MacPhee, P. K. Patel, R. R. Freeman, L. D. V. Woerkom, and C. M. Castaneda, 2008, *Rev. Sci. Instrum.* **79**, 053501.
- Hoffmann, D., *et al.*, 2000, *Nucl. Instrum. Methods Phys. Res., Sect. B* **161–163**, 9.

- Hofmann, I., J. Meyer-ter Vehn, X. Yan, A. Orzechovskaya, and S. Yaramyshev, 2011, *Phys. Rev. ST Accel. Beams* **14**, 031304.
- Honrubia, J. J., J. C. Fernandez, M. Temporal, B. M. Hegelich, and J. M. ter Vehn, 2009, *Phys. Plasmas* **16**, 102701.
- Hosseini Motlagh, S., S. Mohamadi, and R. Shamsi, 2008, *J. Fusion Energy* **27**, 154.
- Humphries, S., 1990, *Charged Particle Beams* (Wiley, New York).
- Ichimaru, S., 1982, *Rev. Mod. Phys.* **54**, 1017.
- Ikegami, M., *et al.*, 2009, *Phys. Rev. ST Accel. Beams* **12**, 063501.
- Jackson, J. D., 1998, *Classical Electrodynamics* (Wiley, New York), Chap. 7.3, 3rd ed.
- Ji, L., B. Shen, X. Zhang, F. Wang, Z. Jin, M. Wen, W. Wang, and J. Xu, 2009, *Phys. Rev. Lett.* **102**, 239501.
- Jullien, A., *et al.*, 2005, *Opt. Lett.* **30**, 920.
- Jung, D., *et al.*, 2011a, *Rev. Sci. Instrum.* **82**, 043301.
- Jung, D., *et al.*, 2011b, *Phys. Rev. Lett.* **107**, 115002.
- Kaluza, M., J. Schreiber, M. I. K. Santala, G. D. Tsakiris, K. Eidmann, J. Meyer-ter Vehn, and K. J. Witte, 2004, *Phys. Rev. Lett.* **93**, 045003.
- Kar, S., K. Markey, M. Borghesi, D. C. Carroll, P. McKenna, D. Neely, M. N. Quinn, and M. Zepf, 2011, *Phys. Rev. Lett.* **106**, 225003.
- Kar, S., *et al.*, 2007, *New J. Phys.* **9**, 402.
- Kar, S., *et al.*, 2008a, *Phys. Rev. Lett.* **100**, 225004.
- Kar, S., *et al.*, 2008b, *Phys. Rev. Lett.* **100**, 105004.
- Kar, S., *et al.*, 2012, *Phys. Rev. Lett.* **109**, 185006.
- Karsch, S., S. Düsterer, H. Schwoerer, F. Ewald, D. Habs, M. Hegelich, G. Pretzler, A. Pukhov, K. Witte, and R. Sauerbrey, 2003, *Phys. Rev. Lett.* **91**, 015001.
- Kemp, A. J., B. I. Cohen, and L. Divol, 2010, *Phys. Plasmas* **17**, 056702.
- Kemp, A. J., and H. Ruhl, 2005, *Phys. Plasmas* **12**, 033105.
- Key, M. H., 2007, *Phys. Plasmas* **14**, 055502.
- Key, M. H., *et al.*, 1998, *Phys. Plasmas* **5**, 1966.
- King, N., *et al.*, 1999, *Nucl. Instrum. Methods Phys. Res., Sect. A* **424**, 84.
- Kirby, D., S. Green, F. Fiorini, D. Parker, L. Romagnani, D. Doria, S. Kar, C. Lewis, M. Borghesi, and H. Palmans, 2011, *Laser Part. Beams* **29**, 231.
- Kishimoto, Y., K. Mima, T. Watanabe, and K. Nishikawa, 1983, *Phys. Fluids* **26**, 2308.
- Klimo, O., J. Psikal, J. Limpouch, J. Proška, F. Novotny, T. Ceccotti, V. Floquet, and S. Kawata, 2011, *New J. Phys.* **13**, 053028.
- Klimo, O., J. Psikal, J. Limpouch, and V. T. Tikhonchuk, 2008, *Phys. Rev. ST Accel. Beams* **11**, 031301.
- Klimo, O., V. T. Tikhonchuk, and A. Debayle, 2007, *Phys. Rev. E* **75**, 016403.
- Knoll, G. F., 2010, *Radiation Detection and Measurement* (Wiley, New York), 4th ed.
- Koehler, A. M., 1968, *Science* **160**, 303.
- Koenig, M., *et al.*, 2005, *Plasma Phys. Controlled Fusion* **47**, B441.
- Kovalev, V., V. Bychenkov, and V. Tikhonchuk, 2001, *JETP Lett.* **74**, 10.
- Kovalev, V., V. Bychenkov, and V. Tikhonchuk, 2002, *J. Exp. Theor. Phys.* **95**, 226.
- Kovalev, V. F., and V. Y. Bychenkov, 2003, *Phys. Rev. Lett.* **90**, 185004.
- Kraft, G., and S. D. Kraft, 2009, *New J. Phys.* **11**, 025001.
- Kraft, S. D., *et al.*, 2010, *New J. Phys.* **12**, 085003.
- Kritcher, A. L., *et al.*, 2008, *Science* **322**, 69.
- Kruer, W. L., and K. Estabrook, 1985, *Phys. Fluids* **28**, 430.
- Krushelnick, K., *et al.*, 2000, *IEEE Trans. Plasma Sci.* **28**, 1110.
- Krushelnick, K., E. L. Clark, F. N. Beg, A. E. Dangor, Z. Najmudin, P. A. Norreys, M. Wei, and M. Zepf, 2005, *Plasma Phys. Controlled Fusion* **47**, B451.
- Krushelnick, K., *et al.*, 1999, *Phys. Rev. Lett.* **83**, 737.
- Kugland, N. L., 2012, *Nat. Phys.* **8**, 809.
- Lancaster, K. L., *et al.*, 2004, *Phys. Plasmas* **11**, 3404.
- Lancia, L., *et al.*, 2011, *Phys. Plasmas* **18**, 030705.
- Landau, L. D., and E. M. Lifshitz, 1962, *The Classical Theory of Fields* (Elsevier, Oxford), Chap. 78, 2nd ed., p. 250.
- Landau, L. D., and E. M. Lifshitz, 1980, *Statistical Physics: Part I, Course of Theoretical Physics* (Butterworth-Heinemann, Oxford, England).
- Lawrence, J., 1957, *Cancer* **10**, 795.
- Ledingham, K. W. D., P. McKenna, and R. P. Singhal, 2003, *Science* **300**, 1107.
- Lee, K., J. Y. Lee, S. H. Park, Y.-H. Cha, Y. W. Lee, K. N. Kim, and Y. U. Jeong, 2011, *Phys. Plasmas* **18**, 013101.
- Lee, K., S. H. Park, Y.-H. Cha, J. Y. Lee, Y. W. Lee, K.-H. Yea, and Y. U. Jeong, 2008, *Phys. Rev. E* **78**, 056403.
- Lee, R. W., *et al.*, 2003, *J. Opt. Soc. Am. B* **20**, 770.
- Lefebvre, E., E. d'Humières, S. Fritzler, and V. Malka, 2006, *J. Appl. Phys.* **100**, 113308.
- Li, C. K., *et al.*, 2006, *Phys. Rev. Lett.* **97**, 135003.
- Li, Y. T., *et al.*, 2005, *Phys. Rev. E* **72**, 066404.
- Lindau, F., O. Lundh, A. Persson, P. McKenna, K. Osvay, D. Batani, and C.-G. Wahlström, 2005, *Phys. Rev. Lett.* **95**, 175002.
- Linz, U., and J. Alonso, 2007, *Phys. Rev. ST Accel. Beams* **10**, 094801.
- Liseikina, T. V., and A. Macchi, 2007, *Appl. Phys. Lett.* **91**, 171502.
- Liseykina, T. V., M. Borghesi, A. Macchi, and S. Tuveri, 2008, *Plasma Phys. Controlled Fusion* **50**, 124033.
- Liu, M.-P., B.-S. Xie, Y.-S. Huang, J. Liu, and M. Yu, 2009, *Laser Part. Beams* **27**, 327.
- Lontano, M., and M. Passoni, 2006, *Phys. Plasmas* **13**, 042102.
- Lundh, O., F. Lindau, A. Persson, C.-G. Wahlström, P. McKenna, and D. Batani, 2007, *Phys. Rev. E* **76**, 026404.
- Luo, W., J. Li, E. Fourkal, J. Fan, X. Xu, Z. Chen, L. Jin, R. Price, and C.-M. Ma, 2008, *Phys. Med. Biol.* **53**, 7151.
- Ma, C., I. Veltchev, E. Fourkal, J. Li, J. Fan, T. Lin, W. Luo, and S. Stathakis, 2006, *Med. Phys.* **33**, 2117.
- Macchi, A., 2006, *Appl. Phys. B* **82**, 337.
- Macchi, A., F. Cattani, T. V. Liseykina, and F. Cornolti, 2005, *Phys. Rev. Lett.* **94**, 165003.
- Macchi, A., F. Ceccherini, F. Cornolti, S. Kar, and M. Borghesi, 2009, *Plasma Phys. Controlled Fusion* **51**, 024005.
- Macchi, A., T. V. Liseykina, S. Tuveri, and S. Veghini, 2009, *C. R. Physique* **10**, 207.
- Macchi, A., A. S. Nindrayog, and F. Pegoraro, 2012, *Phys. Rev. E* **85**, 046402.
- Macchi, A., S. Veghini, T. V. Liseykina, and F. Pegoraro, 2010, *New J. Phys.* **12**, 045013.
- Macchi, A., S. Veghini, and F. Pegoraro, 2009, *Phys. Rev. Lett.* **103**, 085003.
- Mackinnon, A. J., M. Borghesi, S. Hatchett, M. H. Key, P. K. Patel, H. Campbell, A. Schiavi, R. Snavely, S. C. Wilks, and O. Willi, 2001, *Phys. Rev. Lett.* **86**, 1769.
- Mackinnon, A. J., *et al.*, 2006, *Phys. Rev. Lett.* **97**, 045001.
- Mackinnon, A. J., P. K. Patel, D. W. Price, D. Hicks, L. Romagnani, and M. Borghesi, 2003, *Appl. Phys. Lett.* **82**, 3188.
- Mackinnon, A. J., *et al.*, 2004, *Rev. Sci. Instrum.* **75**, 3531.
- Mackinnon, A. J., Y. P. Sentoku, K. Patel, D. W. Price, S. Hatchett, M. H. Key, C. Andersen, R. Snavely, and R. R. Freeman, 2002, *Phys. Rev. Lett.* **88**, 215006.
- Maksimchuk, A., S. Gu, K. Flippo, D. Umstadter, and V. Y. Bychenkov, 2000, *Phys. Rev. Lett.* **84**, 4108.
- Malka, V., *et al.*, 2004, *Med. Phys.* **31**, 1587.

- Mančić, A., J. Fuchs, P. Antici, S.A. Gaillard, and P. Audebert, 2008, *Rev. Sci. Instrum.* **79**, 073301.
- Mančić, A., *et al.*, 2010a, *Phys. Rev. Lett.* **104**, 035002.
- Mančić, A., *et al.*, 2010b, *High Energy Density Phys.* **6**, 21.
- Manclossi, M., J. J. Santos, D. Batani, J. Faure, A. Debayle, V. T. Tikhonchuk, and V. Malka, 2006, *Phys. Rev. Lett.* **96**, 125002.
- Margarone, D., *et al.*, 2011, *J. Appl. Phys.* **109**, 103302.
- Markey, K., *et al.*, 2010, *Phys. Rev. Lett.* **105**, 195008.
- Martins, S.F., R. A. Fonseca, L. O. Silva, and W.B. Mori, 2009, *Astrophys. J. Lett.* **695**, L189.
- Marx, G., 1966, *Nature (London)* **211**, 22.
- Matsukado, K., *et al.*, 2003, *Phys. Rev. Lett.* **91**, 215001.
- Maxwell, J.C., 1873, *A Treatise on Electricity and Magnetism* (Macmillan and Co., London), Vol. 2.
- McKenna, P., *et al.*, 2008, *Laser Part. Beams* **26**, 591.
- McKenna, P., *et al.*, 2007, *Phys. Rev. Lett.* **98**, 145001.
- McKenna, P., *et al.*, 2003a, *Appl. Phys. Lett.* **83**, 2763.
- McKenna, P., *et al.*, 2003b, *Phys. Rev. Lett.* **91**, 075000.
- McKenna, P., *et al.*, 2005, *Phys. Rev. Lett.* **94**, 084801.
- McKenna, P., *et al.*, 2004, *Phys. Rev. E* **70**, 036405.
- McKenna, P., *et al.*, 2011, *Phys. Rev. Lett.* **106**, 185004.
- McLaughlin, J.M.A., W.L.A. and Puhl, M.A. Al-Sheikhly, C. A. A. Christou, A. B. Miller, A. C. Kovács, L. C. Wojnarovits, and D. F. D. Lewis, 1996, *Radiation Protection Dosimetry* **66**, 263.
- Mendel, C. W., and J. N. Olsen, 1975, *Phys. Rev. Lett.* **34**, 859.
- Mora, P., 2003, *Phys. Rev. Lett.* **90**, 185002.
- Mora, P., 2005, *Phys. Rev. E* **72**, 056401.
- Mora, P., and R. Pellat, 1979, *Phys. Fluids* **22**, 2300.
- Mourou, G. A., T. Tajima, and S. V. Bulanov, 2006, *Rev. Mod. Phys.* **78**, 309.
- Mulser, P., and D. Bauer, 2010, *High Power Laser-Matter Interaction*, Springer Tracts in Modern Physics (Springer, New York), Vol. 238.
- Mulser, P., H. Ruhl, and J. Steinmetz, 2001, *Laser Part. Beams* **19**, 23.
- Nakamura, H., *et al.*, 2009, *Phys. Rev. Lett.* **102**, 045009.
- Nakamura, S., *et al.*, 2006, *Jpn. J. Appl. Phys.* **45**, L913.
- Nakamura, T., M. Tampo, R. Kodama, S. V. Bulanov, and M. Kando, 2010, *Phys. Plasmas* **17**, 113107.
- Naumova, N., T. Schlegel, V. T. Tikhonchuk, C. Labaune, I. V. Sokolov, and G. Mourou, 2009, *Phys. Rev. Lett.* **102**, 025002.
- Nayuki, T., Y. Oishi, T. Fujii, K. Takano, X. Wang, A. A. Andreev, K. Nemoto, and K. Ueda, 2006, *J. Appl. Phys.* **100**, 043111.
- Neely, D., P. Foster, A. Robinson, F. Lindau, O. Lundh, A. Persson, C.-G. Wahlström, and P. McKenna, 2006, *Appl. Phys. Lett.* **89**, 021502.
- Nemoto, K., A. Maksimchuk, S. Banerjee, K. Flippo, G. Mourou, D. Umstadter, and V. Y. Bychenkov, 2001, *Appl. Phys. Lett.* **78**, 595.
- Nilson, P.M., *et al.*, 2010, *Phys. Rev. Lett.* **105**, 235001.
- Nilson, P.M., *et al.*, 2011, *Phys. Plasmas* **18**, 042702.
- Nilson, P.M., *et al.*, 2006, *Phys. Rev. Lett.* **97**, 255001.
- Niroomand-Rad, A., C. R. Blackwell, B. M. Coursey, K. P. Gall, J. M. Galvin, W. L. McLaughlin, A. S. Meigooni, R. Nath, J. E. Rodgers, and C. G. Soares, 1998, *Med. Phys.* **25**, 2093.
- Nishiuchi, M., *et al.*, 2006, *Phys. Lett. A* **357**, 339.
- Nishiuchi, M., *et al.*, 2008, *Phys. Plasmas* **15**, 053104.
- Nishiuchi, M., *et al.*, 2009, *Appl. Phys. Lett.* **94**, 061107.
- Nishiuchi, M., *et al.*, 2010a, *Phys. Rev. ST Accel. Beams* **13**, 071304.
- Nishiuchi, M., *et al.*, 2010b, *J. Phys. Conf. Ser.* **244**, 022051.
- Norreys, P. A., *et al.*, 1998, *Plasma Phys. Controlled Fusion* **40**, 175.
- Nuernberg, F., *et al.*, 2009, *Rev. Sci. Instrum.* **80**, 033301.
- Offermann, D. T., *et al.*, 2010, *J. Phys. Conf. Ser.* **244**, 022053.
- Ogura, K., *et al.*, 2009, *Appl. Phys. Express* **2**, 066001.
- Ogura, K., *et al.*, 2012, *Opt. Lett.* **37**, 2868.
- Pakhomov, A. V., 2002, *J. Phys. G* **28**, 1469.
- Palaniyappan, S., *et al.*, 2012, *Nat. Phys.* **8**, 763.
- Palmer, C. A. J., *et al.*, 2011, *Phys. Rev. Lett.* **106**, 014801.
- Palmer, C. A. J., *et al.*, 2012, *Phys. Rev. Lett.* **108**, 225002.
- Passoni, M., L. Bertagna, T. Ceccotti, and P. Martin, 2009, *AIP Conf. Proc.* **1153**, 159.
- Passoni, M., L. Bertagna, and A. Zani, 2010a, *Nucl. Instrum. Methods Phys. Res., Sect. A* **620**, 46.
- Passoni, M., L. Bertagna, and A. Zani, 2010b, *New J. Phys.* **12**, 045012.
- Passoni, M., and M. Lontano, 2004, *Laser Part. Beams* **22**, 163.
- Passoni, M., and M. Lontano, 2008, *Phys. Rev. Lett.* **101**, 115001.
- Passoni, M., V. T. Tikhonchuk, M. Lontano, and V. Y. Bychenkov, 2004, *Phys. Rev. E* **69**, 026411.
- Patel, P. K., A. J. Mackinnon, M. H. Key, T. E. Cowan, M. E. Foord, M. Allen, D. F. Price, H. Ruhl, P. T. Springer, and R. Stephens, 2003, *Phys. Rev. Lett.* **91**, 125004.
- Peano, F., G. Coppia, F. Peinetti, R. Mulas, and L. O. Silva, 2007, *Phys. Rev. E* **75**, 066403.
- Pearlman, J. S., and R. L. Morse, 1978, *Phys. Rev. Lett.* **40**, 1652.
- Pegoraro, F., and S. V. Bulanov, 2007, *Phys. Rev. Lett.* **99**, 065002.
- Pelka, A., *et al.*, 2010, *Phys. Rev. Lett.* **105**, 265701.
- Perego, C., A. Zani, D. Batani, and M. Passoni, 2011, *Nucl. Instrum. Methods Phys. Res., Sect. A* **653**, 89.
- Perkins, L., B. Logan, M. Rosen, M. Perry, T. D. de la Rubia, N. Ghoniem, T. Ditmire, P. Springer, and S. Wilks, 2000, *Nucl. Fusion* **40**, 1.
- Petrov, G. M., J. Davis, and T. Petrova, 2009, *Plasma Phys. Controlled Fusion* **51**, 095005.
- Pfotenhauer, S. M., O. Jckel, J. Polz, S. Steinke, H.-P. Schlenvoigt, J. Heymann, A. P. L. Robinson, and M. C. Kaluza, 2010, *New J. Phys.* **12**, 103009.
- Pfotenhauer, S. M., *et al.*, 2008, *New J. Phys.* **10**, 033034.
- Ping, Y., *et al.*, 2008, *Phys. Rev. Lett.* **100**, 085004.
- Popescu, H., *et al.*, 2005, *Phys. Plasmas* **12**, 063106.
- Psikal, J., V. T. Tikhonchuk, J. Limpouch, A. A. Andreev, and A. V. Brantov, 2008, *Phys. Plasmas* **15**, 053102.
- Pukhov, A., 2001, *Phys. Rev. Lett.* **86**, 3562.
- Qiao, B., S. Kar, M. Geissler, P. Gibbon, M. Zepf, and M. Borghesi, 2012, *Phys. Rev. Lett.* **108**, 115002.
- Qiao, B., M. Zepf, M. Borghesi, B. Dromey, M. Geissler, A. Karmakar, and P. Gibbon, 2010, *Phys. Rev. Lett.* **105**, 155002.
- Qiao, B., M. Zepf, M. Borghesi, and M. Geissler, 2009, *Phys. Rev. Lett.* **102**, 145002.
- Quinn, K., *et al.* 2009a, *Phys. Rev. Lett.* **102**, 194801.
- Quinn, K., *et al.*, 2009b, *Rev. Sci. Instrum.* **80**, 113506.
- Quinn, M. N., *et al.*, 2011, *Plasma Phys. Controlled Fusion* **53**, 025007.
- Ramis, R., and J. Ramirez, 2004, *Nucl. Fusion* **44**, 720.
- Ravasio, A., *et al.*, 2010, *Phys. Rev. E* **82**, 016407.
- Raynaud, M., J. Kuperszttych, C. Riconda, J. C. Adam, and A. Héron, 2007, *Phys. Plasmas* **14**, 092702.
- Richter, C., *et al.*, 2011, *Phys. Med. Biol.* **56**, 1529.
- Ridgers, C. P., M. Sherlock, R. G. Evans, A. P. L. Robinson, and R. J. Kingham, 2011, *Phys. Rev. E* **83**, 036404.
- Robinson, A. P. L., A. R. Bell, and R. J. Kingham, 2006, *Phys. Rev. Lett.* **96**, 035005.
- Robinson, A. P. L., and P. Gibbon, 2007, *Phys. Rev. E* **75**, 015401.

- Robinson, A. P. L., P. Gibbon, S. M. Pfotenhauer, O. Jckel, and J. Polz, 2009, *Plasma Phys. Controlled Fusion* **51**, 024001.
- Robinson, A. P. L., P. Gibbon, M. Zepf, S. Kar, R. G. Evans, and C. Bellei, 2009, *Plasma Phys. Controlled Fusion* **51**, 024004.
- Robinson, A. P. L., D.-H. Kwon, and K. Lancaster, 2009, *Plasma Phys. Controlled Fusion* **51**, 095006.
- Robinson, A. P. L., D. Neely, P. McKenna, and R. G. Evans, 2007, *Plasma Phys. Controlled Fusion* **49**, 373.
- Robinson, A. P. L., M. Zepf, S. Kar, R. G. Evans, and C. Bellei, 2008, *New J. Phys.* **10**, 013021.
- Robson, L., *et al.*, 2007, *Nat. Phys.* **3**, 58.
- Romagnani, L., *et al.*, 2010, *Phys. Rev. Lett.* **105**, 175002.
- Romagnani, L., *et al.*, 2008, *Phys. Rev. Lett.* **101**, 025004.
- Romagnani, L., *et al.*, 2005, *Phys. Rev. Lett.* **95**, 195001.
- Roth, M., *et al.*, 2001, *Phys. Rev. Lett.* **86**, 436.
- Roth, M., *et al.*, 2002, *Phys. Rev. ST Accel. Beams* **5**, 061301.
- Roth, M., *et al.*, 2009, *Plasma Phys. Controlled Fusion* **51**, 124039.
- Ruhl, H., S. V. Bulanov, T. E. Cowan, T. V. Liseikina, P. Nickles, F. Pegoraro, M. Roth, and W. Sandner, 2001, *Plasma Phys. Rep.* **27**, 363.
- Ruhl, H., T. Cowan, and J. Fuchs, 2004, *Phys. Plasmas* **11**, L17.
- Ruhl, H., A. Macchi, P. Mulser, F. Cornolti, and S. Hain, 1999, *Phys. Rev. Lett.* **82**, 2095.
- Rykovarov, S. G., J. Schreiber, J. M. ter Vehn, C. Bellei, A. Henig, H. C. Wu, and M. Geissler, 2008, *New J. Phys.* **10**, 113005.
- Sakabe, S., T. Mochizuki, T. Yamanaka, and C. Yamanaka, 1980, *Rev. Sci. Instrum.* **51**, 1314.
- Sakaki, H., *et al.*, 2010, *Appl. Phys. Express* **3**, 126401.
- Santala, M. I. K., *et al.*, 2001, *Appl. Phys. Lett.* **78**, 19.
- Sarkisov, G. S., V. Y. Bychenkov, V. N. Novikov, V. T. Tikhonchuk, A. Maksimchuk, S.-Y. Chen, R. Wagner, G. Mourou, and D. Umstadter, 1999, *Phys. Rev. E* **59**, 7042.
- Sarri, G., *et al.*, 2010a, *New J. Phys.* **12**, 045006.
- Sarri, G., *et al.*, 2010b, *Phys. Plasmas* **17**, 010701.
- Sarri, G., *et al.*, 2010c, *Phys. Plasmas* **17**, 113303.
- Sarri, G., *et al.*, 2010d, *Phys. Rev. Lett.* **105**, 175007.
- Sarri, G., *et al.*, 2011a, *Phys. Rev. Lett.* **106**, 095001.
- Sarri, G., *et al.*, 2011b, *Phys. Plasmas* **18**, 080704.
- Schardt, D., 2007, *Nucl. Phys. A* **787**, 633.
- Schardt, D., T. Elsässer, and D. Schulz-Ertner, 2010, *Rev. Mod. Phys.* **82**, 383.
- Schell, S., and J. J. Wilkens, 2010, *Med. Phys.* **37**, 5330.
- Schlegel, T., N. Naumova, V. T. Tikhonchuk, C. Labaune, I. V. Sokolov, and G. Mourou, 2009, *Phys. Plasmas* **16**, 083103.
- Schollmeier, M., *et al.*, 2008, *Phys. Rev. Lett.* **101**, 055004.
- Schreiber, J., *et al.*, 2006, *Phys. Rev. Lett.* **97**, 045005.
- Schreiber, J., *et al.*, 2004, *Appl. Phys. B* **79**, 1041.
- Schwoerer, H., S. Pfotenhauer, O. Jaekel, K. U. Amthor, B. Liesfeld, W. Ziegler, R. Sauerbrey, K. W. D. Ledingham, and T. Esirkepov, 2006, *Nature (London)* **439**, 445.
- Séguin, F. H., *et al.*, 2003, *Rev. Sci. Instrum.* **74**, 975.
- Sentoku, Y., T. E. Cowan, A. Kemp, and H. Ruhl, 2003, *Phys. Plasmas* **10**, 2009.
- Sentoku, Y., *et al.*, 2000, *Phys. Rev. E* **62**, 7271.
- Sentoku, Y., K. Mima, H. Ruhl, Y. Toyama, R. Kodama, and T. E. Cowan, 2004, *Phys. Plasmas* **11**, 3083.
- Sgattoni, A., P. Londrillo, A. Macchi, and M. Passoni, 2012, *Phys. Rev. E* **85**, 036405.
- Shah, R. C., R. P. Johnson, T. Shimada, K. A. Flippo, J. C. Fernandez, and B. M. Hegelich, 2009, *Opt. Lett.* **34**, 2273.
- Shen, B., and Z. Xu, 2001, *Phys. Rev. E* **64**, 056406.
- Shen, B., X. Zhang, Z. Sheng, M. Y. Yu, and J. Cary, 2009, *Phys. Rev. ST Accel. Beams* **12**, 121301.
- Shmatov, M. L., 2003, *Fusion Sci. Technol.* **43**, 456 [http://www.new.ans.org/pubs/journals/fst/a_291].
- Shmatov, M. L., 2008, *J. Phys. Conf. Ser.* **112**, 022061.
- Shmatov, M. L., 2011, *Laser Part. Beams* **29**, 339.
- Silva, L. O., M. Marti, J. R. Davies, R. A. Fonseca, C. Ren, F. S. Tsung, and W. B. Mori, 2004, *Phys. Rev. Lett.* **92**, 015002.
- Simmons, J. F. L., and C. R. McInnes, 1993, *Am. J. Phys.* **61**, 205.
- Smith, A. R., 2009, *Med. Phys.* **36**, 556.
- Snively, R. A., *et al.*, 2000, *Phys. Rev. Lett.* **85**, 2945.
- Snively, R. A., *et al.*, 2007, *Phys. Plasmas* **14**, 092703.
- Sokollik, T., *et al.*, 2008, *Appl. Phys. Lett.* **92**, 091503.
- Solodov, A. A., K. S. Anderson, R. Betti, V. Gotcheva, J. Myatt, J. A. Delettrez, S. Skupsky, W. Theobald, and C. Stoeckl, 2009, *Phys. Plasmas* **16**, 056309.
- Spencer, I., *et al.*, 2001, *Nucl. Instrum. Methods Phys. Res., Sect. B* **183**, 449.
- Spencer, I., *et al.*, 2003, *Phys. Rev. E* **67**, 046402.
- Srivastava, M. K., B. K. Sinha, and S. V. Lawande, 1988, *Phys. Fluids* **31**, 394.
- Tabak, M., J. Hammer, M. E. Glinsky, W. L. Kruer, S. C. Wilks, J. Woodworth, E. M. Campbell, M. D. Perry, and R. J. Mason, 1994, *Phys. Plasmas* **1**, 1626.
- Tahir, N., A. Shutov, I. Lomonosov, A. Piriz, G. Wouchuk, C. Deutsch, D. Hoffmann, and V. Fortov, 2006, *High Energy Density Phys.* **2**, 21.
- Tallents, G., *et al.*, 2009, *High Energy Density Phys.* **5**, 110.
- Tamburini, M., T. V. Liseykina, F. Pegoraro, and A. Macchi, 2012, *Phys. Rev. E* **85**, 016407.
- Tamburini, M., F. Pegoraro, A. D. Piazza, C. H. Keitel, and A. Macchi, 2010, *New J. Phys.* **12**, 123005.
- Tanimoto, T., *et al.*, 2009, *Phys. Plasmas* **16**, 062703.
- Temporal, M., 2006, *Phys. Plasmas* **13**, 122704.
- Temporal, M., J. J. Honrubia, and S. Atzeni, 2002, *Phys. Plasmas* **9**, 3098.
- Temporal, M., J. J. Honrubia, and S. Atzeni, 2008, *Phys. Plasmas* **15**, 052702.
- Ter-Avetisyan, S., M. Schnrer, and P. V. Nickles, 2005, *J. Phys. D* **38**, 863.
- Ter-Avetisyan, S., M. Schnrer, P. V. Nickles, W. Sandner, T. Nakamura, and K. Mima, 2009, *Phys. Plasmas* **16**, 043108.
- Ter-Avetisyan, S., M. Schnrer, R. Polster, P. Nickles, and W. Sandner, 2008, *Laser Part. Beams* **26**, 637.
- Ter-Avetisyan, S., M. Schnürer, P. V. Nickles, M. Kalashnikov, E. Risse, T. Sokollik, W. Sandner, A. Andreev, and V. Tikhonchuk, 2006, *Phys. Rev. Lett.* **96**, 145006.
- Terranova, F., S. V. Bulanov, J. L. Collier, H. Kiriya, and F. Pegoraro, 2006, *Nucl. Instrum. Methods Phys. Res., Sect. A* **558**, 430.
- Thaury, C., *et al.*, 2007, *Nat. Phys.* **3**, 424.
- Thomson, J. J., 1911, *Philos. Mag.* **21**, 225.
- Tidman, D. A., and N. A. Krall, 1971, *Shock Waves in Collisionless Plasmas* (Wiley/Interscience, New York), Chap. 6.
- Tikhonchuk, V., 2010, *Nucl. Instrum. Methods Phys. Res., Sect. A* **620**, 1.
- Tikhonchuk, V., T. Schlegel, C. Regan, M. Temporal, J.-L. Feugeas, P. Nicola, and X. Ribeyre, 2010, *Nucl. Fusion* **50**, 045003.
- Tikhonchuk, V. T., 2002, *Phys. Plasmas* **9**, 1416.
- Tikhonchuk, V. T., A. A. Andreev, S. G. Bochkarev, and V. Y. Bychenkov, 2005, *Plasma Phys. Controlled Fusion* **47**, B869.
- Toncian, T., *et al.*, 2006, *Science* **312**, 410.
- Toncian, T., *et al.*, 2011, *AIP Adv.* **1**, 022142.
- Toupin, C., E. Lefebvre, and G. Bonnaud, 2001, *Phys. Plasmas* **8**, 1011.

- Tresca, O., *et al.*, 2011, *Plasma Phys. Controlled Fusion* **53**, 105008.
- Tripathi, V.K., C.S. Liu, X. Shao, B. Eliasson, and R.Z. Sagdeev, 2009, *Plasma Phys. Controlled Fusion* **51**, 024014.
- True, M.A., J.R. Albritton, and E.A. Williams, 1981, *Phys. Fluids* **24**, 1885.
- Veksler, V., 1957, *At. Energ.* **2**, 525.
- Volpe, L., *et al.*, 2011, *Plasma Phys. Controlled Fusion* **53**, 032003.
- Vshivkov, V.A., N.M. Naumova, F. Pegoraro, and S.V. Bulanov, 1998, *Phys. Plasmas* **5**, 2727.
- Wei, M.S., *et al.*, 2004, *Phys. Rev. Lett.* **93**, 155003.
- Wharton, K.B., S.P. Hatchett, S.C. Wilks, M.H. Key, J.D. Moody, V. Yanovsky, A.A. Offenberger, B.A. Hammel, M.D. Perry, and C. Joshi, 1998, *Phys. Rev. Lett.* **81**, 822.
- Wickens, L.M., J.E. Allen, and P.T. Rumsby, 1978, *Phys. Rev. Lett.* **41**, 243.
- Widner, M., I. Alexeff, and W.D. Jones, 1971, *Phys. Fluids* **14**, 795.
- Wilks, S.C., W.L. Kruer, M. Tabak, and A.B. Langdon, 1992, *Phys. Rev. Lett.* **69**, 1383.
- Wilks, S.C., A.B. Langdon, T.E. Cowan, M. Roth, M. Singh, S. Hatchett, M.H. Key, D. Pennington, A. MacKinnon, and R.A. Snavely, 2001, *Phys. Plasmas* **8**, 542.
- Willingale, L., *et al.*, 2006, *Phys. Rev. Lett.* **96**, 245002.
- Willingale, L., *et al.*, 2007, *Phys. Rev. Lett.* **98**, 049504.
- Willingale, L., *et al.*, 2009, *Phys. Rev. Lett.* **102**, 125002.
- Willingale, L., *et al.* 2010, *Phys. Rev. Lett.* **105**, 095001.
- Willingale, L., P.M. Nilson, A.G.R. Thomas, S.S. Bulanov, A. Maksimchuk, W. Nazarov, T.C. Sangster, C. Stoeckl, and K. Krushelnick, 2011a, *Phys. Plasmas* **18**, 056706.
- Willingale, L., *et al.*, 2011b, *Phys. Rev. Lett.* **106**, 105002.
- Wilson, 1946, *Radiology* **47**, 487 [<http://radiology.rsna.org/content/47/5/487.short>].
- Yan, X., T. Tajima, M. Hegelich, L. Yin, and D. Habs, 2010, *Appl. Phys. B* **98**, 711.
- Yan, X.Q., C. Lin, Z.M. Sheng, Z.Y. Guo, B.C. Liu, Y.R. Lu, J.X. Fang, and J.E. Chen, 2008, *Phys. Rev. Lett.* **100**, 135003.
- Yan, X.Q., C. Lin, Z.M. Sheng, Z.Y. Guo, B.C. Liu, Y.R. Lu, J.X. Fang, and J.E. Chen, 2009a, *Phys. Rev. Lett.* **102**, 239502.
- Yan, X.Q., H.C. Wu, Z.M. Sheng, J.E. Chen, and J. Meyer-ter-Vehn, 2009b, *Phys. Rev. Lett.* **103**, 135001.
- Yang, J.M., *et al.*, 2004a, *J. Appl. Phys.* **96**, 6912.
- Yang, J.M., *et al.*, 2004b, *Appl. Phys. Lett.* **84**, 675.
- Yanovsky, V., *et al.*, 2008, *Opt. Express* **16**, 2109.
- Yin, L., B.J. Albright, K.J. Bowers, D. Jung, J.C. Fernández, and B.M. Hegelich, 2011a, *Phys. Rev. Lett.* **107**, 045003.
- Yin, L., B.J. Albright, B.M. Hegelich, K.J. Bowers, K.A. Flippo, T.J.T. Kwan, and J.C. Fernández, 2007, *Phys. Plasmas* **14**, 056706.
- Yin, L., B.J. Albright, D. Jung, K.J. Bowers, R.C. Shah, S. Palaniyappan, J.C. Fernández, and B.M. Hegelich, 2011b, *Phys. Plasmas* **18**, 053103.
- Yin, Y., W. Yu, M.Y. Yu, A. Lei, X. Yang, H. Xu, and V.K. Senecha, 2008, *Phys. Plasmas* **15**, 093106.
- Yogo, A., *et al.*, 2008, *Phys. Rev. E* **77**, 016401.
- Yogo, A., *et al.*, 2009, *Appl. Phys. Lett.* **94**, 181502.
- Yogo, A., *et al.*, 2011, *Appl. Phys. Lett.* **98**, 053701.
- Youssef, A., R. Kodama, and M. Tampo, 2006, *Phys. Plasmas* **13**, 030702.
- Yu, L.-L., H. Xu, W.-M. Wang, Z.-M. Sheng, B.-F. Shen, W. Yu, and J. Zhang, 2010, *New J. Phys.* **12**, 045021.
- Yu, T.-P., A. Pukhov, G. Shvets, and M. Chen, 2010, *Phys. Rev. Lett.* **105**, 065002.
- Yuan, X.H., *et al.*, 2010, *New J. Phys.* **12**, 063018.
- Zani, A., A. Sgattoni, and M. Passoni 2011, *Nucl. Instrum. Methods Phys. Res., Sect. A* **653**, 94.
- Zani, A., D. Dellasega, V. Russo, and M. Passoni, 2013, *Carbon* **56**, 358.
- Zaouter, Y., L.P. Ramirez, D.N. Papadopoulos, C. Hönninger, M. Hanna, F. Druon, E. Mottay, and P. Georges, 2011, *Opt. Lett.* **36**, 1830.
- Zeil, K., S.D. Kraft, S. Bock, M. Bussmann, T.E. Cowan, T. Kluge, J. Metzkes, T. Richter, R. Sauerbrey, and U. Schramm, 2010, *New J. Phys.* **12**, 045015.
- Zepf, M., *et al.*, 2003, *Phys. Rev. Lett.* **90**, 064801.
- Zhang, X., B. Shen, L. Ji, F. Wang, Z. Jin, X. Li, M. Wen, and J.R. Cary, 2009, *Phys. Rev. ST Accel. Beams* **12**, 021301.
- Zhang, X., B. Shen, X. Li, Z. Jin, and F. Wang, 2007, *Phys. Plasmas* **14**, 073101.
- Zhang, X., B. Shen, M.Y. Yu, X. Li, Z. Jin, F. Wang, and M. Wen, 2007, *Phys. Plasmas* **14**, 113108.
- Zhidkov, A., M. Uesaka, A. Sasaki, and H. Daido, 2002, *Phys. Rev. Lett.* **89**, 215002.
- Ziegler, J., J. Biersack, and M. Ziegler, 2008, *Stopping and Range of ions in Matter* (SRIM Co., Chester, MD).
- Zigler, A., *et al.*, 2011, *Phys. Rev. Lett.* **106**, 134801.